NASA Technical Memorandum 78487

NASA-TM-78487 19790009625

Aerodynamic Properties of a Flat Plate With Cavity for Optical-Propagation Studies

Donald A. Buell

JANUARY 1979

NASA

NASA Technical Memorandum 78487

Aerodynamic Properties of a Flat Plate With Cavity for Optical-Propagation Studies

Donald A. Buell
Ames Research Center
Moffett Field, California

National Aeronautics
and Space Administration

Scientific and Technical
Information Office

1979

SYMBOLS

C_p	static-pressure coefficient, $\frac{\bar{p} - \bar{p}_\infty}{q}$
$\dot{m}$	mass flow of air injected into cavity, kg/sec
M	free-stream Mach number at a station 97 cm downstream from the plate leading edge
M_{local}	Mach number of flow outside boundary layer at arbitrary station
p	static pressure at point of measurement, N/m^2
p_∞	free-stream static pressure where M is defined, N/m^2
p'	fluctuating pressure, $p - \bar{p}$, N/m^2
p_{rms}	root-mean-square pressure, $\sqrt{\overline{(p')^2}}$, N/m^2
PSD	power spectral density of pressure, $(N/m^2)^2/Hz$
q	free-stream dynamic pressure, $\frac{1}{2}\rho_\infty V_\infty{}^2$, N/m^2
R	free-stream Reynolds number per meter, $\frac{\rho_\infty V_\infty}{\mu_\infty}$
V_∞	free-stream velocity where M is defined, m/s
x	coordinate in downstream direction (fig. 3), cm
y	coordinate in cross-stream direction parallel to plate (fig. 3), cm
z	distance from surface of plate, cm
ρ_∞	free-stream density where M is defined, kg/m^3
μ_∞	free-stream viscosity where M is defined, kg/m-sec
$(\bar{\ })$	time-averaged quantity

AERODYNAMIC PROPERTIES OF A FLAT PLATE WITH CAVITY FOR OPTICAL-PROPAGATION STUDIES

Donald A. Buell

Ames Research Center

SUMMARY

Wind-tunnel tests have been performed at transonic speeds on a flat plate with and without a cube-shaped cavity and antiresonance devices. Optical measurements were made of the degradation of a laser beam propagating through the boundary and shear layers. Aerodynamic measurements were made of the densities, velocities, pressures, and temperatures in the flow. This paper describes the model and the velocity profiles of the flow layers, and shows both steady-state and fluctuating pressure measurements.

Model alterations included pins to thicken the boundary layer, fences of various heights and porosities to suppress cavity resonance, and a porous cavity wall, equipped for air injection into the cavity. Different combinations of these devices provided a wide variety of flow and cavity disturbances and enabled a study of the correlation between aerodynamic and optical properties.

INTRODUCTION

An investigation of aerodynamic effects on airborne optical systems that are designed to emit or receive laser radiation has been under way since 1972 under the joint direction of the Air Force and NASA. The studies have emphasized open-port configurations, which serve to avoid the problems of transmission through transparent materials. Early studies were aimed at determining the pressure disturbances in the open cavity containing the optical mirrors. Considerable effort was also expended in minimizing the pressure disturbance loads. A sample of this work is given in reference 1.

More recent studies have been directed towards quantification of the propagation characteristics as the electromagnetic radiation traverses the flow fields surrounding the airplane. References 2 and 3 report some results of transonic wind-tunnel tests of basic thickened boundary-layer flow over a flat plate. The subject of the present paper is a follow-on series of tests of a thickened boundary layer and of the shear layer over a cavity. Also included are shear layers generated by devices that inhibit cavity resonance. The object of the tests was to measure the optical degradation of laser beams traversing the various perturbed layers and, at the same time, to measure the aerodynamic properties of the flows in sufficient detail to permit a mathematical modeling of the optical propagation.

The present paper is primarily a description of the model and of the flow conditions peculiar to each model configuration. The flow conditions are presented in terms of conventional parameters such as pressures on the model surface and mean velocity profiles of the boundary and shear layers. The extent and intensity of flow unsteadiness is indicated by pressure fluctuation levels on the model surface.

The optical measurements and the more detailed flow-probing measurements are to be presented elsewhere by the researchers who made the measurements. Among these researchers are the following: Lt. Col. Keith Gilbert and associates from the Air Force Weapons Laboratory (all optics); Dr. Lawrence D. Weaver of MIT Lincoln Laboratory (modulation transfer function); Dr. James Trolinger of Spectron Development Labs, Inc. (holography); Dr. William C. Rose of Ames Research Center (hot-wire data); Dr. Dennis Johnson of Ames Research Center (laser-doppler velocimeter data); Mr. K. R. Raman of Raman Aeronautics Research and Engineering, Inc. (probe pressure data); and Dr. Dah Yu Cheng and students from the University of Santa Clara (ball-probe data).

Special acknowledgements are due Captain John Otten of the Air Force Weapons Laboratory, who was instrumental in organizing and directing the cooperative NASA-Air Force effort, and Dr. James Van Kuren from Air Force Flight Dynamics Laboratory, who assisted in directing the effort and arranged for preliminary small-scale tests of porous spoilers to assist in spoiler selection. Thanks are also due Mr. K. R. Raman for providing the rake and probe pressure data presented herein.

WIND TUNNEL

The tests were conducted in the Ames 6- by 6-Foot Supersonic Wind Tunnel, the same facility used in the investigation of reference 2. The test section is square in cross section and has slots in the floor and ceiling to facilitate transonic testing.

MODEL

The model, shown in one of its 20 configurations in figure 1, consisted of a splitter plate mounted on the side wall of the wind tunnel. A window was placed in the plate to permit the laser beam from outside the wind tunnel to shine through the boundary layer on the plate, to the "return mirror," and back outside. Dimensions are given in figure 2. The maximum cross-section area of the model was slightly less than 3% of the test-section area and was thus considered to be marginally free from wall-induced flow distortion.

A cavity with a glass bottom was installed in the plate by replacing the section containing the window. Figure 3 shows sketches of the plate with and without the cavity, as it would be viewed from the center of the test section if the return mirror were removed. Figure 3 also shows the size and location of pins through which the flow was seeded with tracer particles for laser velocimeter measurements, of pins for increasing the boundary-layer turbulence, of "fences" for creating shear layers, and of the instrumentation probes.

Figure 4 further illustrates the construction of the probe supports. The position of the fixed probe with respect to the plate was manually adjusted by removing or inserting spacer blocks in the supporting strut, and sections of tubing between the strut and the tip. The movable probe was remotely adjusted in the x (downstream) and z (perpendicular to plate) directions.

The fences were porous spoilers intended to inhibit cavity resonance, as in references 1 and 4. Some of those configurations without the cavity also had a fence so that the shear layer could be studied. Additional fence details are given in figures 5 and 6.

The various model configurations are described in table 1, and photographs of several are presented in figures 7 through 11. Figure 11 shows the porous upstream wall of the cavity of Model 14 (one should not be confused by the reflections from the side wall). Air for this configuration and for Model 16 was drawn from a 6-atmosphere pressure supply and passed through a flow-measurement orifice plate, into a plenum chamber upstream of the cavity, through a fine-mesh screen, and through the 1.27-cm-thick porous wall into the cavity. Air for Model 15 passed from the plenum through a slot 3.8 cm below the plate surface into the cavity.

The model was constructed, mounted, and maintained during the tests by McDonnell-Douglas Corporation under contract to the Air Force Weapons Laboratory.

INSTRUMENTATION

Various instrumentation configurations were defined according to the type of sensor on the probe, the number of probes, and the type of optical measurements. These configurations are summarized in table 2. The rake had 20 total pressure tubes and 2 static pressure tubes distributed over a length of 16.4 cm for measuring the steady-state pressures in the boundary or shear layers. The "multiprobe" was a 0.5-cm tubular tip with provision for sensing steady-state and fluctuating values of both total and static pressures and with a hot wire at the tip for sensing temperature. The sensors labeled "hot wire" were mounted on individual tips and normally operated in pairs at high overheat ratios to sense changes in mass flux in the stream direction. The ball probe was a 0.3-cm-diameter balsa sphere cantilevered from the probe tip so as to transmit force fluctuations to electromagnetic coils and thereby sense the three components of velocity fluctuation. The "AF wire" was an Air Force sensor installed for calibration purpose only. The fixed probe and its support strut were removed when the probe was not required.

The laser-doppler velocimeter (LDV) provided the x and y components of velocity and the velocity fluctuations in the boundary layers, the shear layers, and the cavity. Since the LDV operated by analyzing the backscatter of light from particles in the flow, the return mirror was replaced by a window in order to reduce extraneous reflections. The optical degradation was evaluated in the form of modulation transfer function (MTF) and line-spread function(LSF). These measurements utilized the return mirror to obtain a double pass of a laser beam through the flow. Holograms were also made of the shear and cavity flows by means of windows in the sides of the cavity.

Table 3 lists the coordinates of orifices and transducers that were installed in the plate, cavity, and wind-tunnel wall opposite the model for sensing steady-state and fluctuating pressures. The steady-state pressures were measured with multiport scanivalves just outside the test section and were recorded along with operating conditions at the central computing facility. Corrections were applied to make the free-stream conditions correspond to those at the center of the plate with the model installed.

The fluctuating pressures were recorded on the system shown in figures 12, 13, and 14. Some of the other dynamic sensors itemized above also used those portions of the recording system that were appropriate. The differential pressure transducers were high impedance (above 5,000 ohms) with unamplified sensitivities of approximately 0.6 V per atmosphere of pressure. These transducers were all referenced to tunnel-static pressure. The signals were ac coupled before being amplified so that the amplifier gains could be maximized (up to 1,000). Most of the data were recorded after filtering out frequencies above 50,000 Hz to eliminate transducer "ringing" and other extraneous noise.

The present paper will be concerned only with the pressures on the plate, wall, cavity walls, rake, and selected steady-state pressures measured on the multiprobes.

TESTS

The tests were performed at free-stream Mach numbers from 0.6 to 0.9 and Reynolds numbers of 6.6 and 9.8 million/m (2 and 3 million/ft). The Reynolds number range was extended to 12 million/m for isolated cases. The total temperature of the wind-tunnel air stream was typically between 295 and 305 K.

Aerodynamic measurements with the probes and LDV were made only for selected model configurations which are noted in the last column of table 1.

RESULTS AND DISCUSSION

Steady State

Model and wall pressures without the cavity– The static-pressure coefficient C_p is presented in figures 15 through 32 for various locations on the plate and opposite wall of the wind tunnel for model configurations 1, 2, 3, 4, and 19. The optical test volume, which is of primary interest in the investigation, is about 10 cm wide in the region between the plate and return mirror from $x = 0$ to 20 cm. Nominal free-stream conditions correspond to a C_p of zero, which occurs near the center of the plate for most configurations. The least desirable result was a positive pressure gradient through the test volume, which retarded the flow and accelerated the growth of flow disturbances. A comparison of Model 4 (figs. 29 and 30) with Model 3 (figs. 27 and 28) shows that the return mirror supporting structure was primarily responsible for the gradient. The gradient was not as severe when the fixed probe and its strut were removed, such as in the Instrumentation 5 configuration (figs. 17 and 22). It was also not as severe with the turbulence-generating pins (figs. 15 and 20) as without (figs. 27 and 28). Reynolds number effects (figs. 15 and 16 or figs. 20 and 21) were typically negligible.

The pressure coefficient at $x = 20$ cm in figure 27 corresponds to a Mach number outside the boundary layer about 0.08 less than nominal. It will be shown later that a pressure gradient probably existed through the boundary layer, resulting in an even lower actual stream Mach number. The opposite extreme was observed when the fence was mounted (fig. 23). The pressure distribution on the opposite wall is evidence of a fairly consistent flow acceleration, presumably due to blockage by the model.

Figures 23 and 24 include an indication of the value of the pressure coefficient at which the local Mach number in isentropic flow would be unity.

It can be seen that several areas were supersonic, particularly the leading edge. The seeding pins were in the highest speed portion of the flow, resulting in an even larger disturbance than was produced by the turbulence-generating pins, as will be shown later. It is likely that the flow under the plate was choked at the highest test Mach number, but, because of the lack of lateral pressure gradient (e.g., fig 27), the flow in the test volume probably was not seriously affected.

Model and wall pressures with the cavity– Representative static-pressure coefficients for the cavity configurations are presented in figures 33 through 44. The effect of the cavity can be seen, by comparing figures 27 and 33 or 28 and 35, to have been fairly localized. The absence of the fixed probe in Instrumentation 7 (figs. 34 and 36) again decreased the pressure, but the effect was confined to the region downstream of the cavity. As will be shown in subsequent figures, Model 8 (figs. 33 to 36) had a severe resonance at Mach number of 0.89 and 0.60, while Model 14 (figs. 41 and 42), with a porous wall, did not. Most of the steady-state pressure levels were unaffected by the resonance.

The fences (figs. 37-40) generally decreased the downstream pressures. It should be noted that the fence of Model 2, while having approximately the same height as the Model 11 fence, was located farther upstream in relation to the return mirror and to the test volume. The two models thus simulate rather different flows at the test volume, even if the cavity were not present.

Static pressures in the boundary and shear layers– The velocities in the boundary and shear layers can be calculated from the total and static pressures. The latter were available from taps in the plate, cavity, and multiprobes. Typical results are shown in figures 45 through 48. "Plate" pressures for the cavity configurations have been obtained by interpolating between values upstream and downstream of the cavity.

The trend of the data indicates that, unlike the conventional assumption in boundary-layer calculations, the static pressure did increase somewhat with increasing distance above the plate. Some uncertainty remains because of the flow angularities likely to exist in the flow and because the multiprobes have only a single static hole.

Velocity profiles without the cavity– The ratios of local velocity to velocity at the tip of the rake were calculated from rake pressure readings and from free-stream total temperature data, and are presented for the configurations with no cavity in figures 49 through 57. Because of the uncertainty noted in the previous section, the static pressures were assumed equal to that on the surface of the plate. Since the static pressure is probably underestimated at the tip, the velocity ratios are probably also underestimated near the plate, by an amount on the order of 0.03. A smaller error was caused by ignoring the total temperature that would be expected on approaching the wall. Another source of inaccuracy was the large flow angularity behind the fence, where even the total pressure readings were likely to be underestimated. Despite these uncertainties, the relatively large effects of the various model alterations are easy to discern, and the trends are clear.

Figure 49 shows that the turbulence-generating pins roughly tripled the height of the boundary layer. Unfortunately, the seeding pins were even more effective in producing velocity decrement, and the combination of both types of pins produced a layer approximately four times the thickness of Model 19 with a reverse curvature over part of the velocity profile. Hence, the boundary layers have been thickened as desired but cannot be considered representative of normal boundary layers. Figure 50 illustrates the large fence effects but negligible return-mirror effects, despite the expected instability from the adverse streamwise pressure gradient.

The change in boundary layer from front to back of the test volume is seen in figure 52 to be negligible for models with no fence, and small for the fence configurations. Reynolds number effects were negligible (fig. 53), and increase in Mach number generally caused only small changes in boundary-layer thickness (figs. 54 to 57). It should be stressed that the conclusions about Reynolds and Mach number do not necessarily apply to other situations, such as the natural boundary layer on an airplane fuselage.

Velocity profiles with the cavity– Velocity profiles for the cavity configurations are presented in figures 58 through 64. The profile for Model 8 or Model 14 shown in figure 58 was only slightly modified from the corresponding profile without cavity, Model 3 in figure 49. Figure 58 shows that the shear layer thickness increased with fence height and decreased as porosity increased.

It was possible to lower the rake into the cavity, and figure 59 shows typical results. When static pressures measured in the upper part of the cavity were used in the velocity calculations, the values were changed to those shown by the dotted line. The uncertainty of not knowing the applicable static pressure either in the cavity or at the rake tip raises doubts about the usefulness of the cavity-velocity calculations. This is one area where the laser velocimeter gave much more precise results than is possible from pressure measurements.

The change in the velocity profile from upstream to downstream of the Model 8 cavity is shown in figure 60, and the Mach number effect is shown iin figure 61. Similar effects appear for Model 13 in figures 63 and 64. The Mach number effect for Model 8 is actually very much like that for Model 3 (fig. 56). The effect of streamwise location appears more significant with the larger fence of Model 11 (fig. 62), but the cross-hatched areas indicate that the effect may be illusory due to uncertainties in static pressure.

Lateral distribution of velocities– Velocities were also computed from rake pressure with the rake rotated 90°, as in figure 1. Representative values are shown in figures 65 through 68. A non-uniformity is evident in the distributions of figure 65 that is unaffected by Reynolds number and only slightly by Mach number. The primary difference from a straight line appears to be a loss in velocity over a lateral distance of the order of the 10-cm width of the combined seeding pin wakes. The effect is similar for the vastly different Models 1 and 13 (figs. 66 and 68) but is inverted or possibly nonexistent behind the large fence of Model 2 (fig. 67). Care will have to be exercised in interpreting measurements that extend over appreciable lateral distances.

Dynamic

Pressure fluctuations without the cavity– The root-mean-square (rms) values of the model and wall pressures were normalized by free-stream dynamic pressure and are presented for the no-cavity configurations in figures 69 through 82. Most of the rms averaging covers the frequency range 1 to 50,000 Hz. A few of the measurements made without the 50,000 Hz low-pass filters are included because of the unavailability of filtered data and are identified with the label "wideband."

The higher rms values are associated with flow separation from the seeding and turbulence-generating pins and, at the two highest test Mach numbers, with shock-wave movement over the nose region. The wind tunnel generated noise which established a "floor," or minimum rms value, below which model-generated fluctuations could not be discerned. The coefficients for regions near the test volume generally increased as Mach number decreased (e.g., figs. 69, 71, 72, and 73); the only significant Reynolds number effects occurred at low Mach numbers (figs. 73 and 74) downstream from the test volume.

One might expect higher rms levels for those configurations with the more adverse steady-state pressure gradients. Only at the low Mach number did the removal of the return mirror show an appreciable effect (figs. 78 and 80), and this was confined to regions behind the test volume. It is noteworthy that the surface fluctuations downstream from the fence (figs. 75 and 76) were not really increased much by the fence. This, of course, was a protected region not typical of that farther out in the shear layer.

Pressure fluctuations with the cavity– The fluctuating-pressure coefficients are given in figures 83 through 101 for the cavity configurations. Figure 83 summarizes the cavity data for all configurations, indicating the superiority of Models 11 and higher (Model 15 was improved with air injection). The results in figure 83 are not to be considered a guide to configuration optimization for the general case. Certainly, it is desirable to minimize simultaneously the cavity fluctuations and the thickness of shear layer which the optical beam must traverse. However, the relatively thick boundary layer and low incidence of the flow approaching the cavity unduly enhanced the effectiveness of the wall porosity of Model 14. Earlier tests of reference 1 have shown that acoustic absorption in the cavity walls loses some of its effectiveness at certain angles of incidence. It is also evident the fence height has not necessarily been reduced to the optimum size. The lowest fence, such as on Model 13, had a height equal to 15% of the cavity length, or about twice what reference 1 recommends. It is also twice the height of the fence, relative to cavity length, normally used with the cavity described in reference 5. Unlike the fences in the references, the Model 13 fence was much smaller than the approaching boundary layer (actually between one and two times the displacement thickness). Even the effects of porosity cannot be generalized in this situation. The variety of configurations do provide representative flows over the cavity with which to evaluate optical degradation and the relationship with aerodynamic disturbances. Thus, Models 8 and 14 produced a range of cavity disturbance with a minimum thickness of shear layer, while Models 11 and 13 produced a range of fence-initiated shear-layer thickness with little cavity disturbance.

Resonance conditions for Model 8 are shown in figures 84, 85, 88, and 89, with the higher cavity response at the lower Reynolds numbers. It might be noted that the average fluctuation levels in the cavity correspond to 3 or 4% (higher value at the lower Reynolds number) of the average cavity pressure at $M = 0.89$ and about 2% at $M = 0.60$. The fences on Models 10, 11, 12, and 13 (figs. 90 through 96) were all reasonably effective in keeping the cavity fluctuations small, the fluctuations being approximately equal to the minimum on the plate.

As noted previously, the porous wall of Model 14 (figs. 97 and 98) also kept the rms levels low. Some insight into the phenomenon is provided by the data of figure 101, which shows that as air was injected through the porous cavity wall, the wall was effectively made solid, and the cavity resonated. Additional air injection provided a shear layer, which acted as an alternate mechanism for inhibiting resonance. The smaller slit of Model 15 lacked the powers of acoustic absorption at zero mass flow but was very effective in distributing a small amount of air so as to inhibit resonance.

Pressure spectra– Tape recordings of some of the data have been analyzed for frequency content on an analog-digital combination spectral analyzer described in references 6 and 7. The spectral densities were derived from true integrations of the signals when passed through 106 synthesized bandpass filters centered on frequencies from 10 to 20,000 Hz. Bandwidths varied from 2 to 800 Hz. The corresponding integration times were from 16 to 2 sec, giving statistical errors of less than 16%. The analyses are presented on staggered axes in figures 102 through 111.

The wall-pressure spectra in figure 102 are representative of the tunnel-empty spectra except for the 420-Hz peak at the two lower Mach numbers, which represents the cavity resonance radiating across the wind tunnel. The main noise peaks occurred at frequencies from 980 to 860 Hz, varying with, but not exactly proportional to, velocity. These peaks correspond approximately to measurements in other investigations (e.g., ref. 4) and were not generated by the model. In addition, a sizable peak–possibly a first harmonic–appeared at 1,800 Hz at the lowest Mach number. The spectra at low frequency, while being relatively high in amplitude, do not cover a broad enough frequency range to be as significant as the plots might make them appear.

The tunnel-generated noise peaks are prominent in the spectra for the center of the plate (fig. 103) along with a peak at 13,600 Hz at the lower Mach numbers. The latter is presumed to be associated with vortex shedding off the seeding pins, although the shedding frequency was uncertain due to the flow accelerations and decelerations near the pins. Figure 104 shows that the tunnel noise peaks and the pin-shedding peaks appeared in the spectra for the plate leading edge but were obliterated at the higher Mach numbers, where shock-wave movement was the primary disturbance.

Figures 105 and 106 show the spectra for pressures in the cavity (FP123), downstream from the cavity (FP110), and upstream of the cavity (FP109). The predominant feature is the resonance peak, 1,200 Hz for high Mach number and 420 Hz for low Mach number. Figure 105 also exhibits a harmonic at 2,400 Hz and a lower mode at 500 Hz, while the low Mach number data in figure 106 contains tunnel noise, harmonics, and the pin-shedding peak. It is worth noting that for either Mach number the single predominant peak in the cavity-pressure data contained over three-fourths of the total energy in the entire spectrum.

The fences served primarily to reduce the amplitude of the peaks previously identified. With the high fence of Model 11 (fig. 107) the 420-Hz resonance frequency remained the predominant feature in the cavity data, while the 1,800-Hz frequency, assumed to be tunnel noise, persisted outside the cavity. The latter frequency appeared in much of the low Mach number data, both with and without the fence, and with and without the cavity, at a variety of locations on the model. With the low fence of Model 13, figure 108 shows both resonance frequencies of 420 and 1,200 Hz in the cavity; the main spectral peaks outside the cavity were at 420 and 980 Hz (tunnel noise). A low-frequency mode, 380 Hz appears at low Mach numbers in figure 109, as does the 1,800 Hz noise.

The porous wall changed the frequency of response of the cavity somewhat. At high Mach number, figure 110 shows that the predominant response was at 580 Hz with or without air injections; the air also excited a higher mode in the cavity at 1,020 Hz. At $M = 0.60$ (fig. 111) the primary cavity responses were at 500 Hz and, with no air injections, 1,400 Hz.

Phase relationships in resonance– Additional information about the cavity resonances at Mach numbers of 0.89 and 0.60 is presented in figure 112. Phase angles were determined from a cross-spectral analysis at the same time that the spectral densities in the previous section were obtained. If the pressure is assumed to vary sinusoidally, the phase can be considered equivalent to time and is shown as such in the upper part of the figure. If the pressure disturbance were to travel at the speed of sound across the cavities sketched in the lower part of the figure, the instantaneous pressure would vary as shown in the upper part of the figure. The corresponding locations of maximum and one-half maximum pressure values are sketched in the cavity diagrams, using a dashed line for negative values. It can be deduced that the high Mach number resonance is a fore-aft mode and the low Mach number resonance is largely a depth mode, such as that in an organ pipe. Although not shown, Reynolds number effects were negligible, the low Reynolds number data yielding phase angles within 5° of the high Reynolds number data.

CONCLUDING REMARKS

Transonic tests have been performed on a flat plate with a cube-shaped cavity for the purpose of correlating the optical-propagation losses with the aerodynamic properties of the flow over the plate and cavity. This paper has presented a model description and some of the test results, primarily velocity profiles and pressure data for the model.

A variety of flow conditions was created by numerous model alterations. Pins near the plate leading edge thickened the natural boundary layer by a factor of 3 or 4. Shear layers of widely differing thicknesses were generated by fences of various heights and porosities. Large pressure disturbances, from 2 to 4% of the average pressure, were produced when the cavity resonated in a fore-aft mode at a Mach number 0.89 and in a depth mode of 0.60. The resonance was greatly attenuated by cavity-wall porosity, by air injected into the cavity, and by most of the fences. The models thus provided cavity flows with all combinations of large and small cavity disturbances and large and small shear layers. The frequencies for resonance, as well as for pin-shedding and wind-tunnel-generated noise, were identified by spectral analyses of the pressures.

A Reynolds number variation of 50% was shown to have negligible effect on the velocities and pressure coefficients pertaining to flow through the optical-test volume, except for the condition of strong cavity resonance. It was also shown that a longitudinal pressure gradient caused by the mirror and probe supports had little effect on the flow through the test volume other than lowering the test Mach number. The consequences of ignoring a static-pressure gradient in the flow layers and in the cavity were discussed. Lateral velocity gradients were also identified and discussed.

Ames Research Center
National Aeronautics and Space Administration
Moffett Field, California 94035, July 11, 1978

REFERENCES

1. Van Kuren, James T.; Otten, Capt. L. J., III; Davis, Lt. James A.; and Kyrazis, Col. Demos: Acoustic Phenomena of Open Cavity Airborne Cassegranian Telescopes. AIAA Paper 74-195, Jan. 1974.

2. Otten, L. J.; and Van Kuren, J. T.: Artificial Thickening of Transonic Boundary Layers. AIAA Paper 76-51, 1976.

3. Johnson, D. A.; and Rose, W. C.: Turbulence Measurements in a Transonic Boundary Layer and Free-Shear Flow Using Laser Velocimetry and Hot-Wire Anemometry Techniques. AIAA Paper 76-399, July 1976.

4. Buell, Donald A.: An Experimental Investigation of the Airflow Over a Cavity With Antiresonance Devices. NASA TN D-6205, 1971.

5. Buell, Donald A.: Airloads Near the Open Port of a One-Meter Airborne Telescope. AIAA Paper 75-71, Jan. 1975.

6. Lim, Raymond S.; and Cameron, William D.: Power and Cross-Power Spectrum Analysis by Hybrid Computers, NASA TM X-1324, 1966.

7. Chyu, Wei J.; and Hanly, Richard D.: Power- and Cross-Spectra and Space-Time Correlations of Surface Fluctuating Pressures at Mach Numbers Between 1.6 and 2.5. NASA TN D-5440, 1969.

TABLE 1.– MODEL CONFIGURATIONS

No.	Seed pins	Turbulence-generating pins	Return mirror	Fence height, cm	Fence porosity	Fence hole diameter, cm	Cavity	Upstream wall porosity	Upstream wall hole diameter, cm	Step height, cm	Probe measurement
1	X	X	X	—	—	—	—	—	—	—	X
2	X	—	X	5.1	0.49	0.37	—	—	—	—	X
3	X	—	X	—	—	—	—	—	—	—	—
4	X	—	—	—	—	—	—	—	—	—	—
5	X	—	—	5.1	0.49	0.37	—	—	—	—	—
6	X	X	—	—	—	—	—	—	—	—	—
7	X	—	X	5.1	0.53	0.95	—	—	—	—	—
8	X	—	X	—	—	—	X	0	—	—	X
9	X	—	X	2.3	0.38	0.24 slits	X	0	—	—	—
10	X	—	X	2.3	0.38	0.52	X	0	—	—	—
11	X	—	X	4.6	0.38	0.52	X	0	—	—	X
12	X	—	X	4.6	0.58	0.99	X	0	—	—	—
13	X	—	X	2.3	0.58	0.99	X	0	—	—	X
14	X	—	X	—	—	—	X	0.49	0.32	—	X
15	X	—	X	—	—	—	X	—	0.64 slot	—	—
16	X	—	X	2.3	0.58	0.99	X	0.49	0.32	—	—
18	—	—	X	—	—	—	—	—	—	0.64	—
19	—	—	X	—	—	—	—	—	—	—	—
20	—	X	X	—	—	—	—	—	—	—	—
21	—	X	X	—	—	—	—	—	—	0.64	—

TABLE 2.– INSTRUMENTATION CONFIGURATIONS

No.	On movable probe	On fixed probe	On cavity probe	Optics
1	Rake	Ball	—	—
2	Multiprobe	Multiprobe	—	—
3	Hot wire	Hot wire	—	LDV
4	—	—	—	LDV
5	Rake	—	—	MTF, LSF
6	Rake	—	—	Holograms
7	Rake	—	—	MTF
8	Rake	AF wire	—	Holograms
9	Hot wire	—	Hot wire	LDV
10	Ball	AF wire	Hot wire	LDV

TABLE 3.– SPLITTER-PLATE PRESSURE-INSTRUMENTATION COORDINATES

Pressure tap	x_p, cm (from leading edge)	y_p, cm (from centerline)	z_p, cm (from upper surface)	Transducer	x_p, cm (from leading edge)	y_p, cm (from centerline)	z_p, cm (from upper surface)
Upper surface							
P100	1.3	0	0	—	—	—	—
P101	2.5			—	—	—	—
P102	3.8			—	—	—	—
P103	15.2			FP103	15.2	0.4	0
P104	20.1	0.5		FP104	20.1	0	
—	—	—	—	FP204	20.1	1.0	
—	—	—	—	FP304	20.1	1.9	
P105	43.2	0	0	—	—	—	—
P106	68.6			—	—	—	—
P107	96.5			—	—	—	—
P108	118.4			FP108	118.4	-0.6	0
P109	137.5	-0.4		FP109	137.5	0	
P110	157.1	-0.4		FP110	157.1	0	
P111	175.3	0		FP111	175.3	-0.6	
P112	195.6	0		—	—	—	—
P113	118.4	5.8		FP113	118.4	5.1	0
P114	118.4	20.3		—	—	—	—
P115	118.4	30.5		—	—	—	—
P116	147.3	7.6		FP116	147.3	7.0	0
P116A	147.3	13.1		FP116A	147.3	12.7	
P117	175.3	7.6		FP117	175.3	7.0	
P119	175.3	30.5		—	—	—	—
Cavity							
P120	139.7	0.2	-4.8	FP120	139.7	0.2	-4.8
P121	139.7	0.2	-11.8	FP121	139.7	0.2	-11.8
P122	154.9	0.2	-4.8	FP122	154.9	0.2	-4.8
P123	154.9	0.2	-11.8	FP123	154.9	0.2	-11.8
Lower surface							
P126	43.2	20.3	-2.5	—	—	—	—
P127	68.6	20.3		—	—	—	—
P128	96.5	20.3		—	—	—	—
Opposite wall							
P130	85.6	5.8	—	—	—	—	—
P131	116.2	0.7	—	FP131	111.8	1.4	—
P132	168.8	-1.2	—	FP132	170.2	-1.4	—
P133	183.0	-1.2	—	—	—	—	—

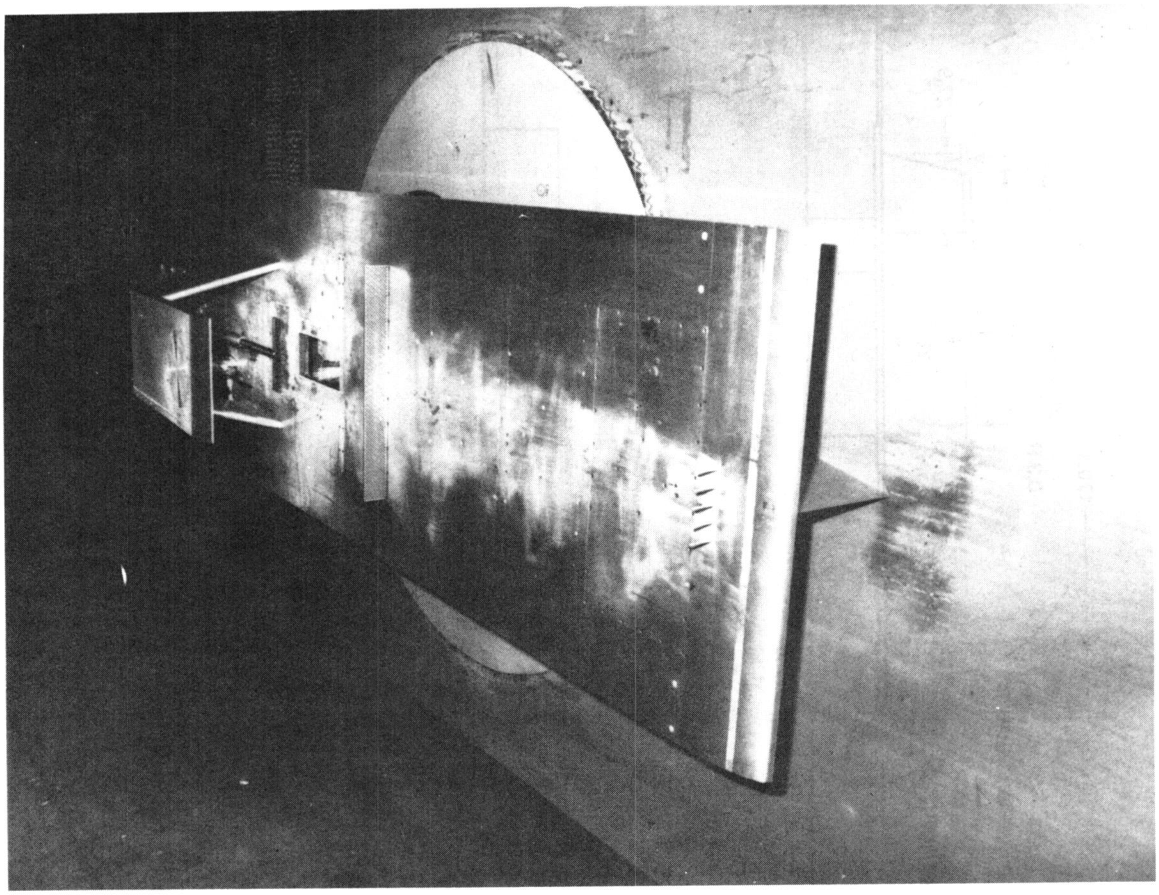

Figure 1.– View looking downstream of model on wind-tunnel wall.

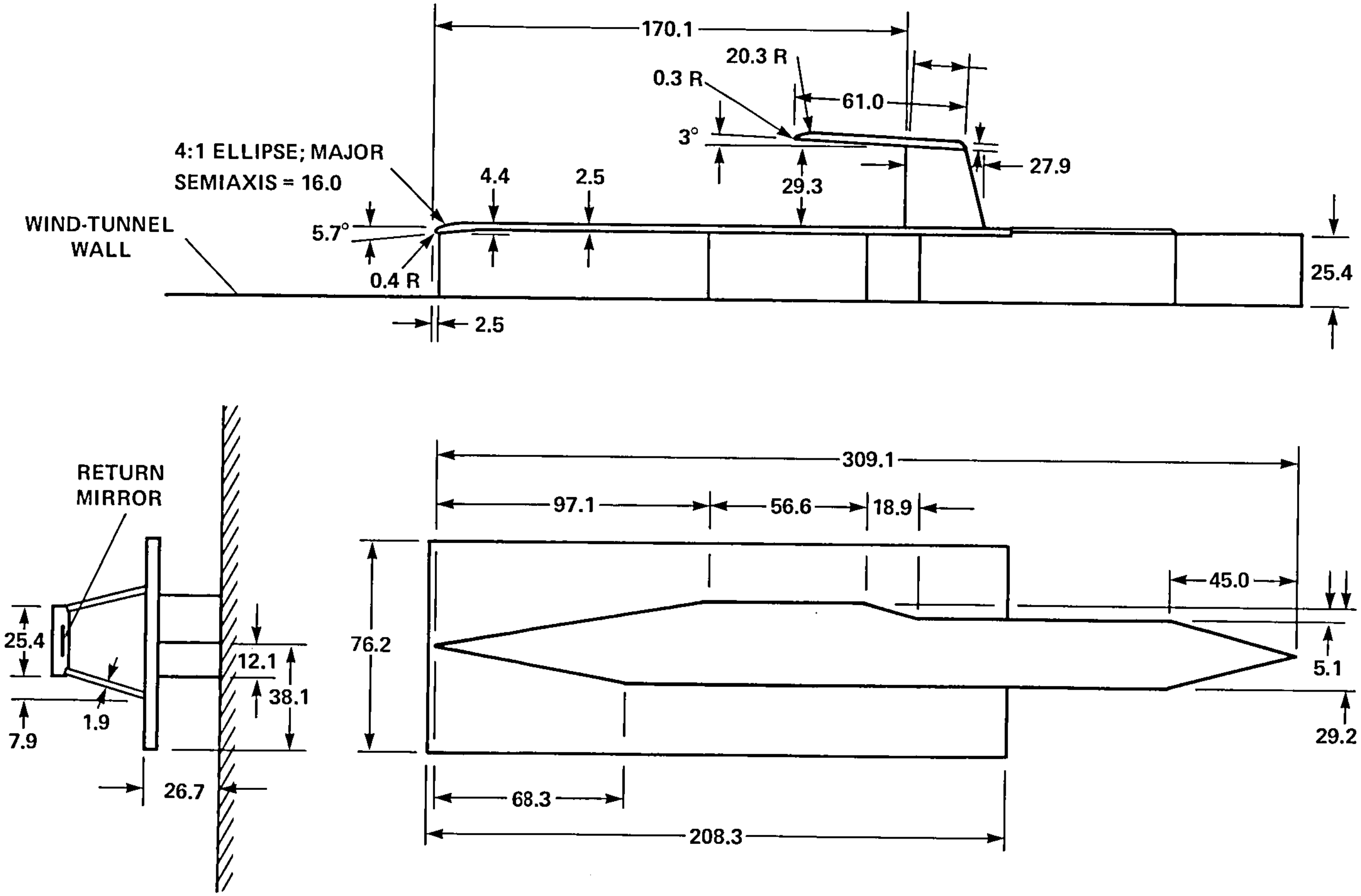

LINEAR DIMENSIONS IN cm

Figure 2.– Three-view drawing of the model with return mirror.

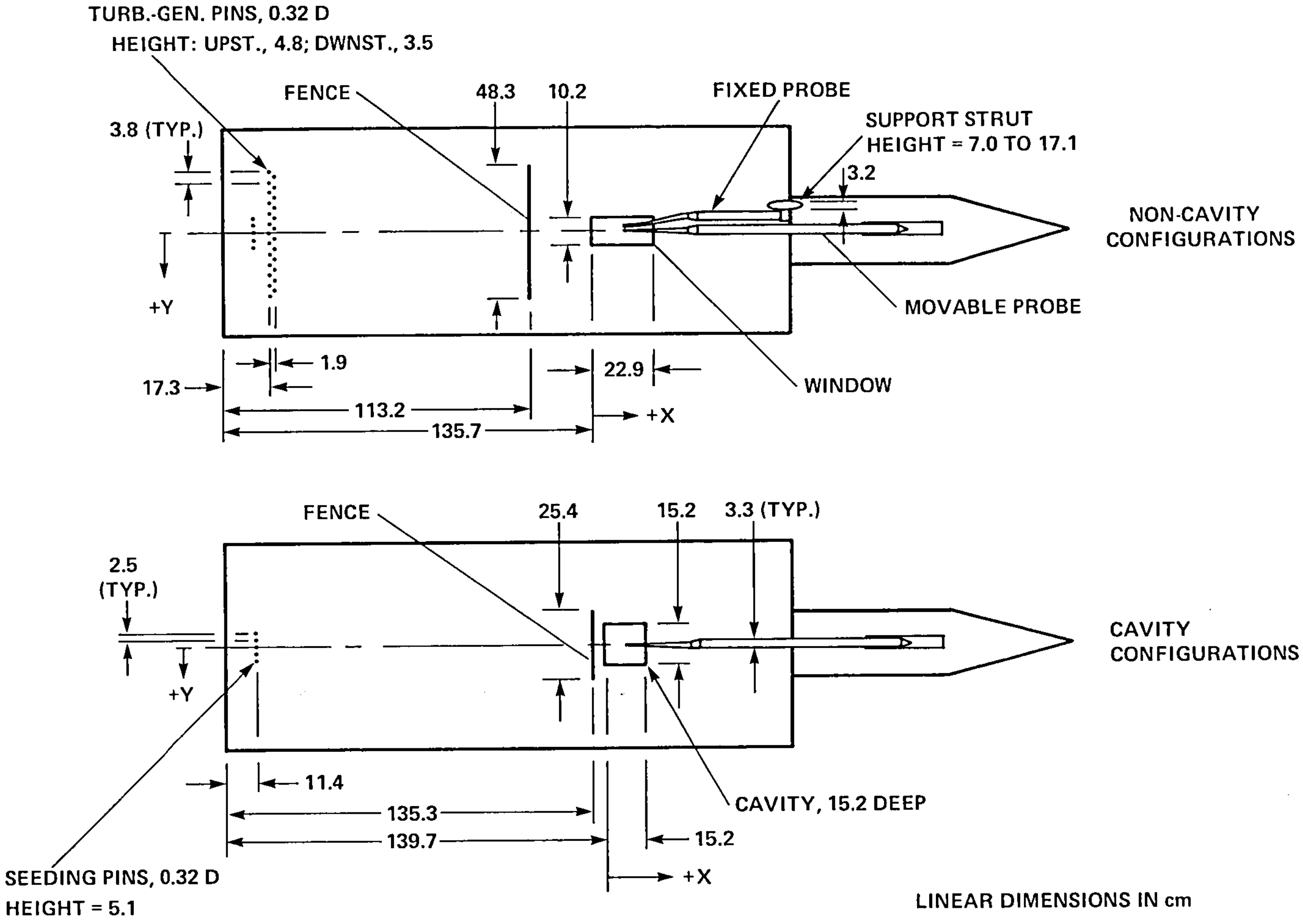

Figure 3.– Top views of the model without return mirror.

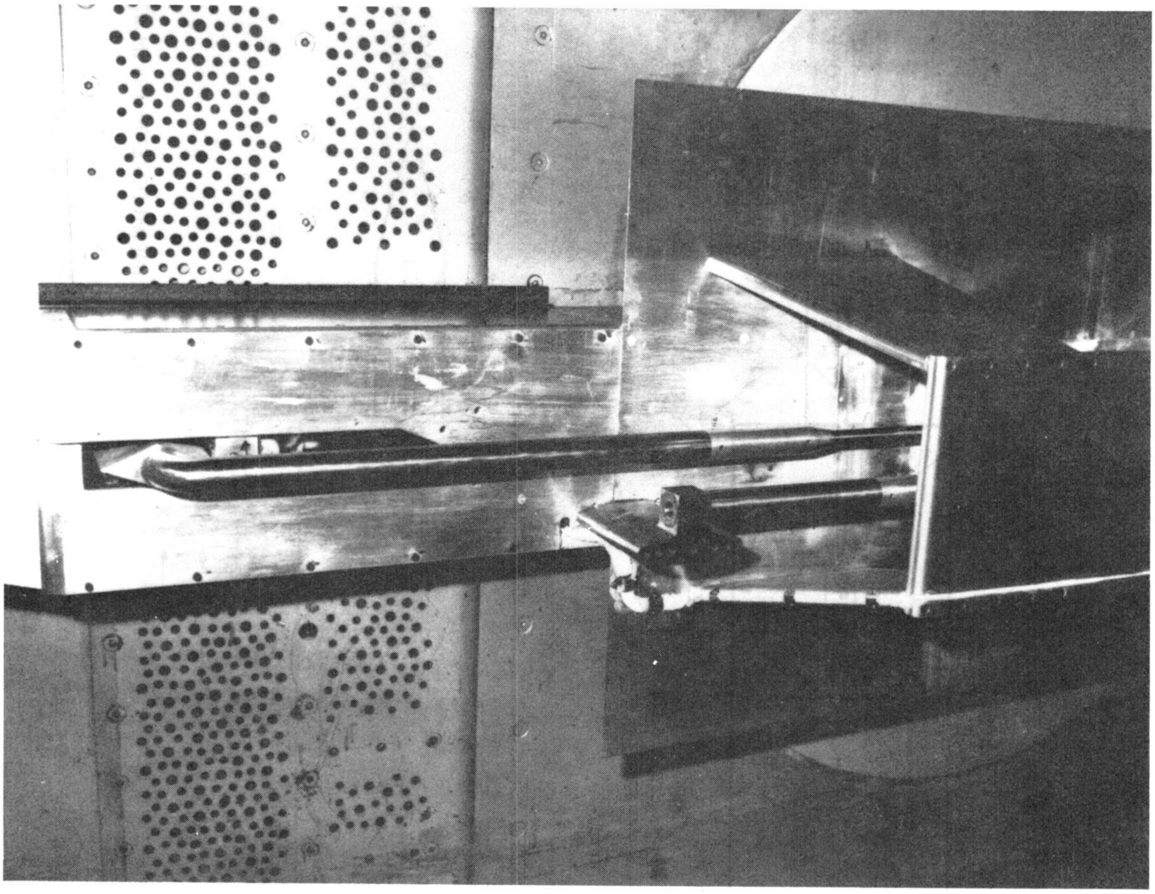

Figure 4.– View from top of probe supports.

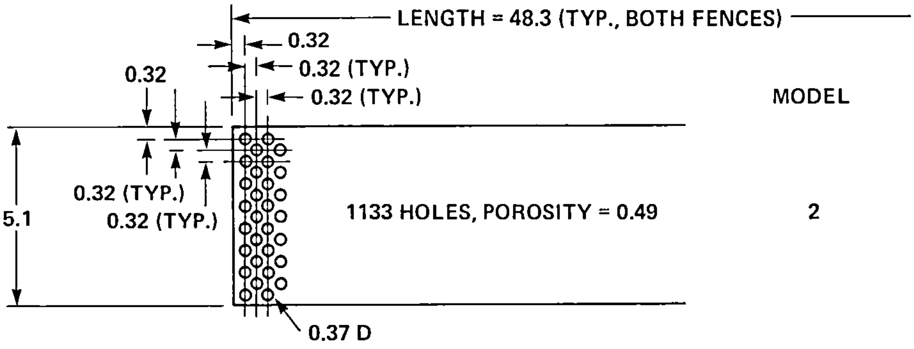

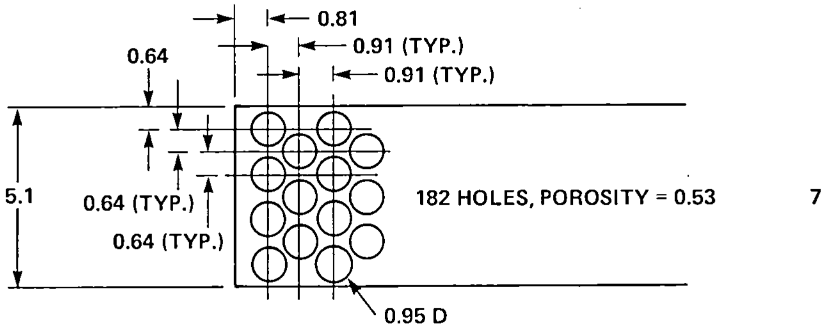

LINEAR DIMENSIONS IN cm

Figure 5.– Sketch of the no-cavity fences; thickness = 0.46 cm.

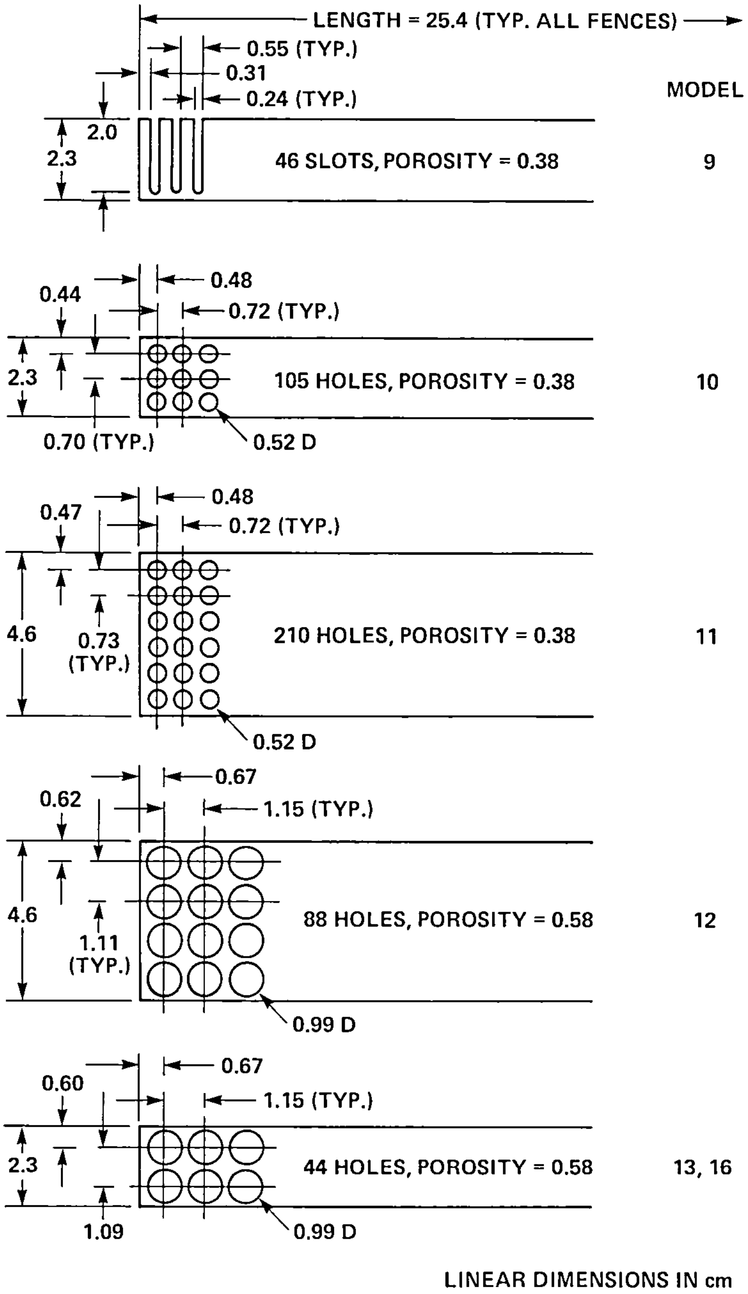

Figure 6.— Sketch of the cavity fences; thickness = 0.48 cm.

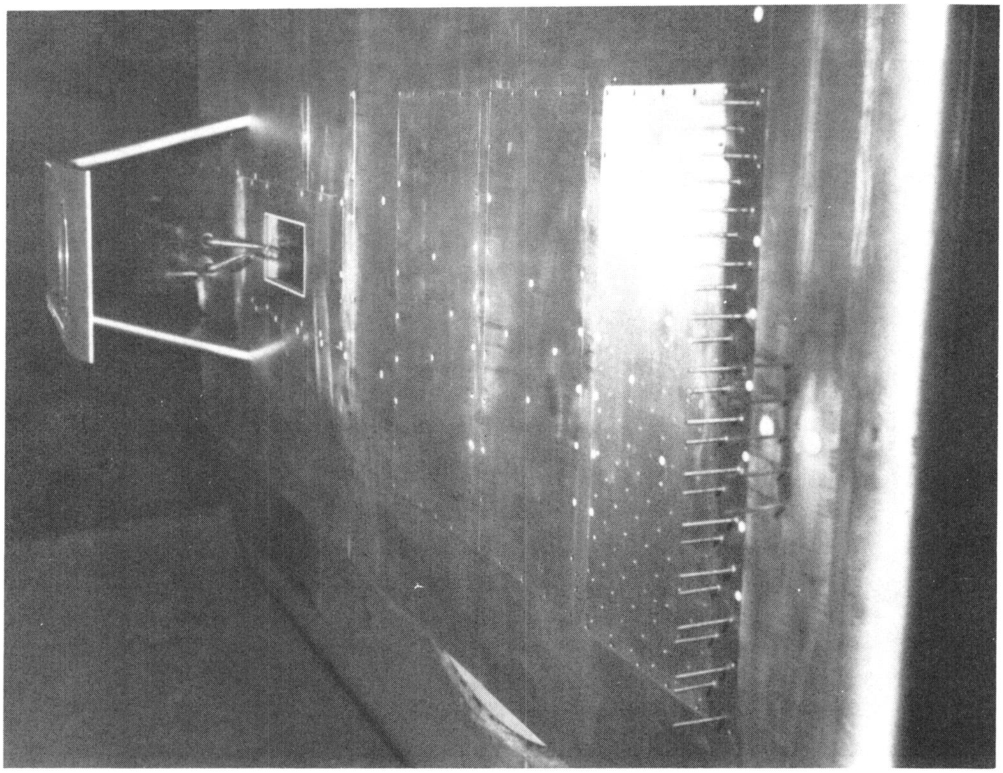

Figure 7.– Model 1, Instrumentation 2.

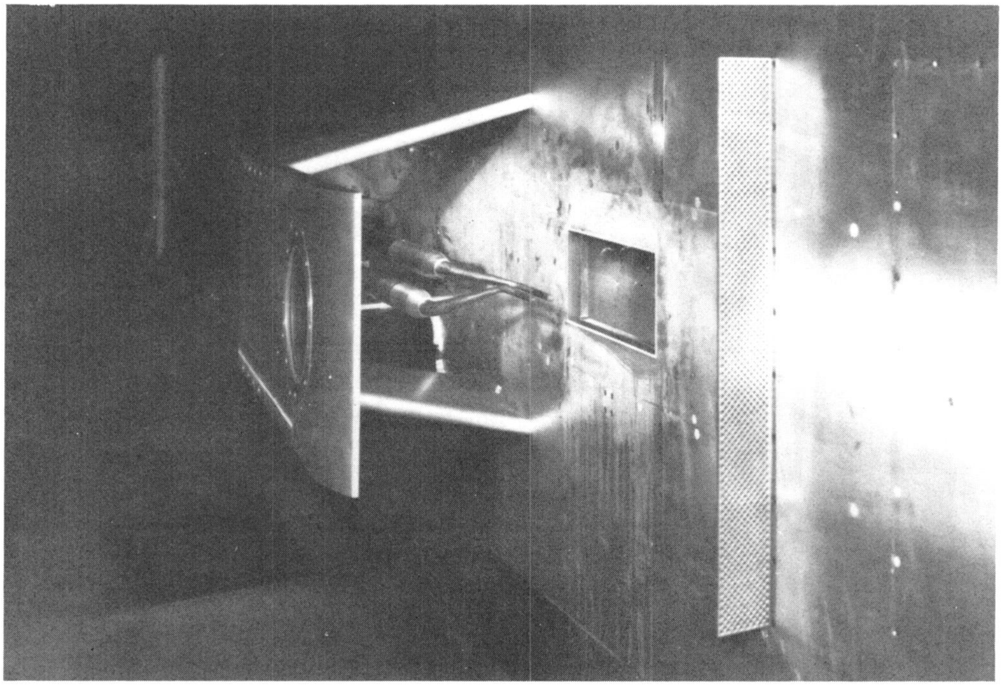

Figure 8.– Model 2, Instrumentation 3.

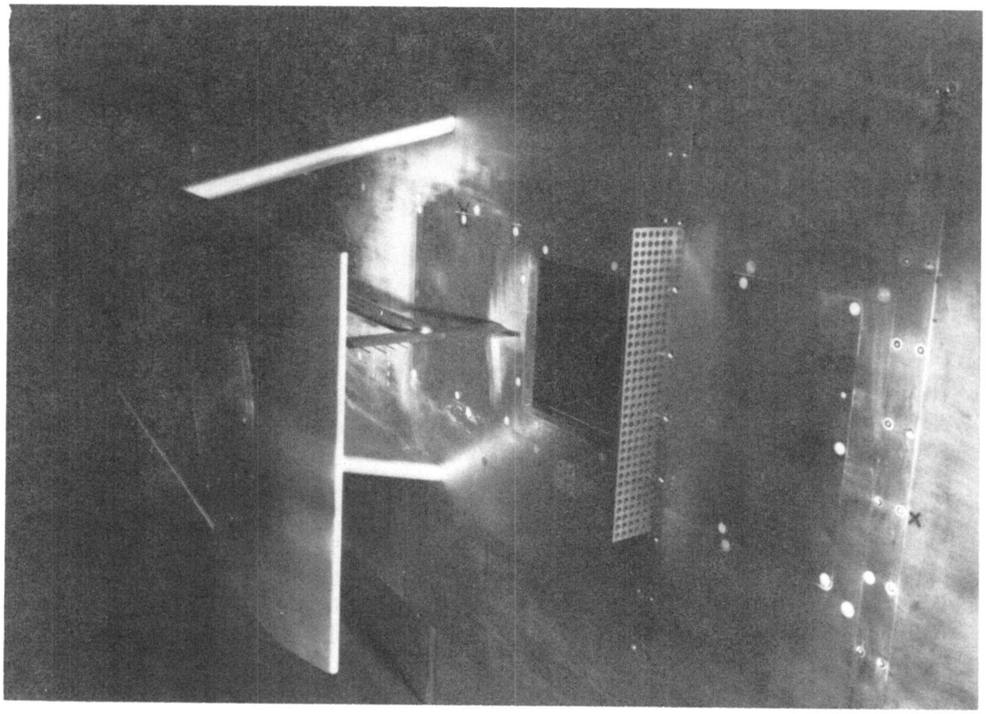

Figure 9.– Model 11, Instrumentation 7.

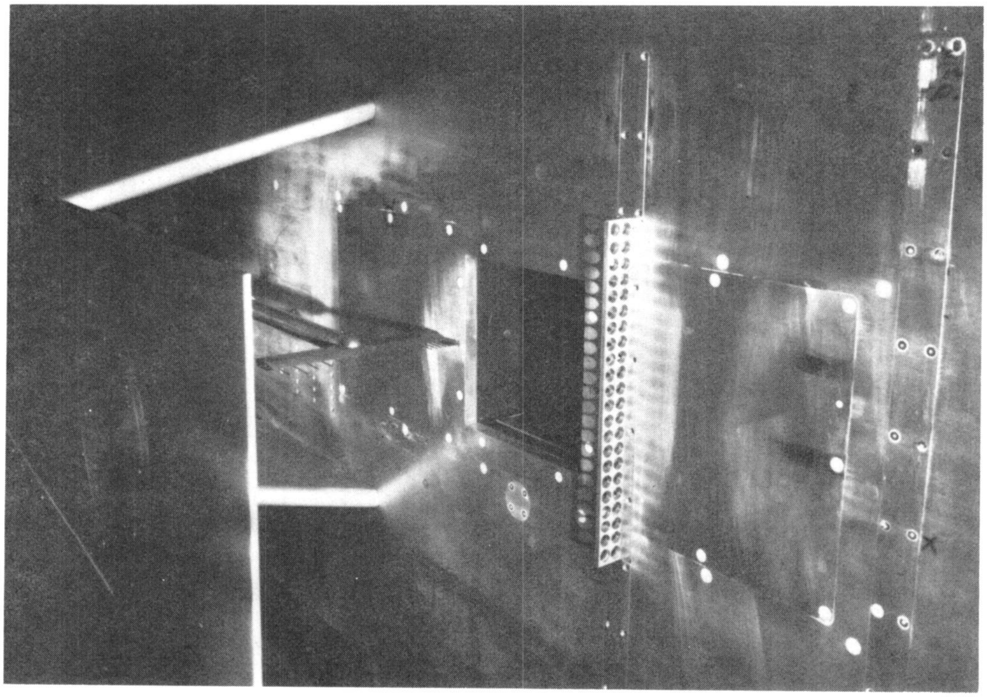

Figure 10.– Model 13, Instrumentation 7.

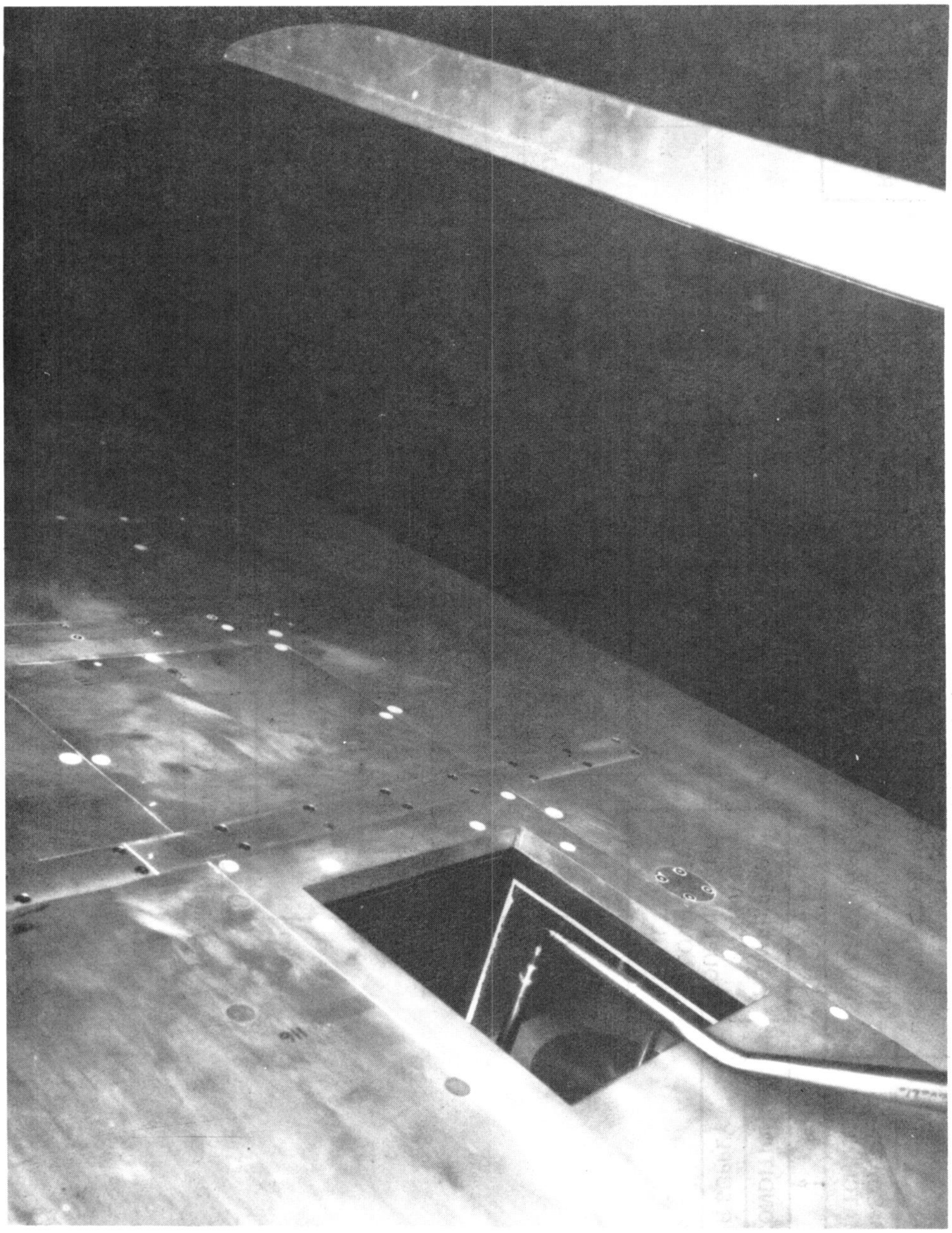

Figure 11.– Model 14, Instrumentation 9.

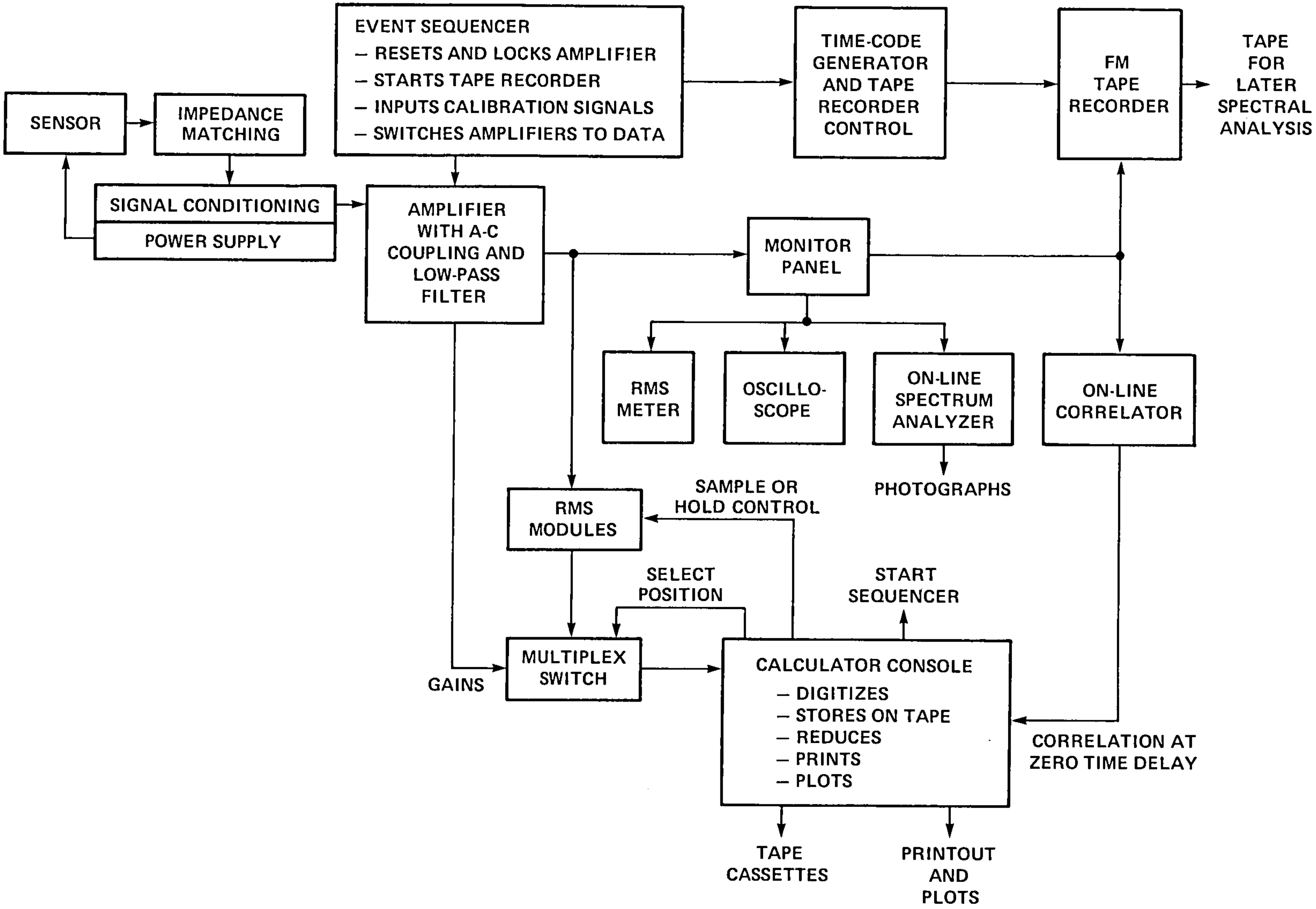

Figure 12.– Typical dynamic-instrumentation channel.

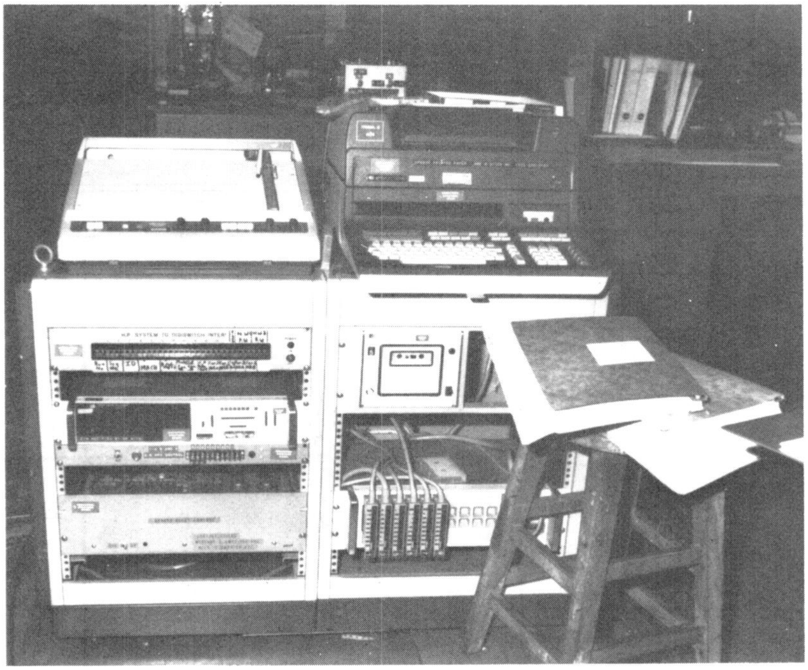

Figure 13.– Calculator console for dynamic data control.

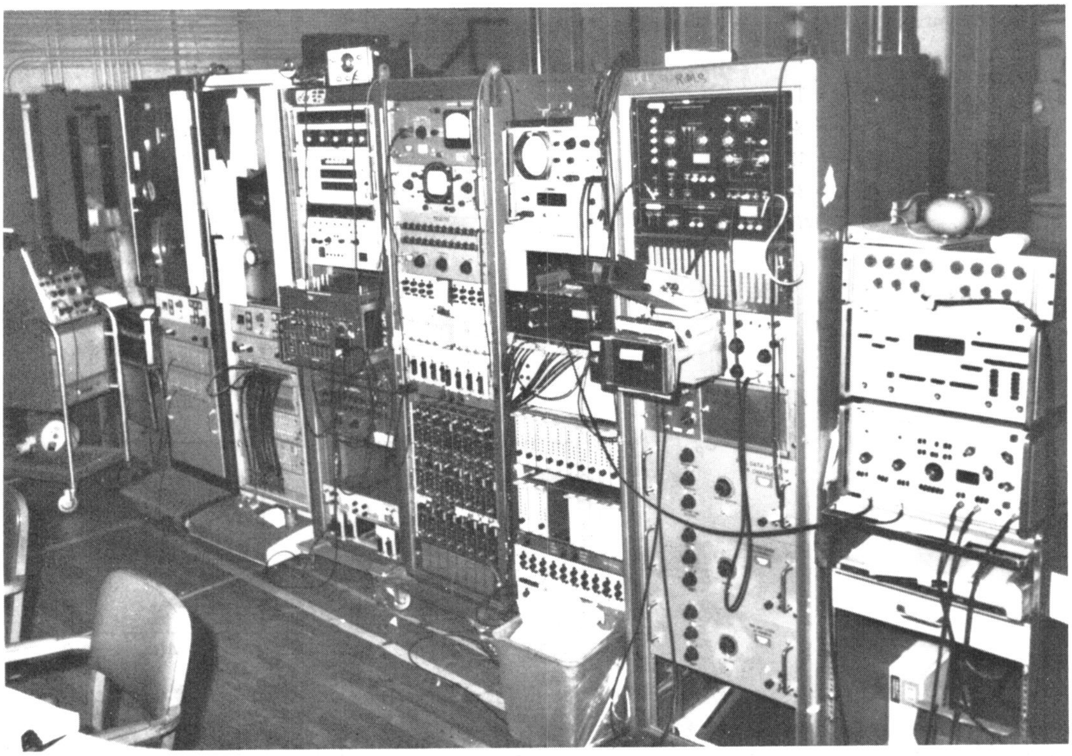

Figure 14.– Recording and analysis equipment for dynamic data.

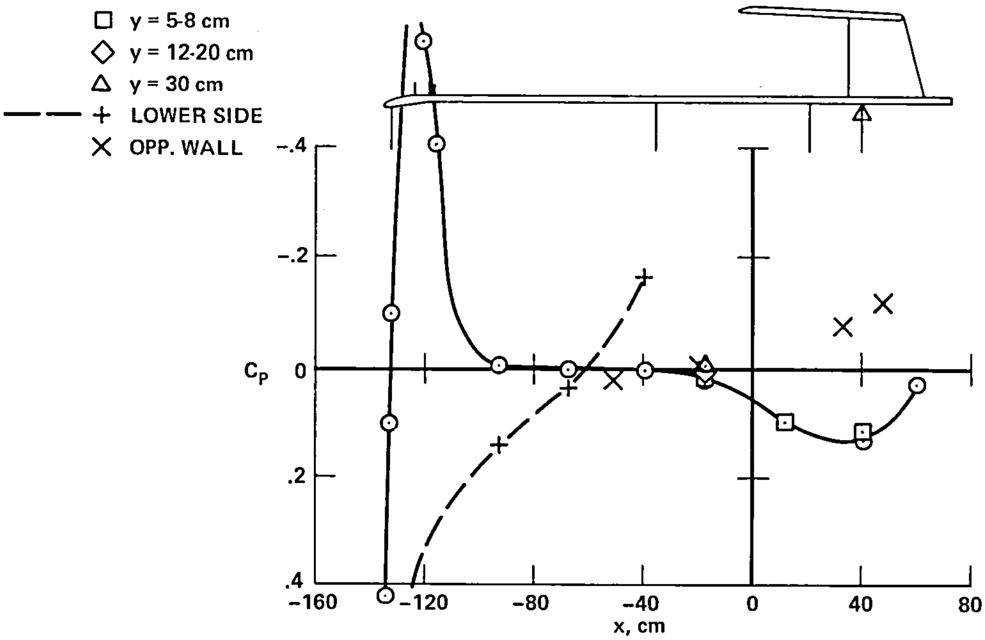

Figure 15.– Static-pressure coefficient on plate and wall; Model 1, Instrumentation 1, $M = 0.89$, $R = 9.7 \times 10^6$/m.

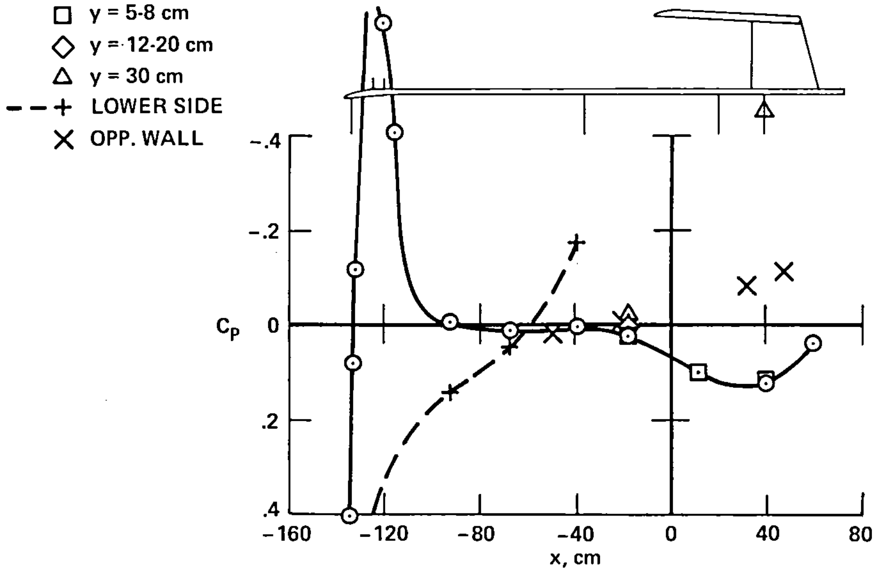

Figure 16.– Static-pressure coefficients on plate and wall; Model 1, Instrumentation 1, $M = 0.89$, $R = 6.5 \times 10^6$/m.

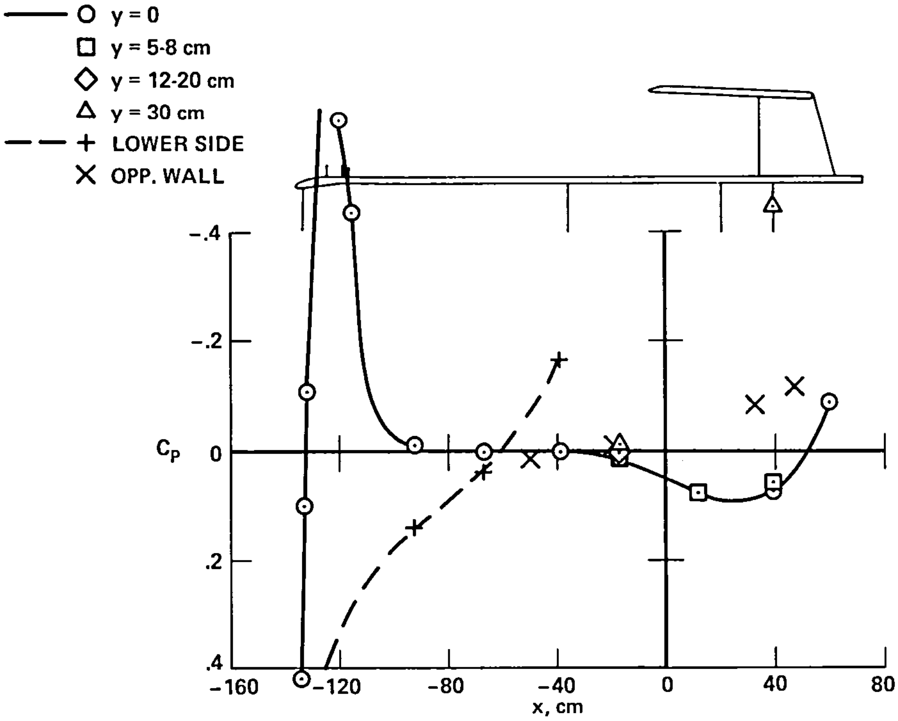

Figure 17.– Static-pressure coefficients on plate and wall; Model 1, Instrumentation 5, $M = 0.89$, $R = 9.8 \times 10^6$/m.

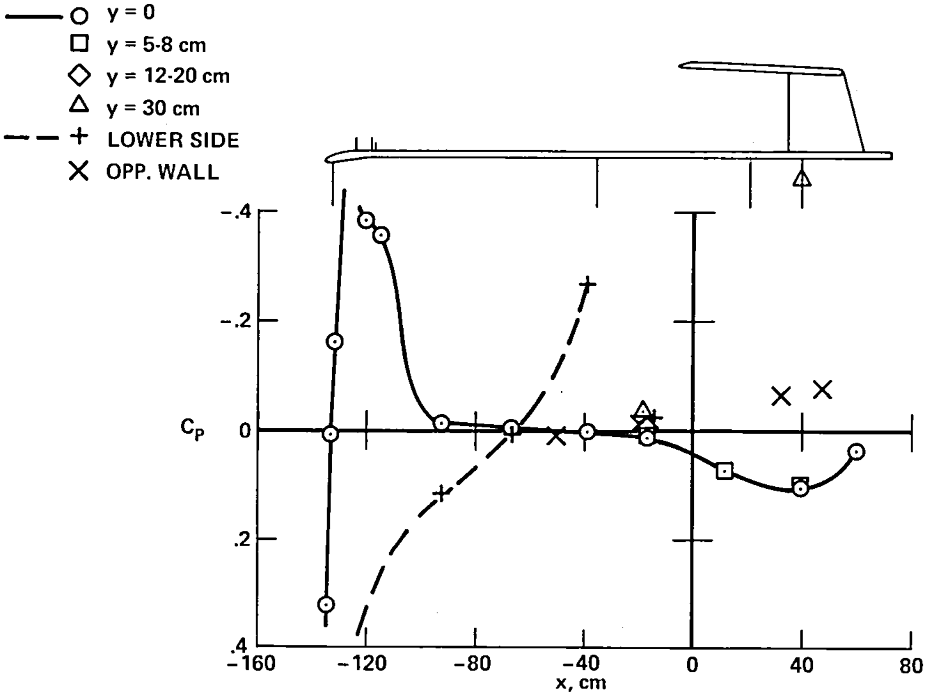

Figure 18.– Static-pressure coefficients on plate and wall; Model 1, Instrumentation 1, $M = 0.79$, $R = 9.9 \times 10^6$/m.

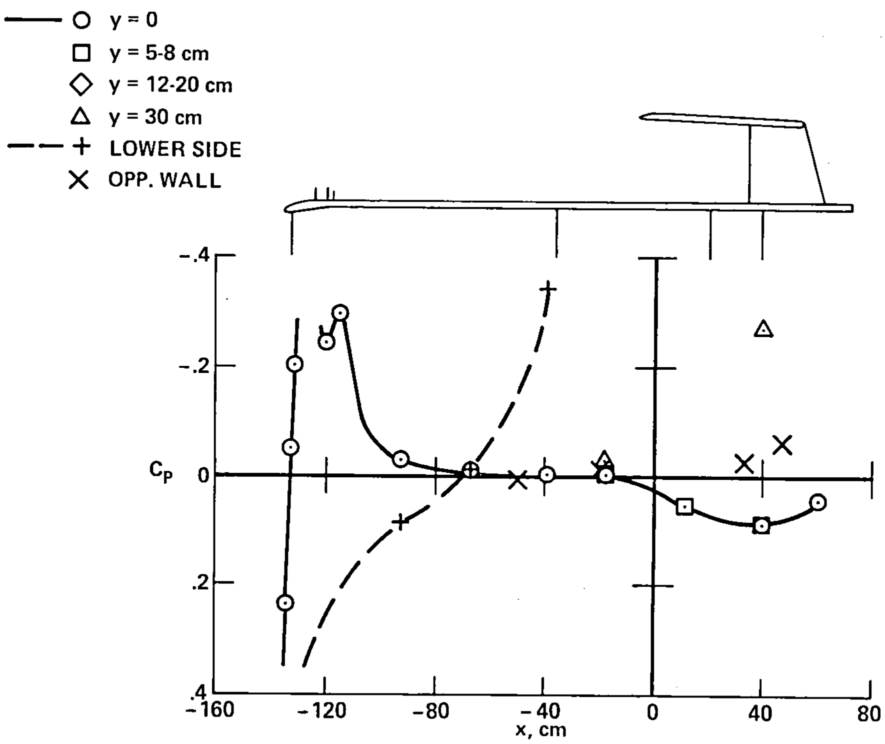

Figure 19.— Static-pressure coefficients on plate and wall; Model 1, Instrumentation 1, $M = 0.70$, $R = 9.9 \times 10^6$/m.

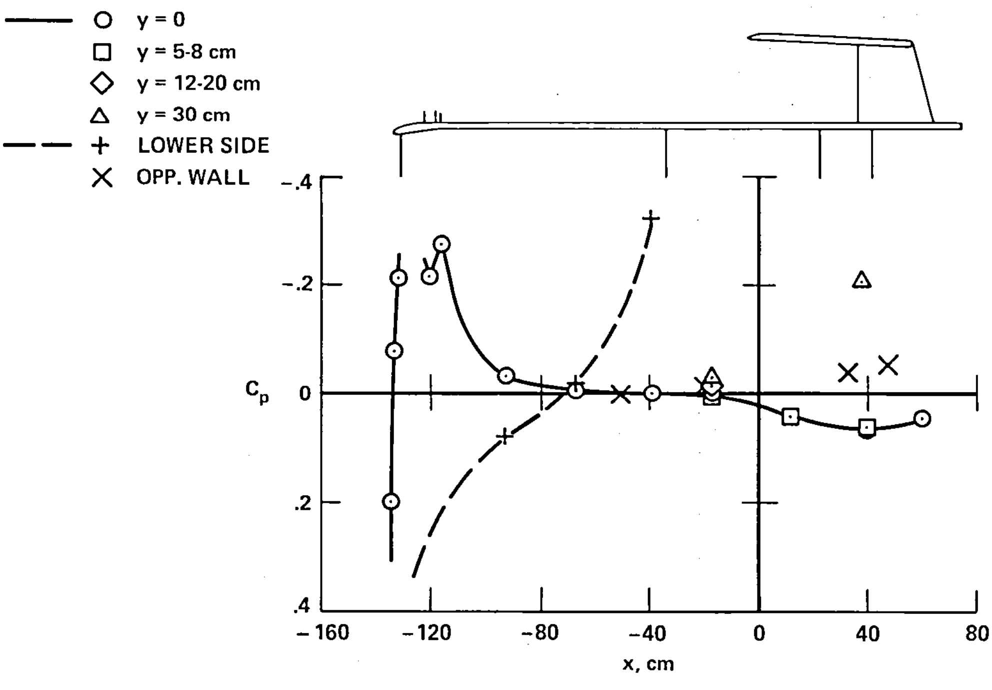

Figure 20.— Static-pressure coefficients on plate and wall; Model 1, Instrumentation 1, $M = 0.6$, $R = 9.9 \times 10^6$/m.

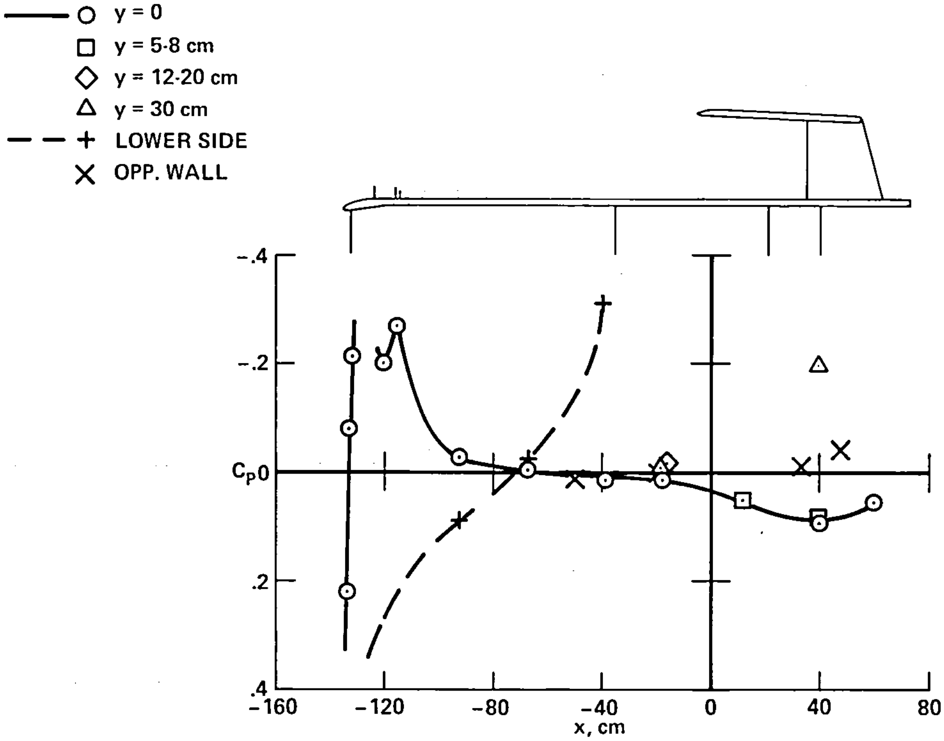

Figure 21.– Static-pressure coefficients on plate and wall; Model 1, Instrumentation 1, $M = 0.60$, R = 6.5X10^6/m.

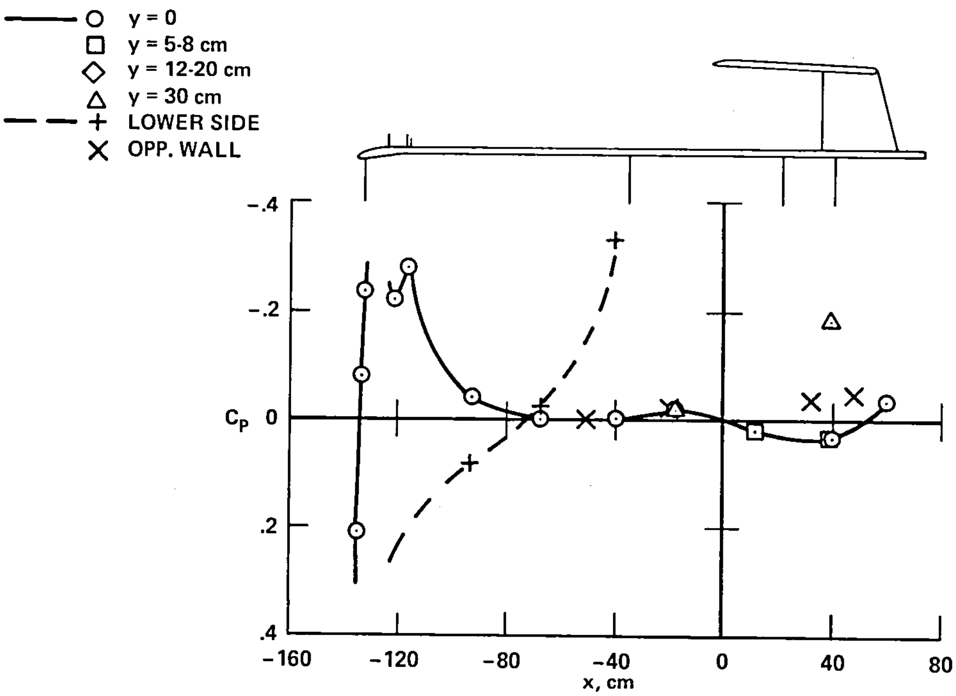

Figure 22.– Static-pressure coefficients on plate and wall; Model 1, Instrumentation 5, $M = 0.60$, $R = 9.8 \times 10^6$/m.

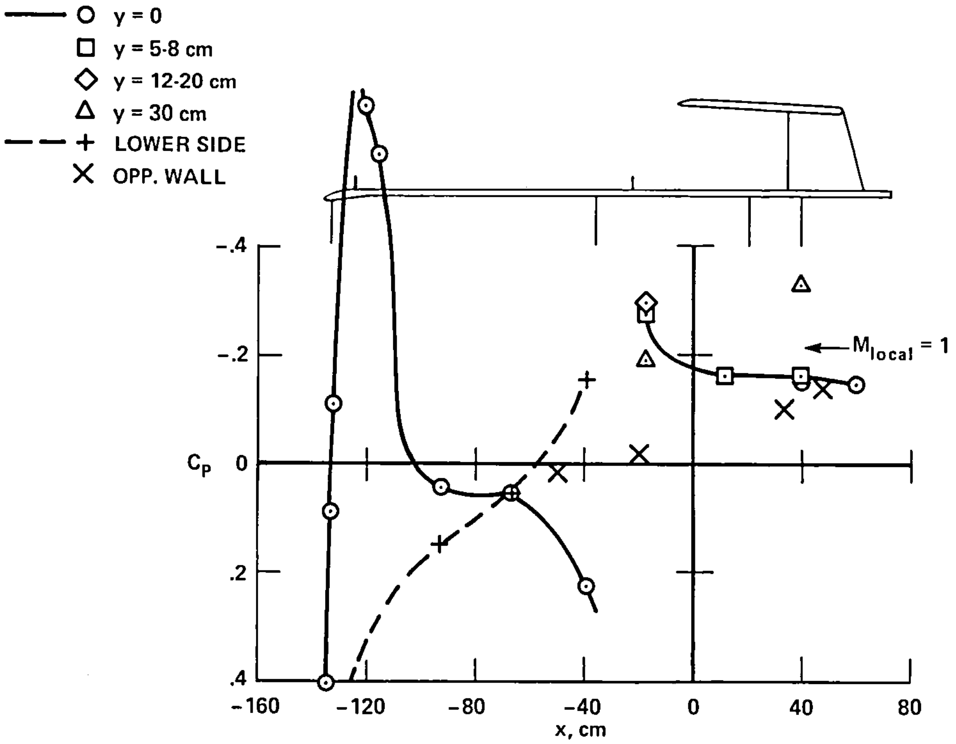

Figure 23.– Static-pressure coefficients on plate and wall; Model 2, Instrumentation 1, $M = 0.89$, $R = 9.8 \times 10^6$/m.

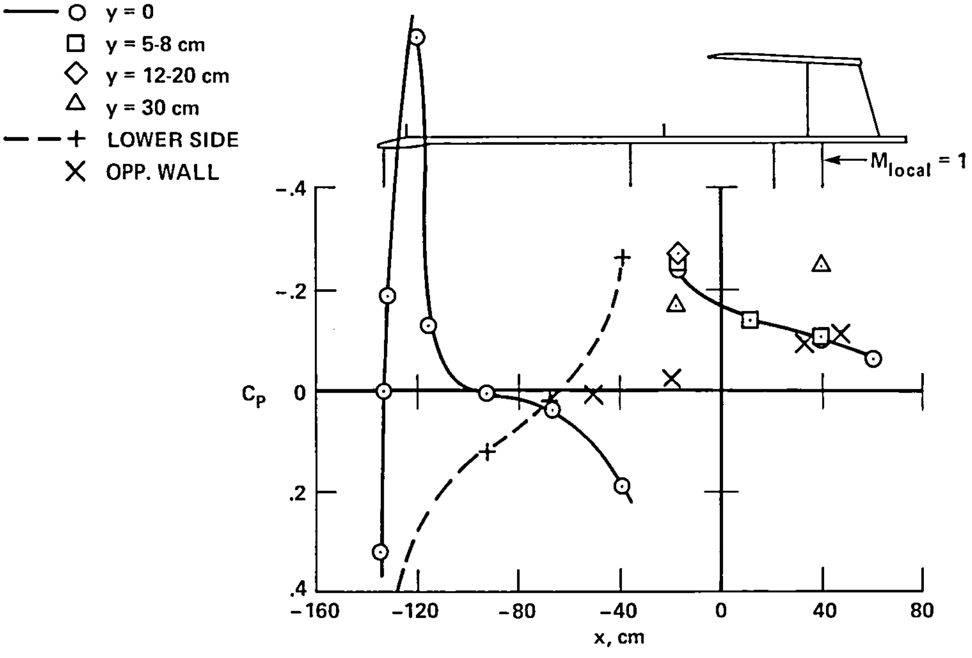

Figure 24.– Static-pressure coefficients on plate and wall; Model 2, Instrumentation 1, $M = 0.79$, $R = 9.8 \times 10^6$/m.

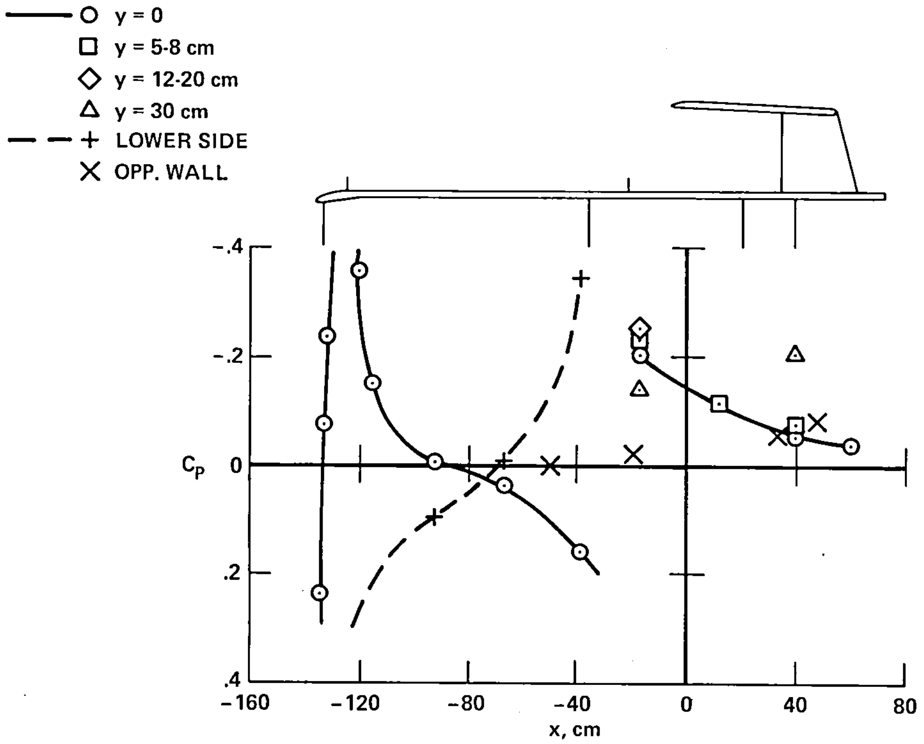

Figure 25.– Static-pressure coefficients on plate and wall; Model 2, Instrumentation 1, $M = 0.70$, $R = 9.8 \times 10^6$/m.

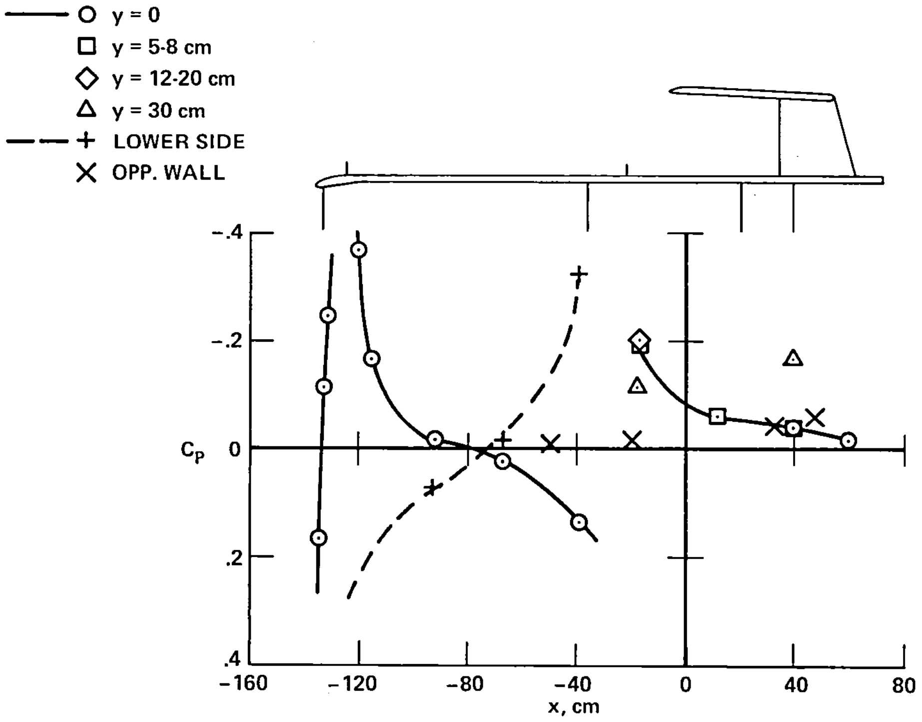

Figure 26.– Static-pressure coefficients on plate and wall; Model 2, Instrumentation 1, $M = 0.60$, $R = 9.8 \times 10^6$/m.

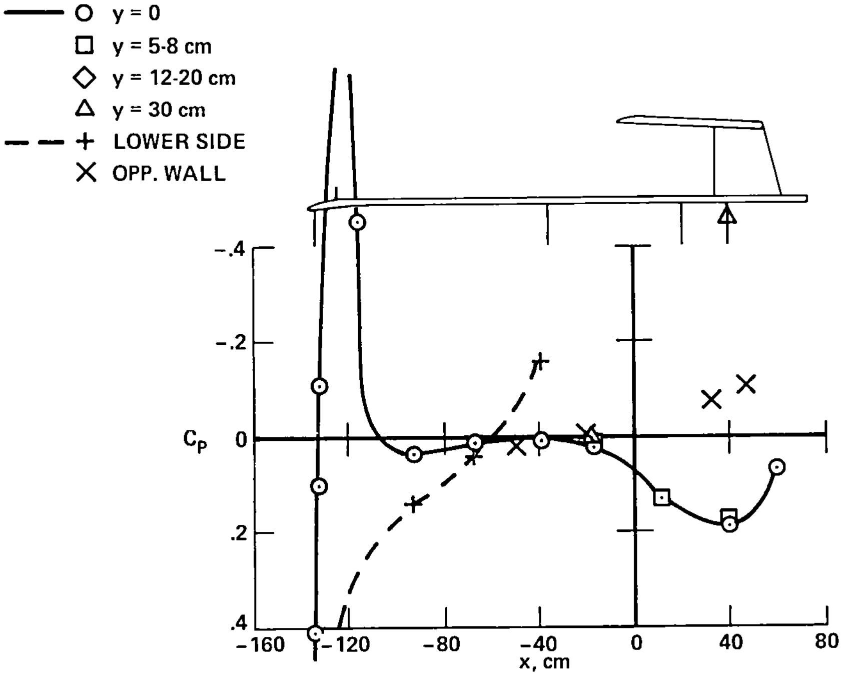

Figure 27.– Static-pressure coefficients on plate and wall; Model 3, Instrumentation 1, $M = 0.89$, $R = 9.7\times10^6$/m.

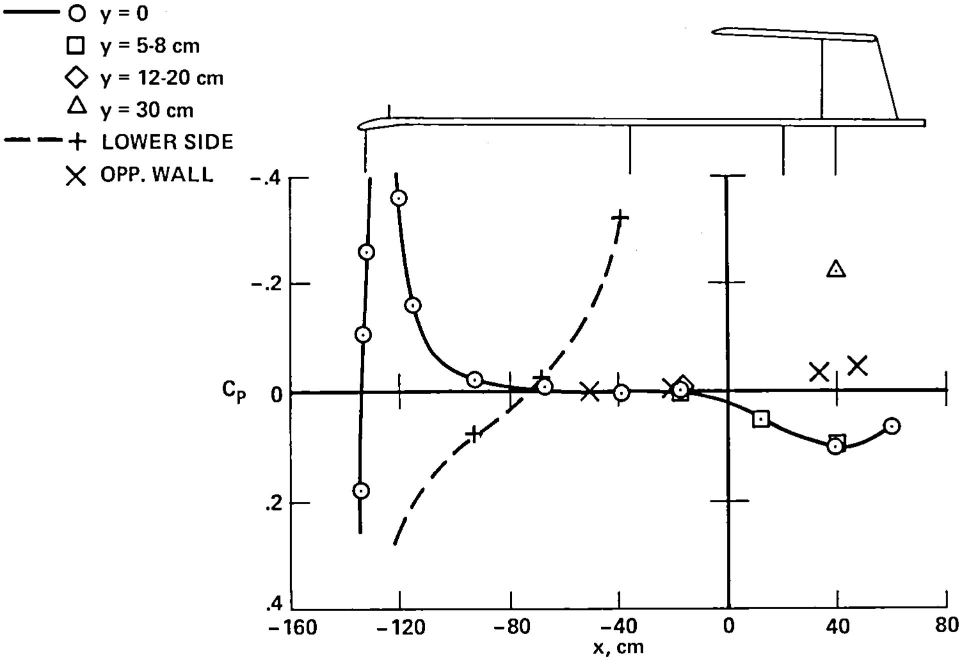

Figure 28.– Static-pressure coefficients on plate and wall; Model 3, Instrumentation 1, $M = 0.60$, $R = 9.9\times10^6$/m.

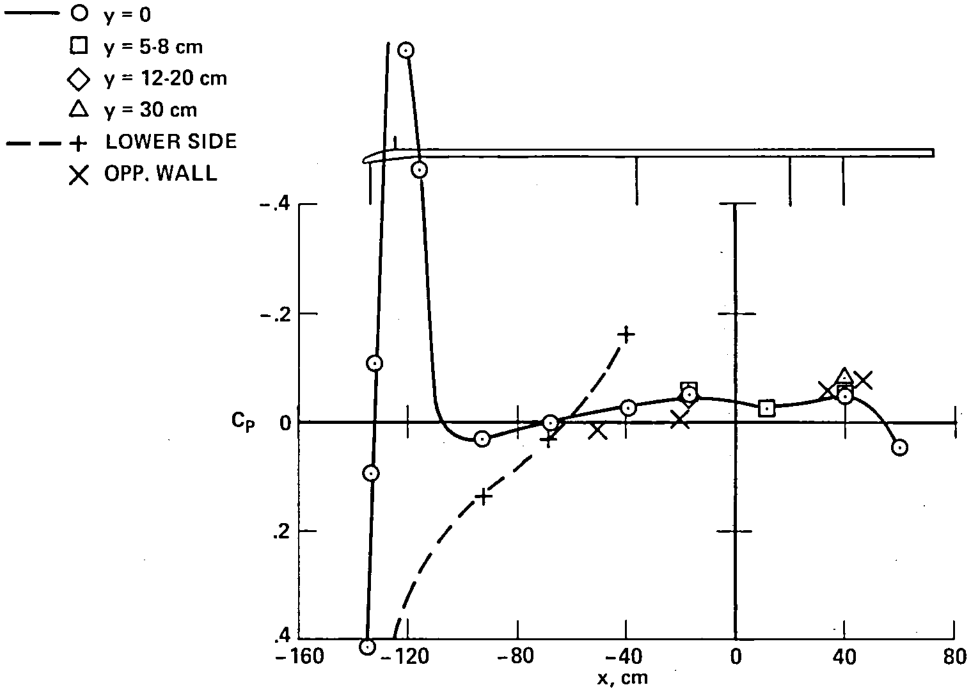

Figure 29.– Static-pressure coefficients on plate and wall; Model 4, Instrumentation 1, $M = 0.89$, $R = 9.9 \times 10^6$/m.

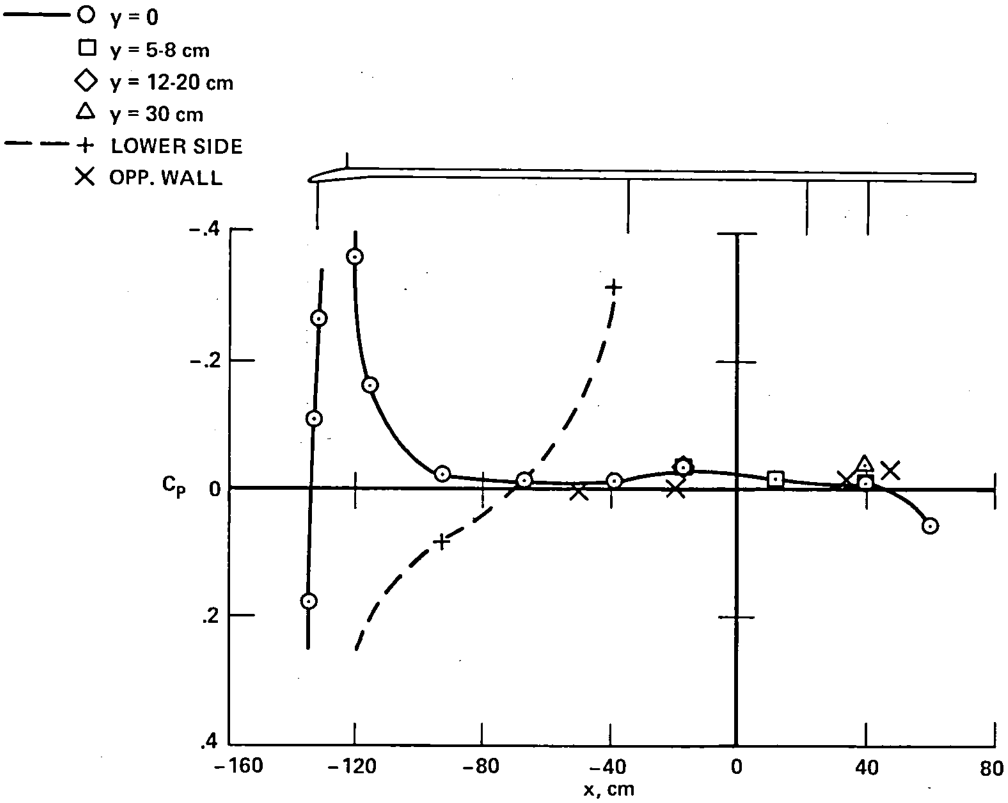

Figure 30.– Static-pressure coefficients on plate and wall; Model 4, Instrumentation 1, $M = 0.60$, $R = 6.6 \times 10^6$/m.

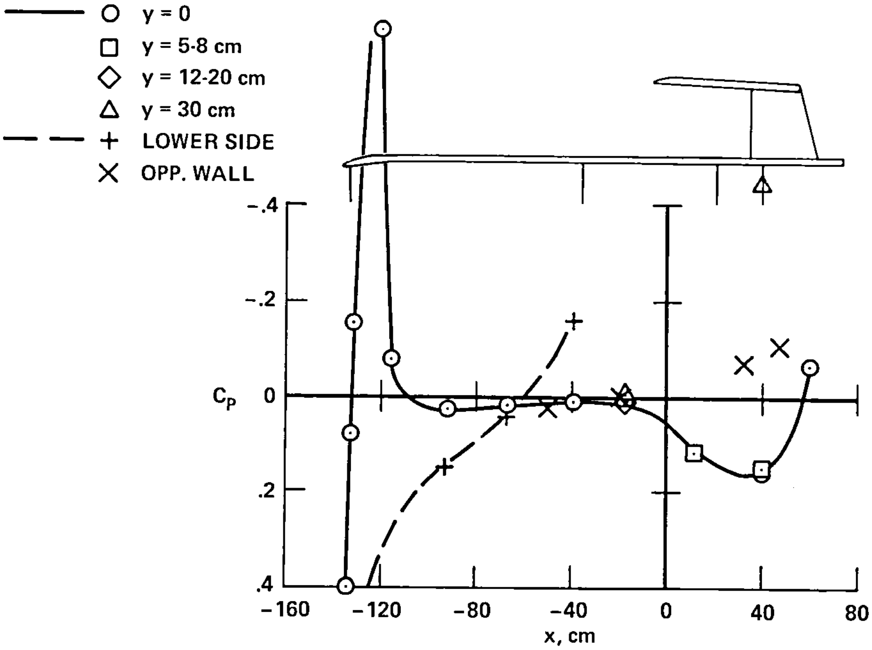

Figure 31.– Static-pressure coefficients on plate and wall; Model 19, Instrumentation 5, $M = 0.89$, $R = 9.8 \times 10^6$/m.

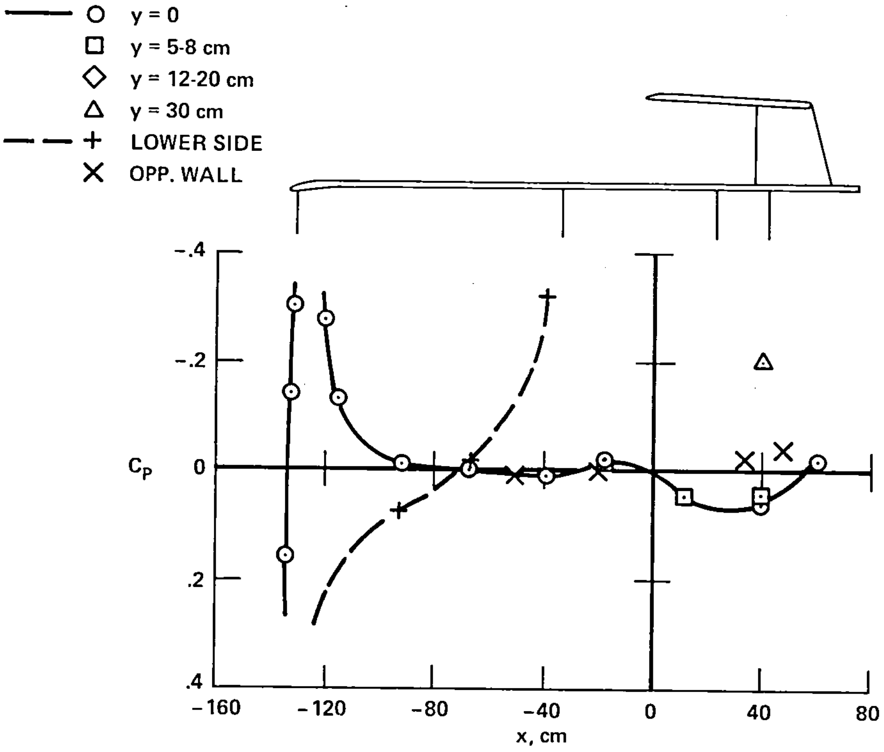

Figure 32.– Static-pressure coefficients on plate and wall; Model 19, Instrumentation 5, $M = 0.60$, $R = 9.8 \times 10^6$/m.

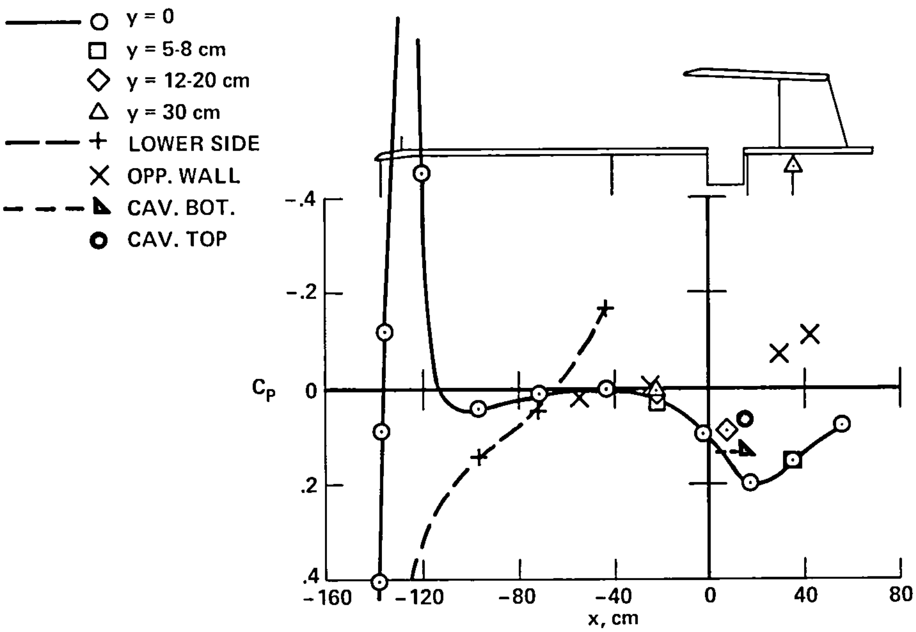

Figure 33.— Static-pressure coefficients on plate, wall, and cavity; Model 8, Instrumentation 2, $M = 0.89$, $R = 9.7 \times 10^6$/m.

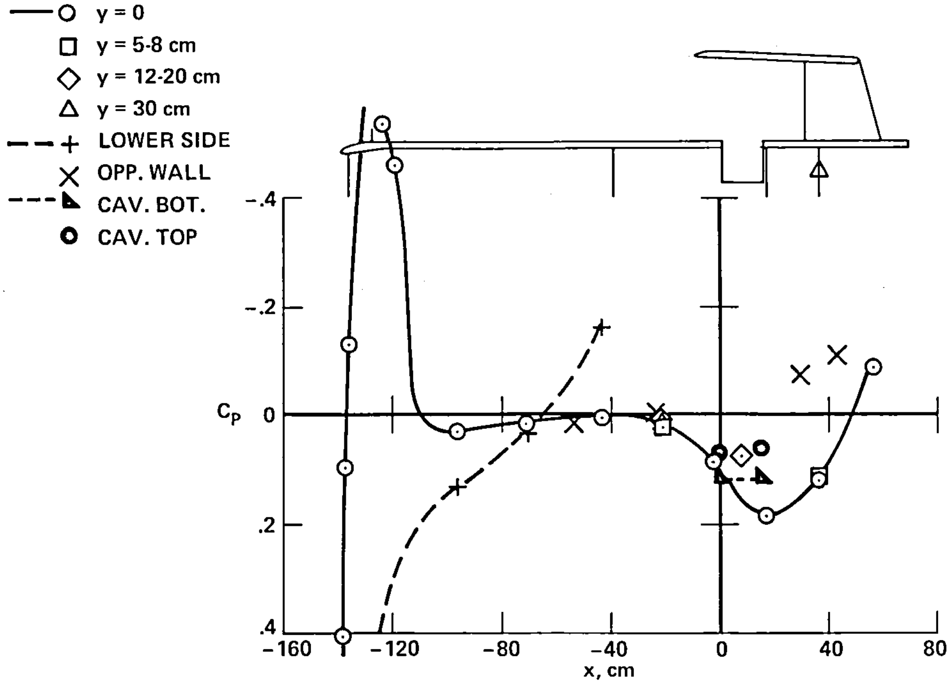

Figure 34.— Static-pressure coefficients on plate, wall, and cavity; Model 8, Instrumentation 7, $M = 0.89$, $R = 9.8 \times 10^6$/m.

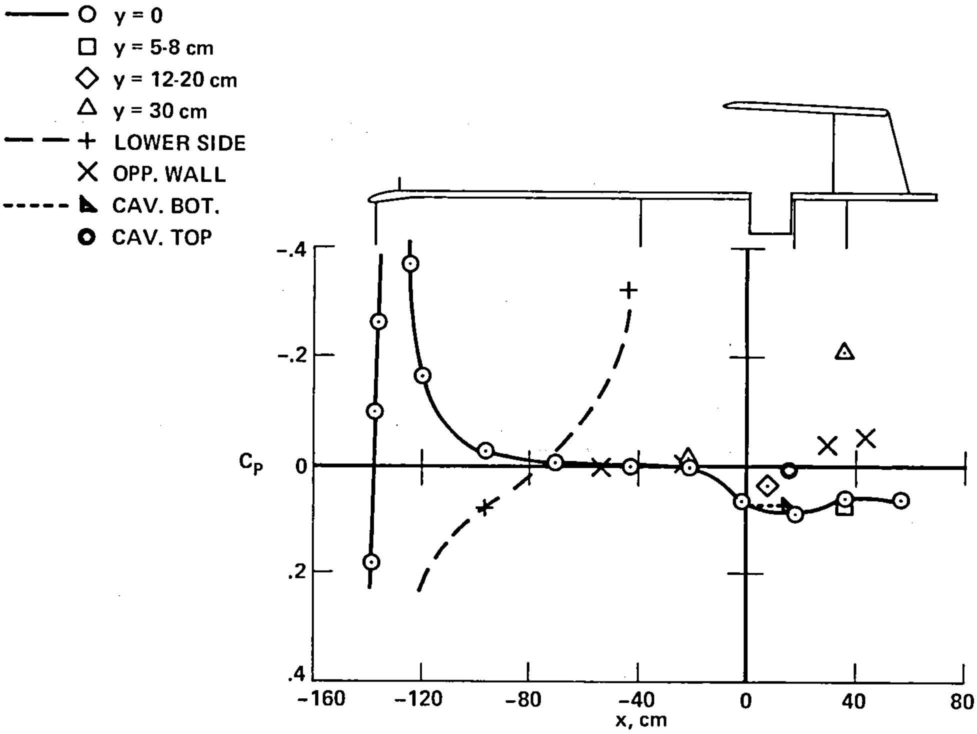

Figure 35.– Static-pressure coefficients on plate, wall, and cavity; Model 8, Instrumentation 2, $M = 0.60$, $R = 9.8 \times 10^6$/m.

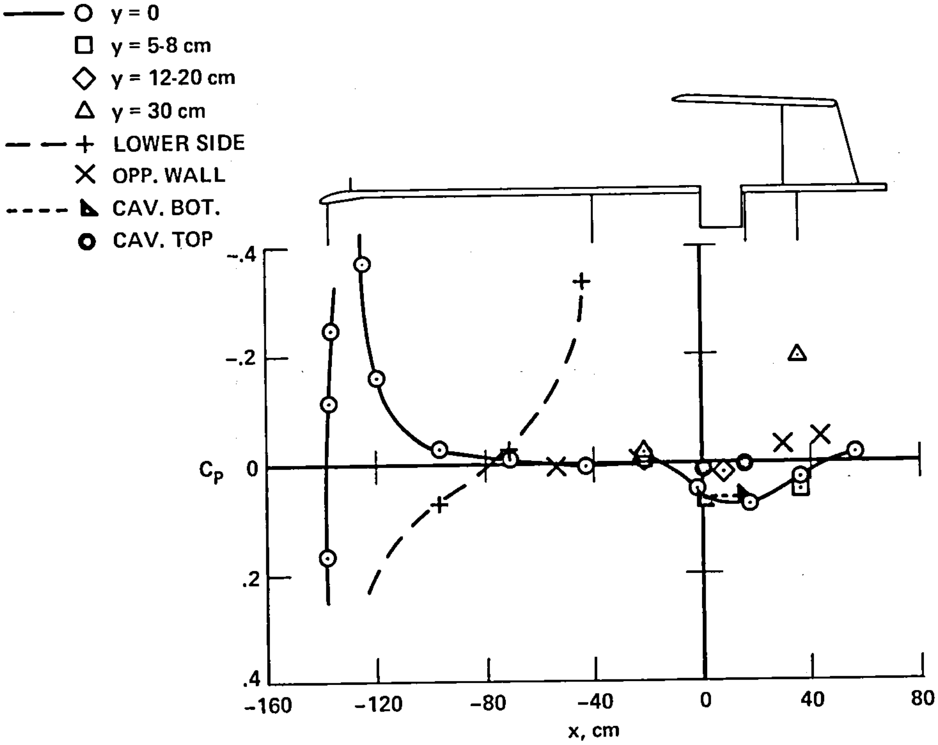

Figure 36.– Static-pressure coefficients on plate, wall, and cavity; Model 8, Instrumentation 7, $M = 0.60, R = 9.8 \times 10^6$ /m.

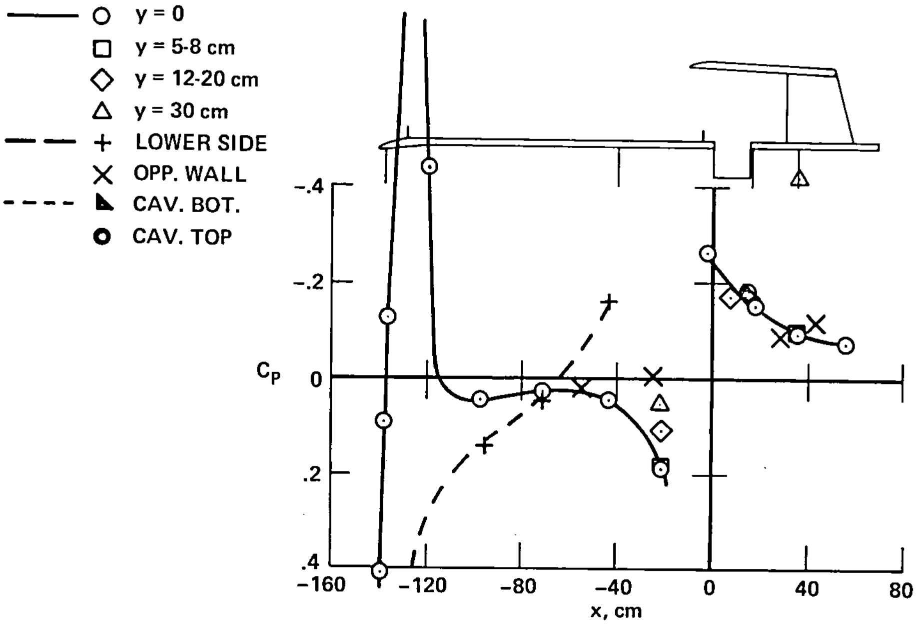

Figure 37.– Static-pressure coefficients on plate, wall, and cavity; Model 11, Instrumentation 2, $M = 0.89$, $R = 9.8 \times 10^6$/m.

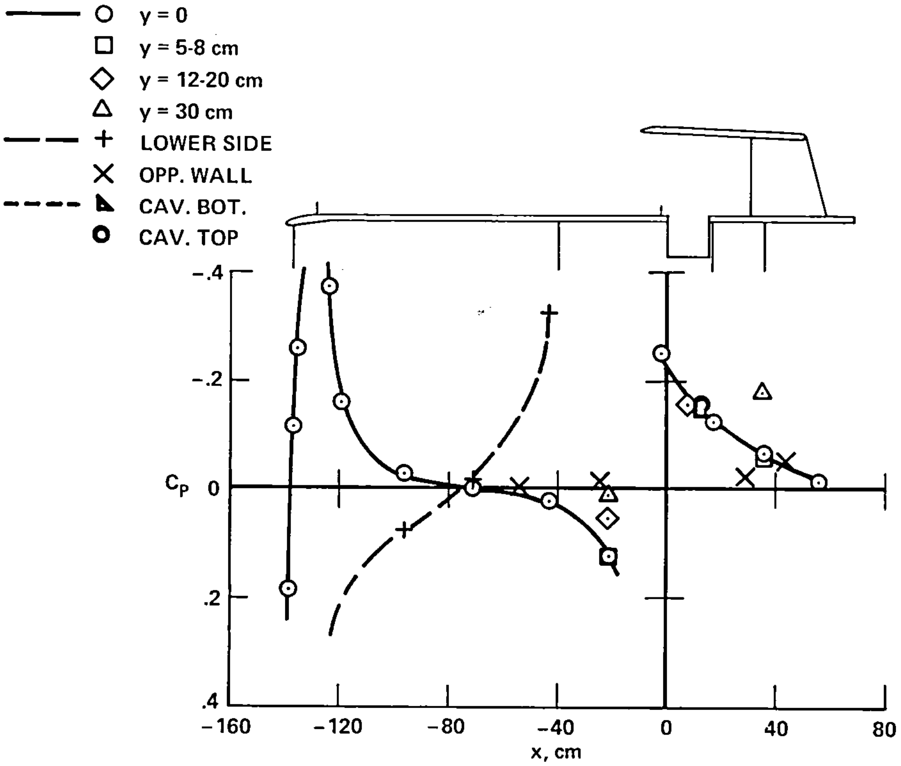

Figure 38.– Static-pressure coefficients on plate, wall, and cavity; Model 11, Instrumentation 2, $M = 0.60$, $R = 9.8 \times 10^6$/m.

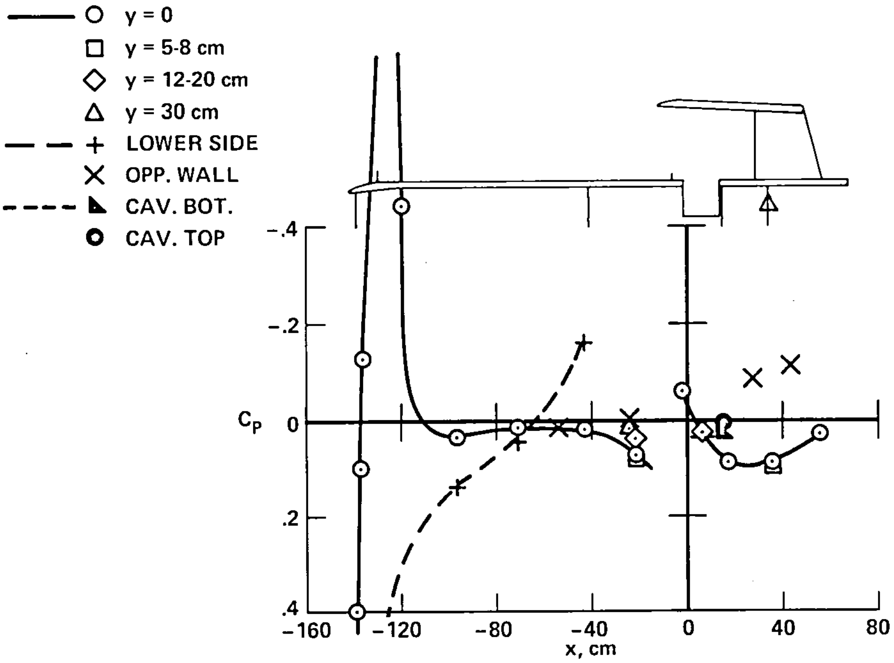

Figure 39.– Static-pressure coefficients on plate, wall, and cavity; Model 13, Instrumentation 2, $M = 0.89$, $R = 9.8 \times 10^6$/m.

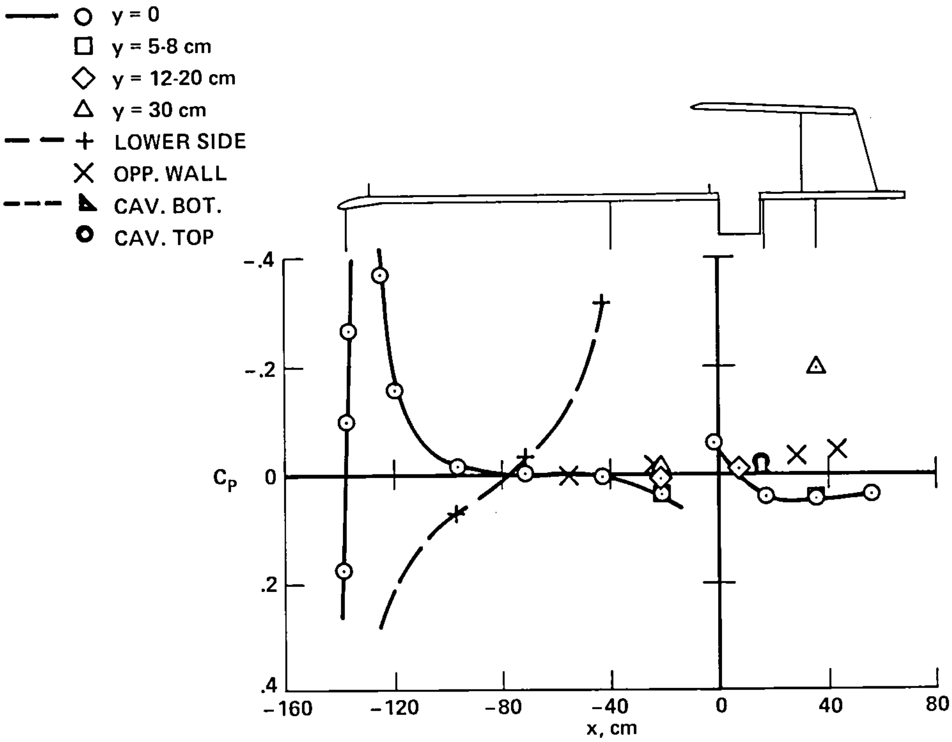

Figure 40.– Static-pressure coefficients on plate, wall, and cavity; Model 13, Instrumentation 2, $M = 0.60$, $R = 9.9 \times 10^6$/m.

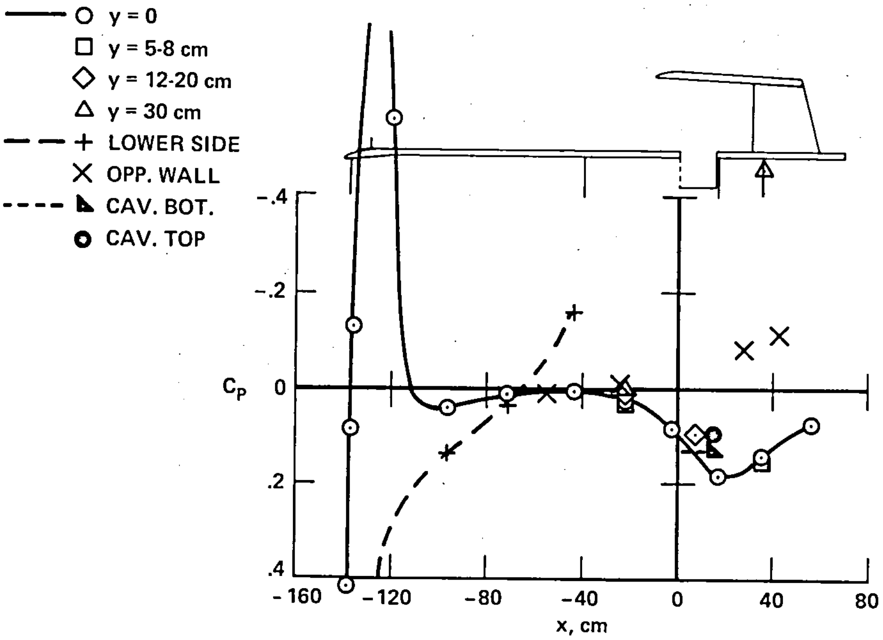

Figure 41.– Static-pressure coefficients on plate, wall, and cavity; Model 14, $\dot{m} = 0$, Instrumentation 2, $M = 0.89$, $R = 9.8 \times 10^6$/m.

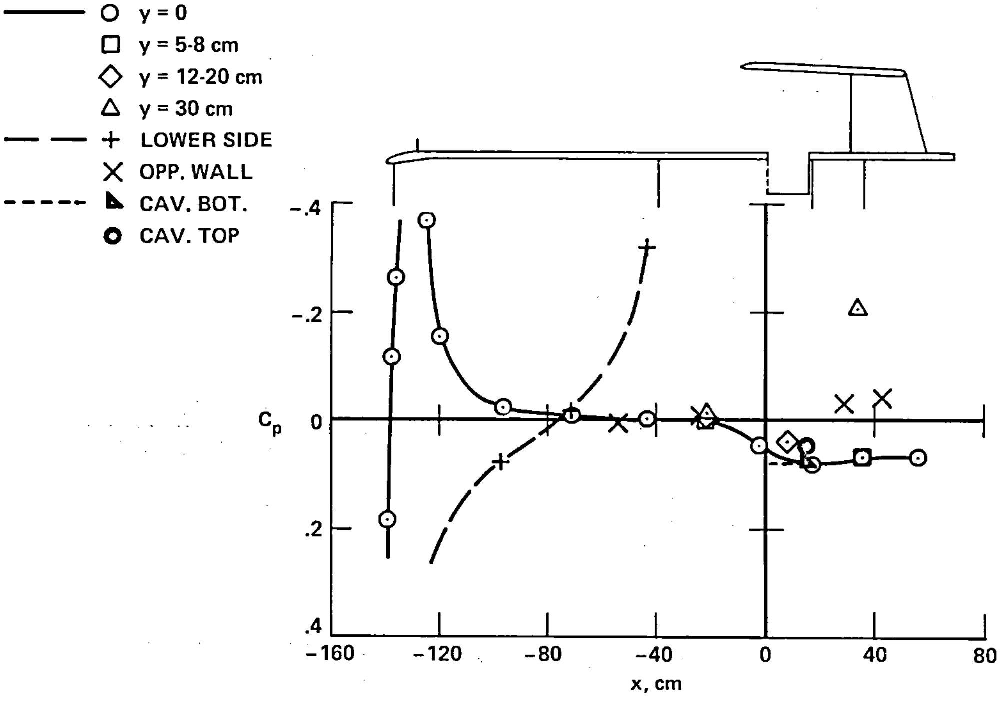

Figure 42.– Static-pressure coefficients on plate, wall, and cavity; Model 14, $\dot{m} = 0$, Instrumentation 2, $M = 0.60$, $R = 9.8 \times 10^6$/m.

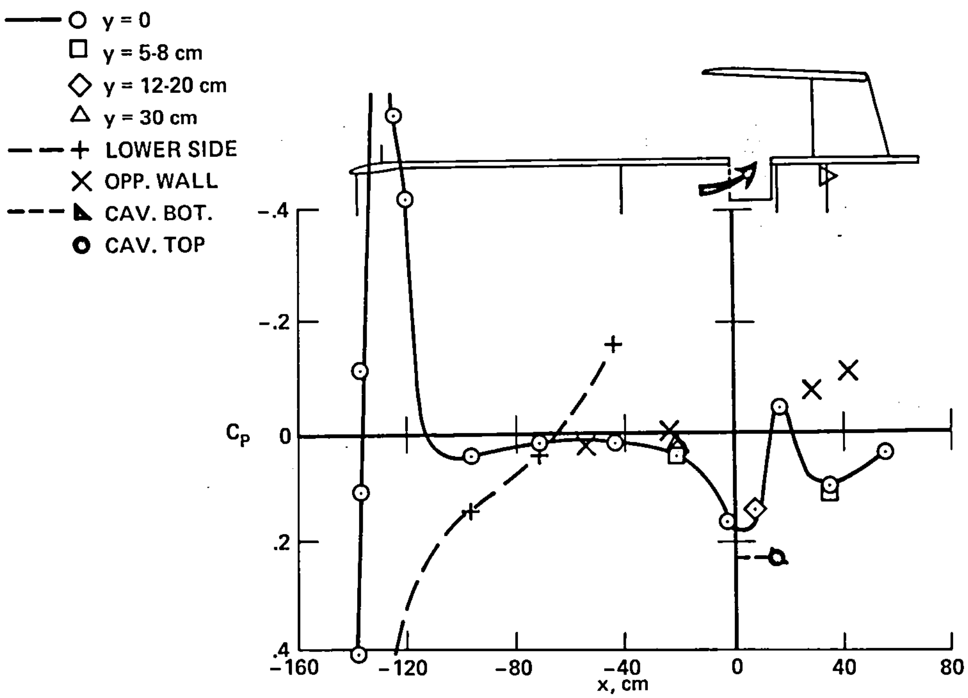

Figure 43.– Static-pressure coefficients on plate, wall, and cavity; Model 14, $\dot{m}$ = 0.23 kg/sec, Instrumentation 2, M = 0.89, R = 9.8X10^6/m.

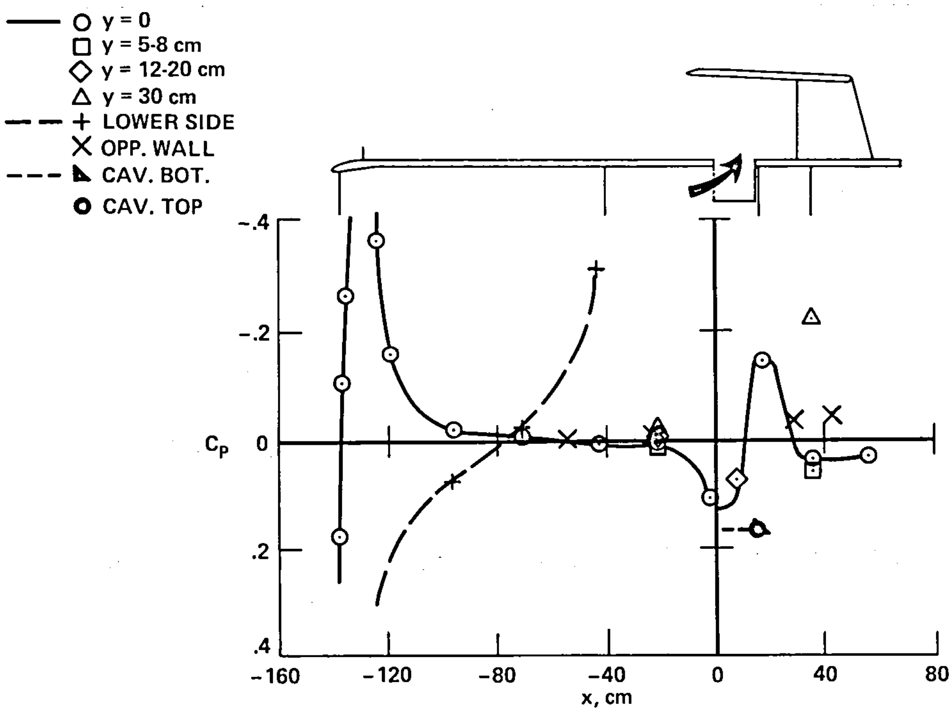

Figure 44.– Static-pressure coefficients on plate, wall, and cavity; Model 14, $\dot{m}$ = 0.24 kg/sec, Instrumentation 2, M = 0.60, R = 9.8X10^6/m.

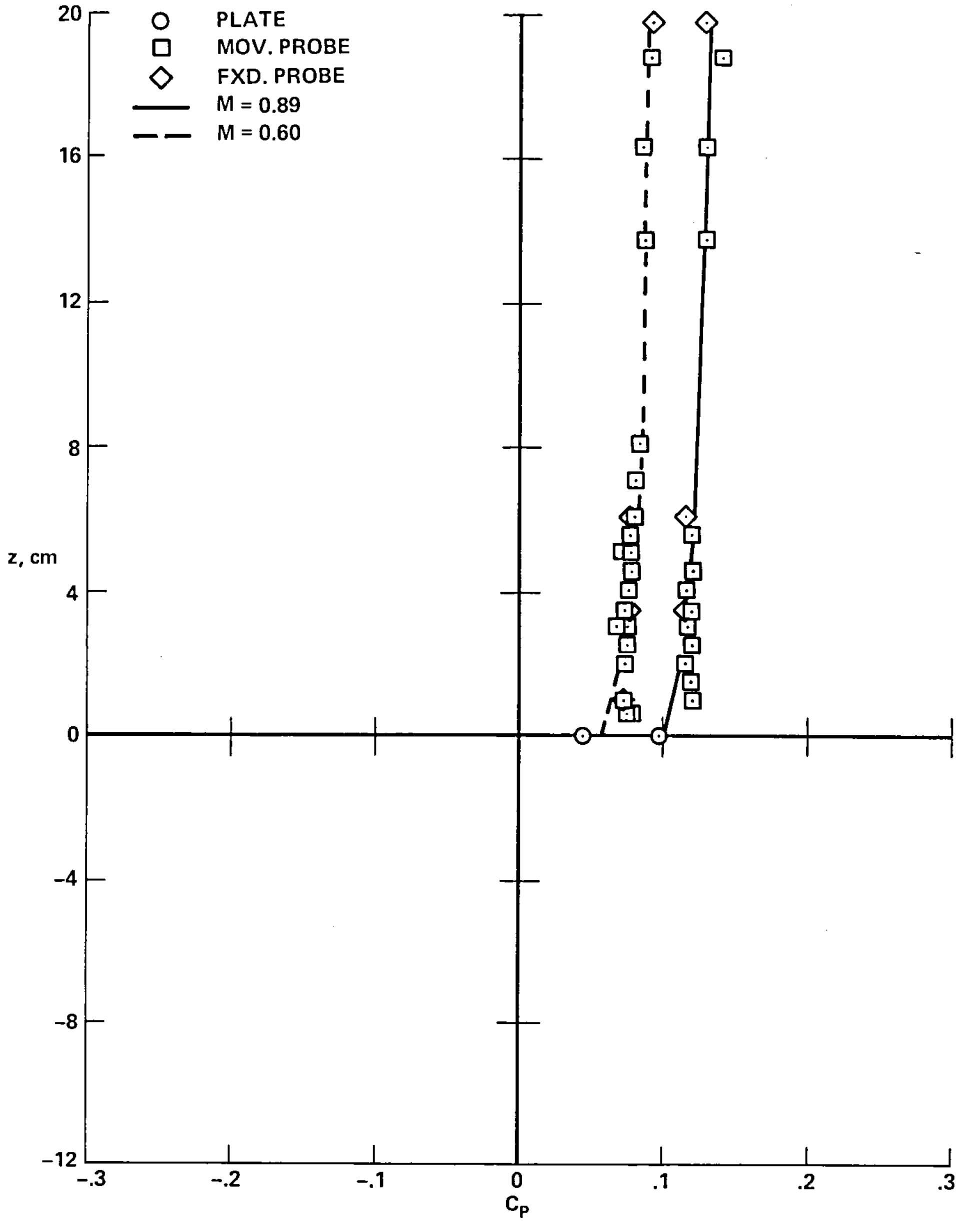

Figure 45.– Static-pressure coefficients in the boundary layer; Model 1, R = 9.8X10^6/m, x = 11.4 cm, y = -4.0 to - 1.0 cm.

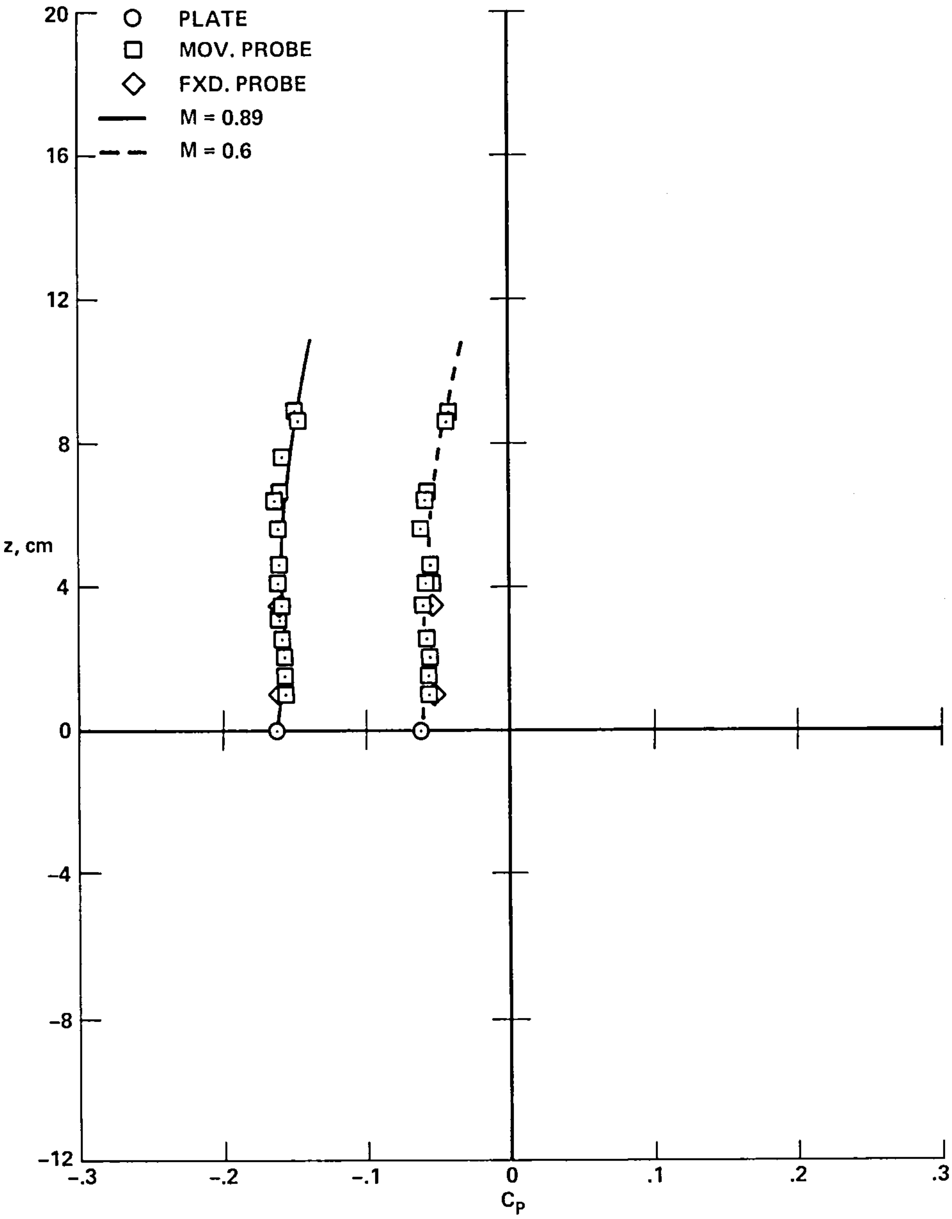

Figure 46.– Static-pressure coefficients in the boundary layer; Model 2, R = 9.8X10^6/m, x = 13.2 cm, y = – 1.0 cm.

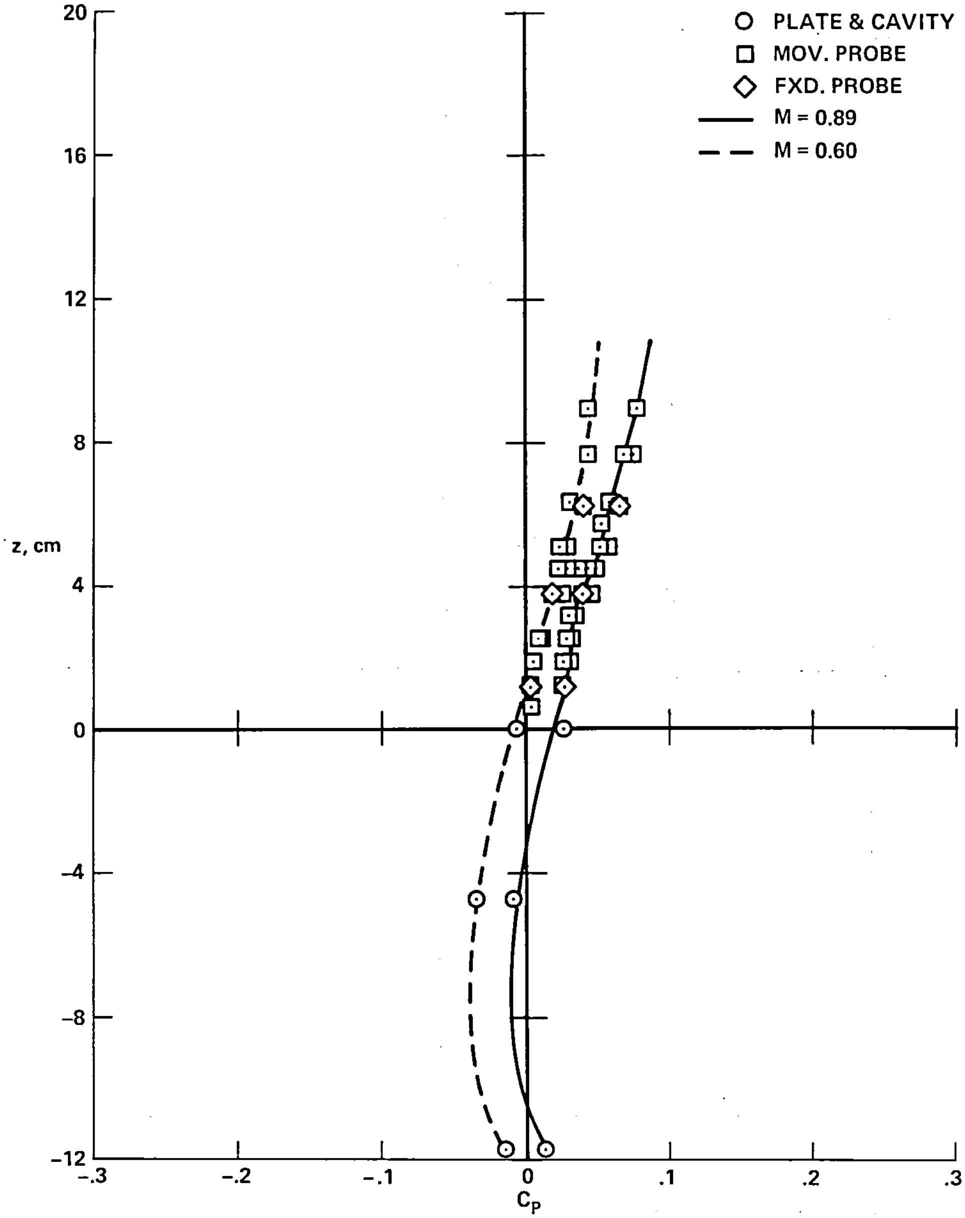

Figure 47.– Static-pressure coefficients in the shear layer; Model 13, $R = 9.8 \times 10^6$/m, $x = 9.2$ cm, $y = -0.7$ cm.

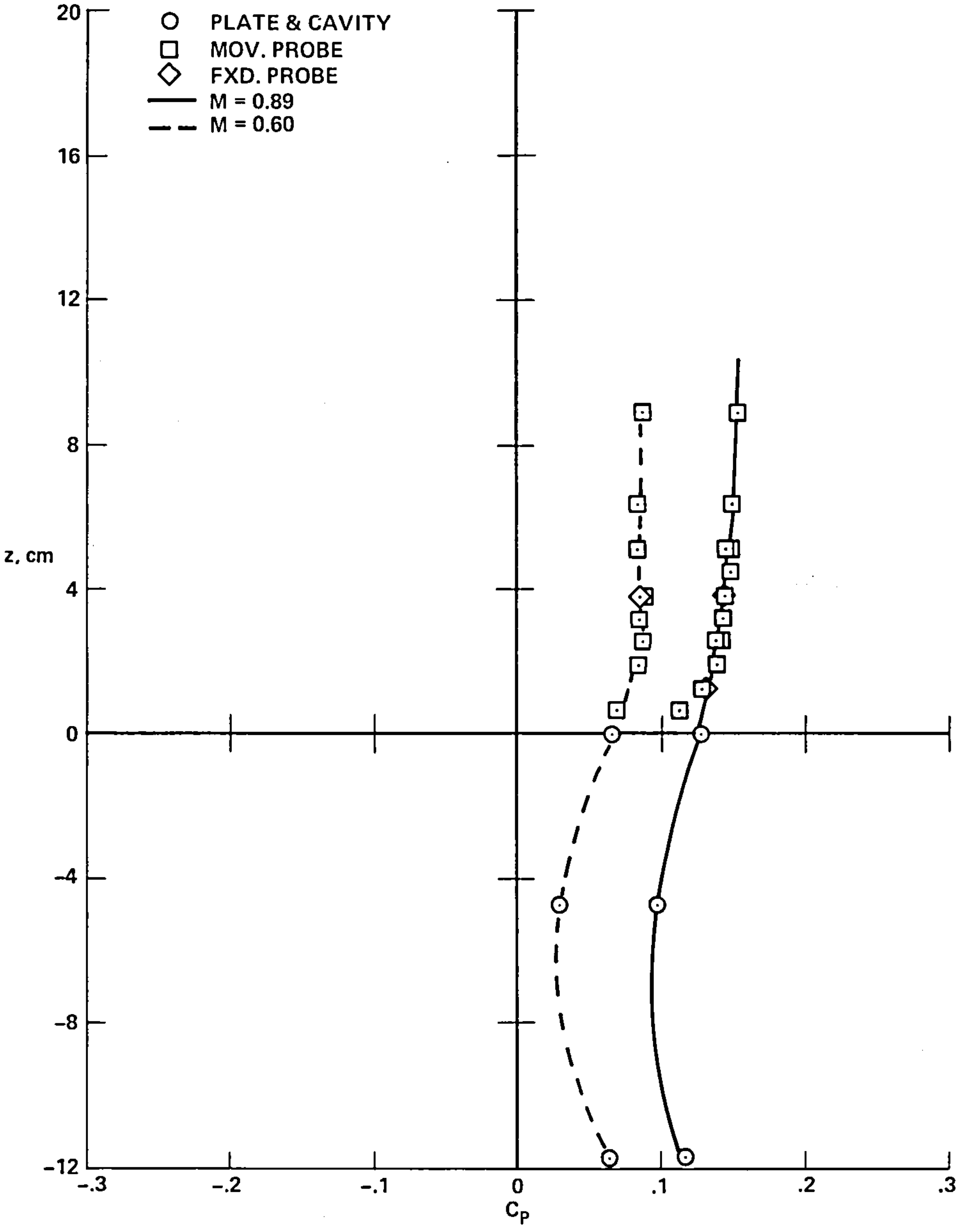

Figure 48.– Static-pressure coefficients in the shear layer; Model 14, $R = 9.8 \times 10^6$/m, $x = 9.2$ cm, $y = -0.7$ cm.

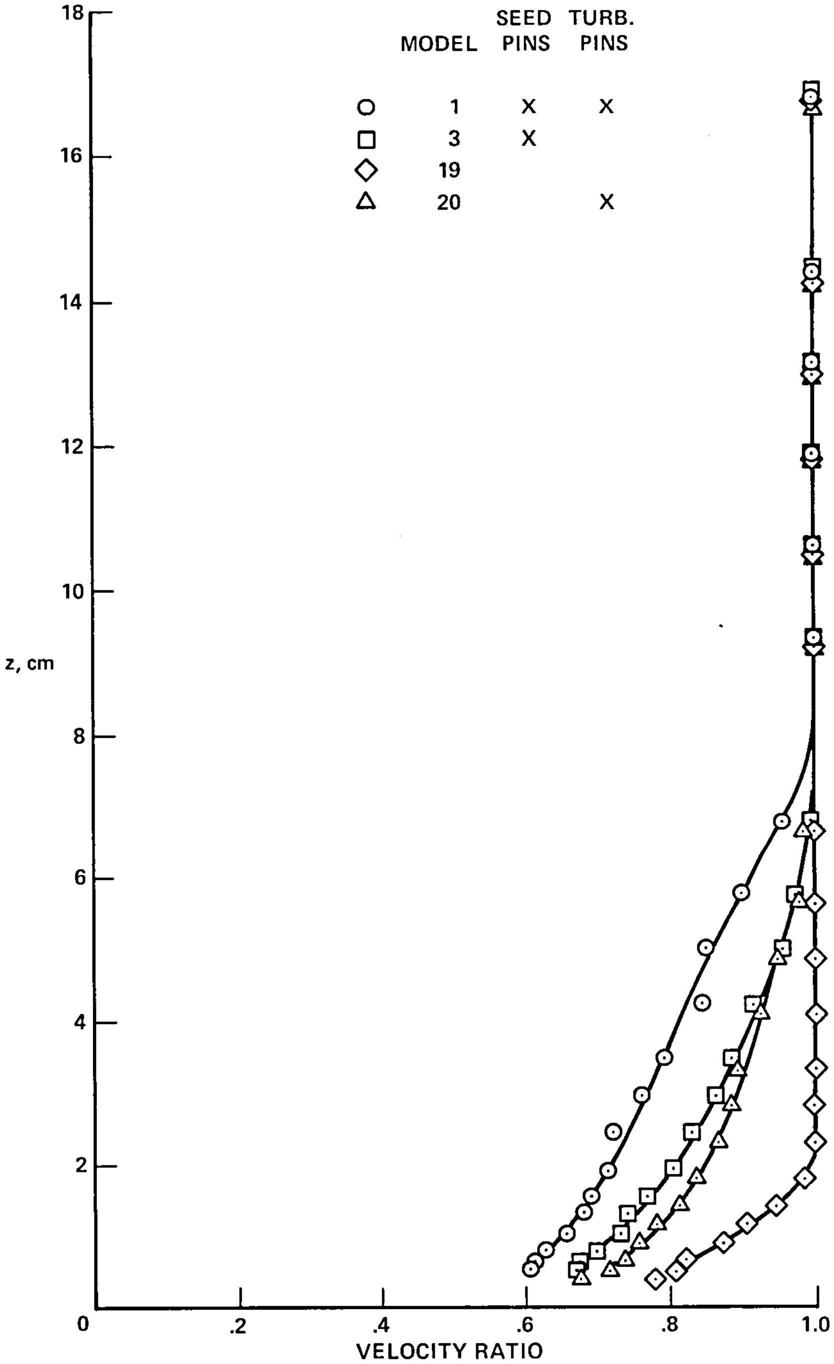

Figure 49.– Velocity profiles with and without pins; $M = 0.60$, $R = 9.8 \times 10^6$/m, $x = 21.6$ cm, $y = 0$.

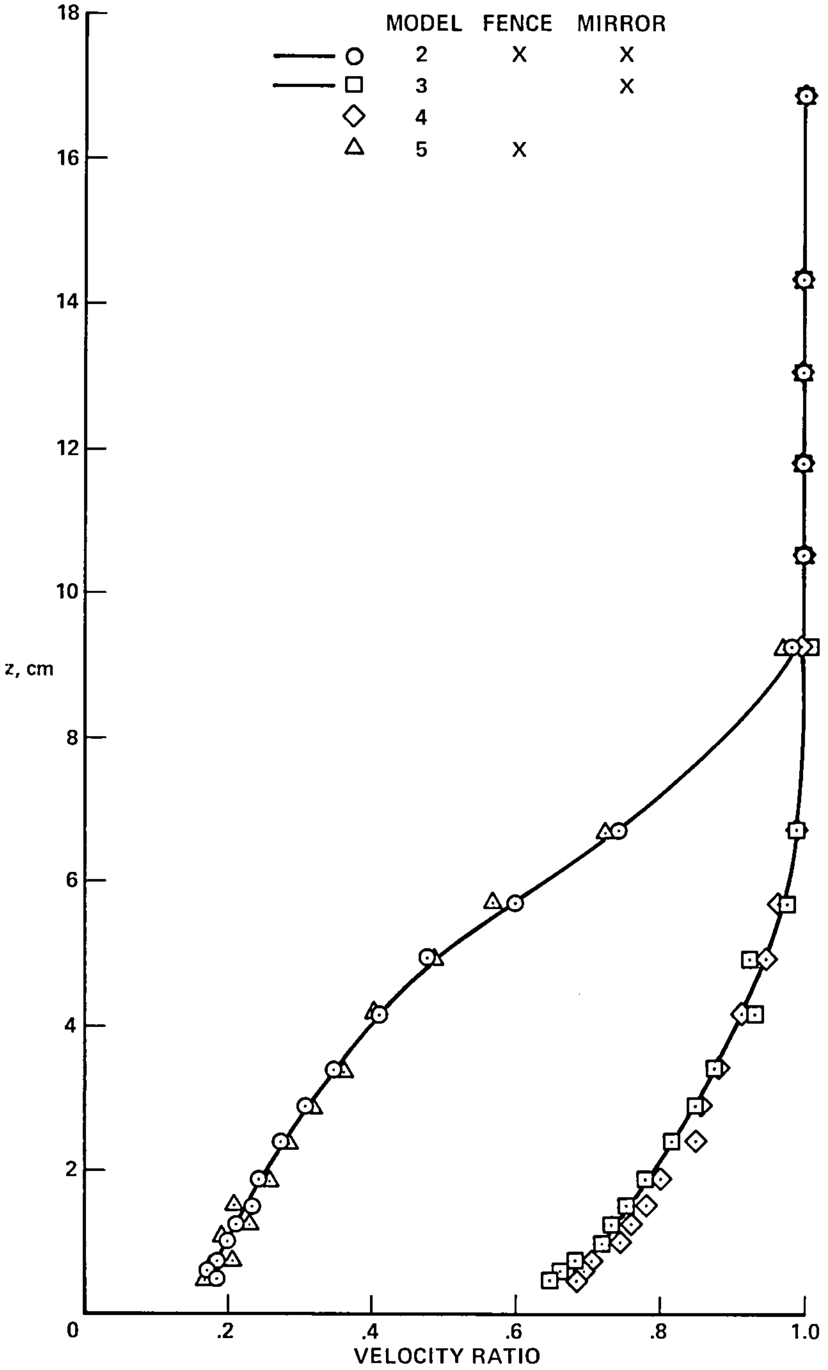

Figure 50.— Velocity profiles with and without fence and mirror; $M = 0.60$, $R = 6.6 \times 10^6$/m, $x = 11.4$ cm, $y = 0$.

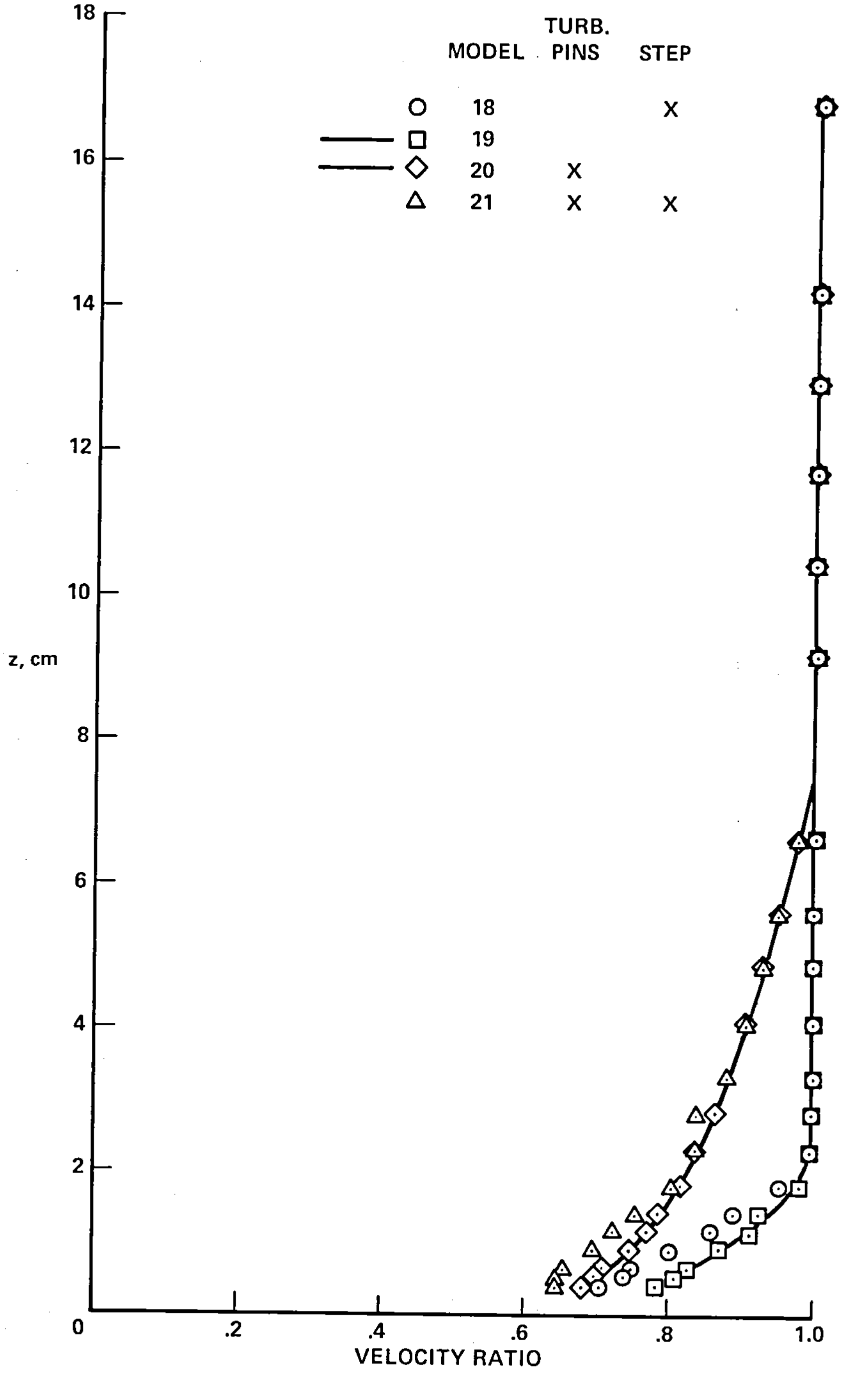

Figure 51.– Velocity profiles without seeding pins; $M = 0.70$, $R = 9.8 \times 10^6$/m, $x = 21.6$ cm, $y = 0$.

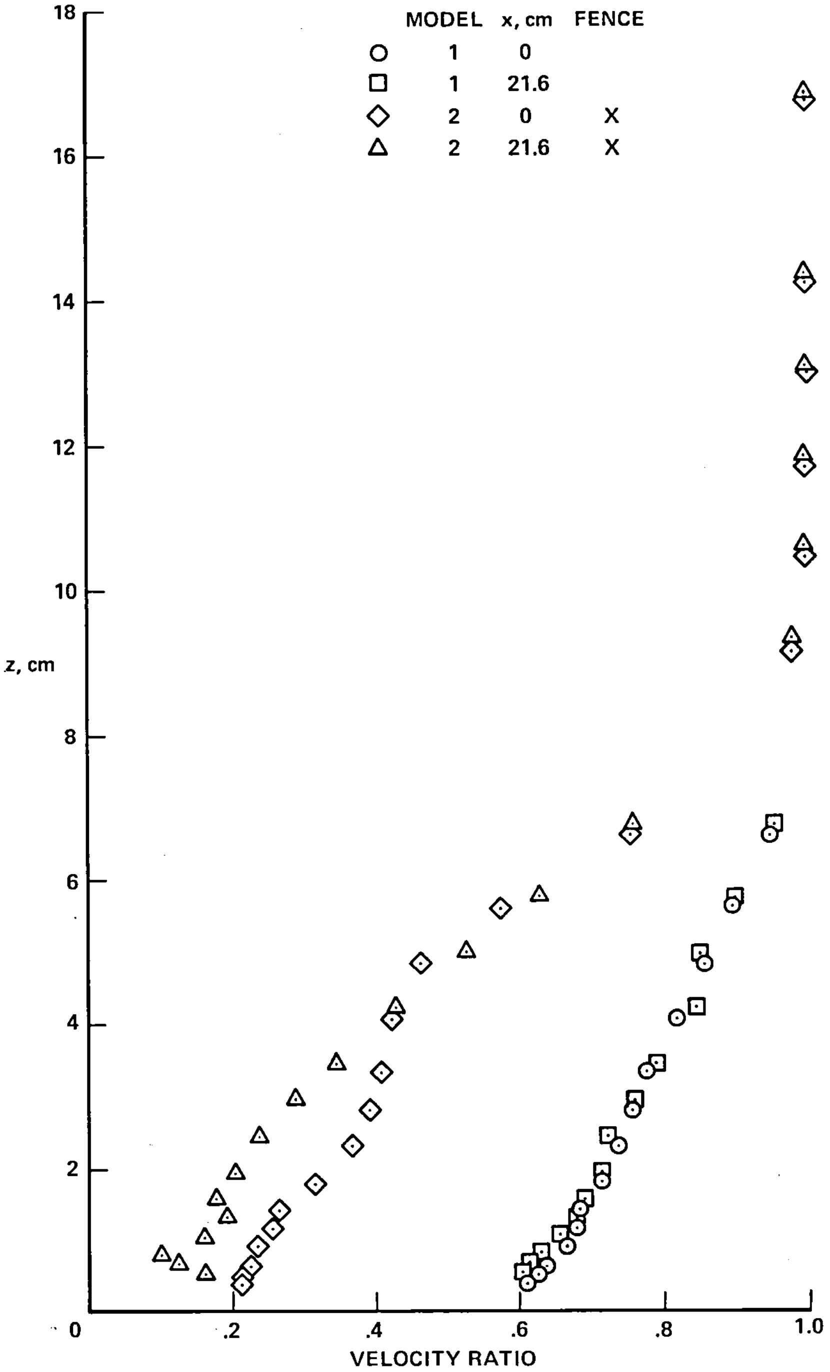

Figure 52.– Velocity profiles upstream and downstream of window; $\dot{M} = 0.60$, $R = 9.8\times10^6$/m, $y = 0$.

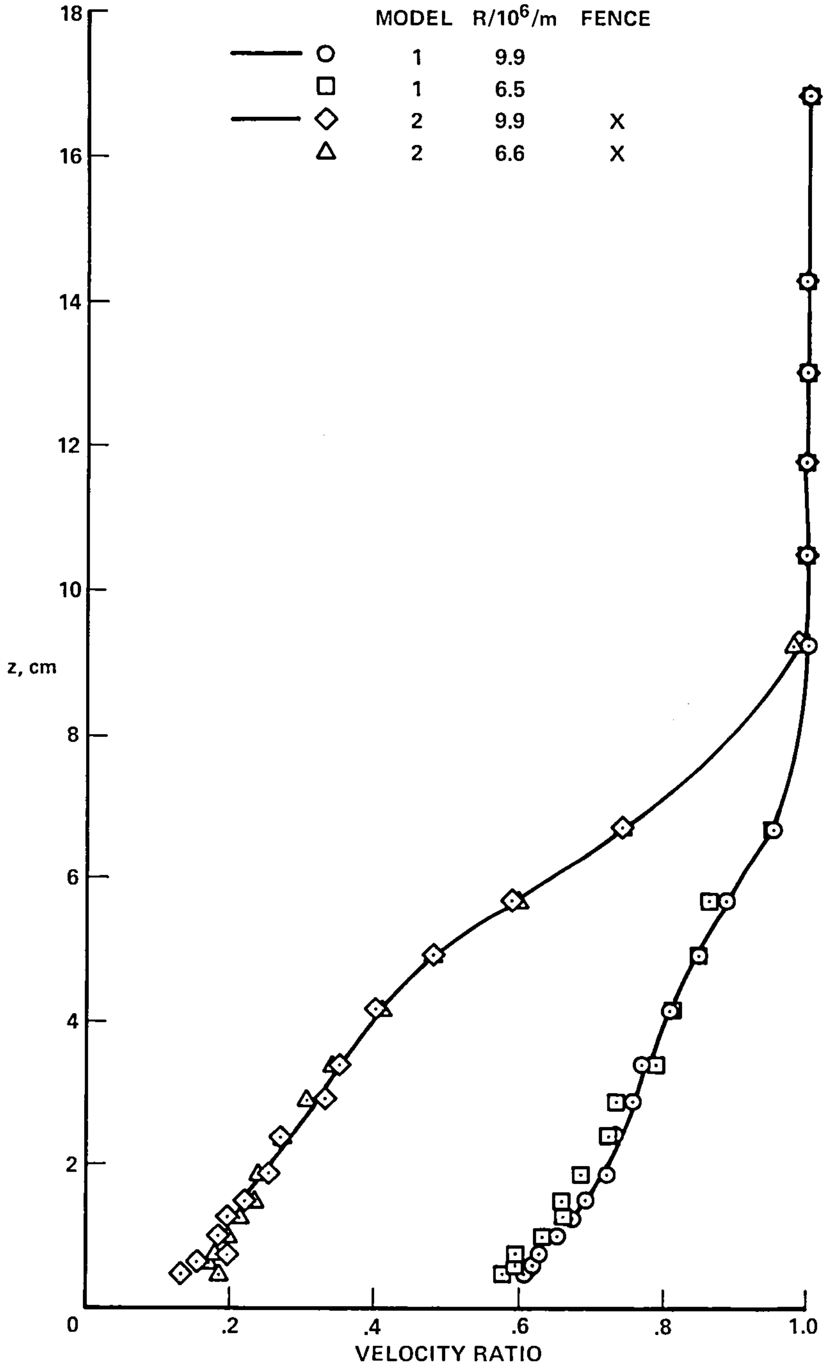

Figure 53.– Velocity profiles at two Reynolds numbers; $M = 0.60$, $x = 11.4$ cm, $y = 0$.

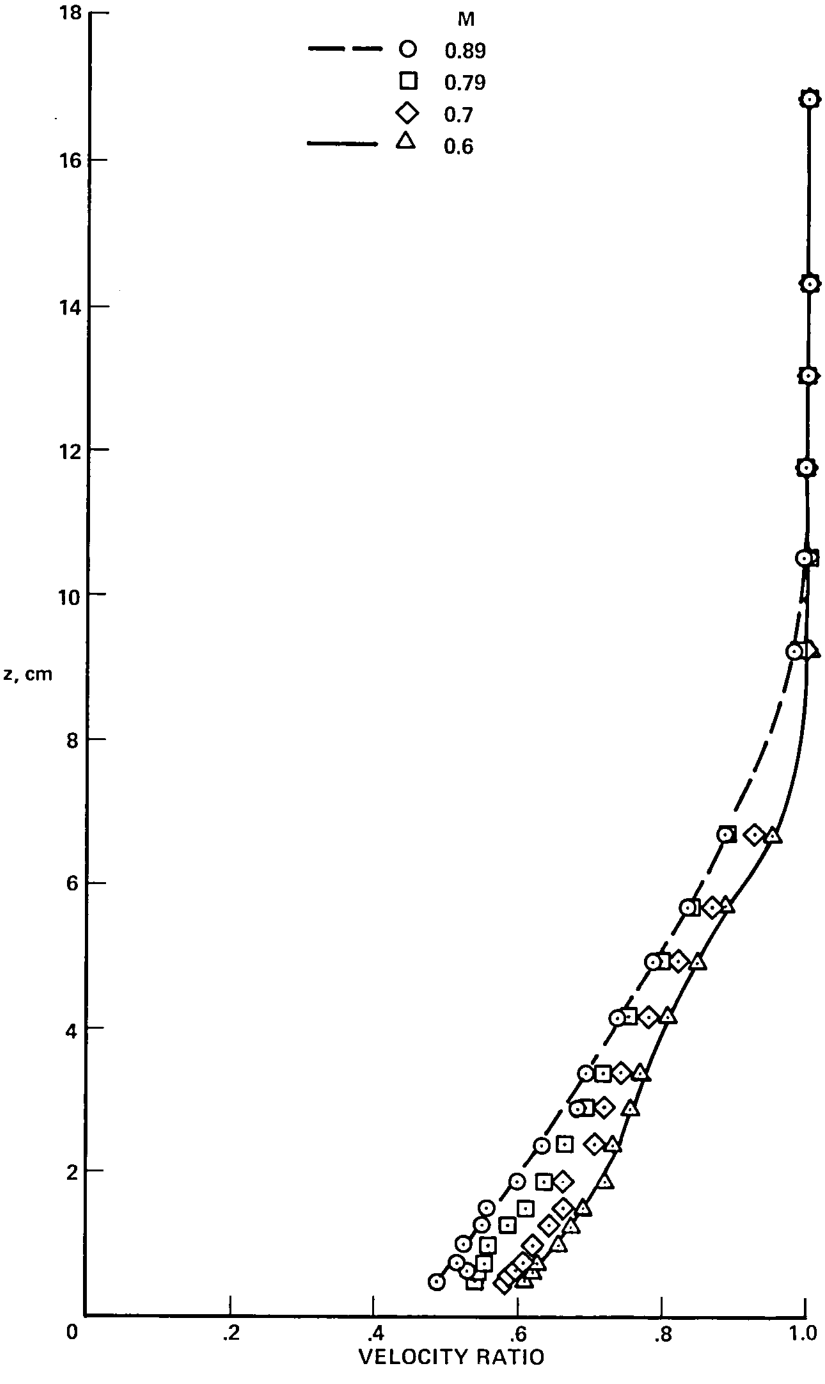

Figure 54.– Velocity profiles at various Mach numbers; Model 1, $R = 9.8$ to 12.1×10^6/m, $x = 11.4$ cm, $y = 0$.

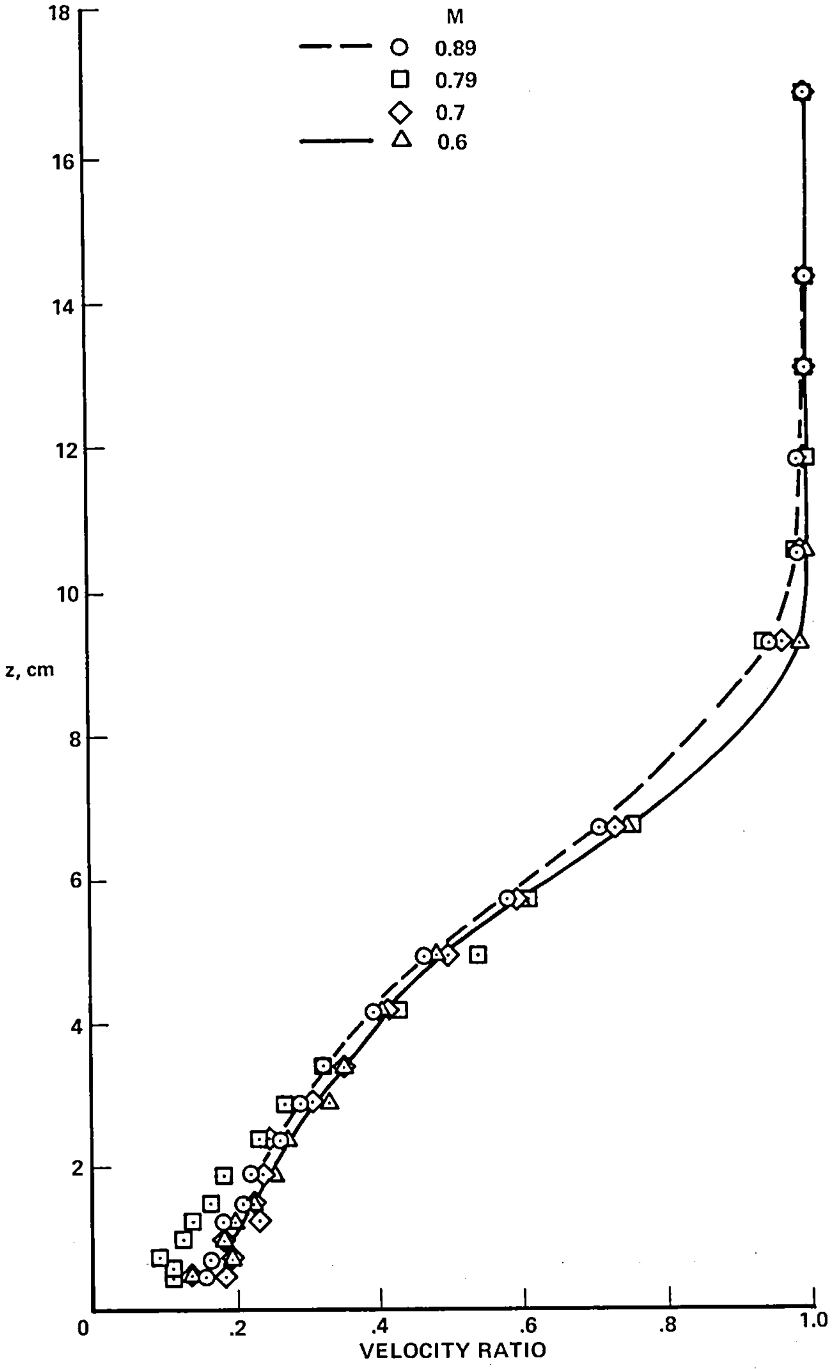

Figure 55.– Velocity profiles at various Mach numbers; Model 2, $R = 9.8 \times 10^6$/m, $x = 11.4$ cm, $y = 0$.

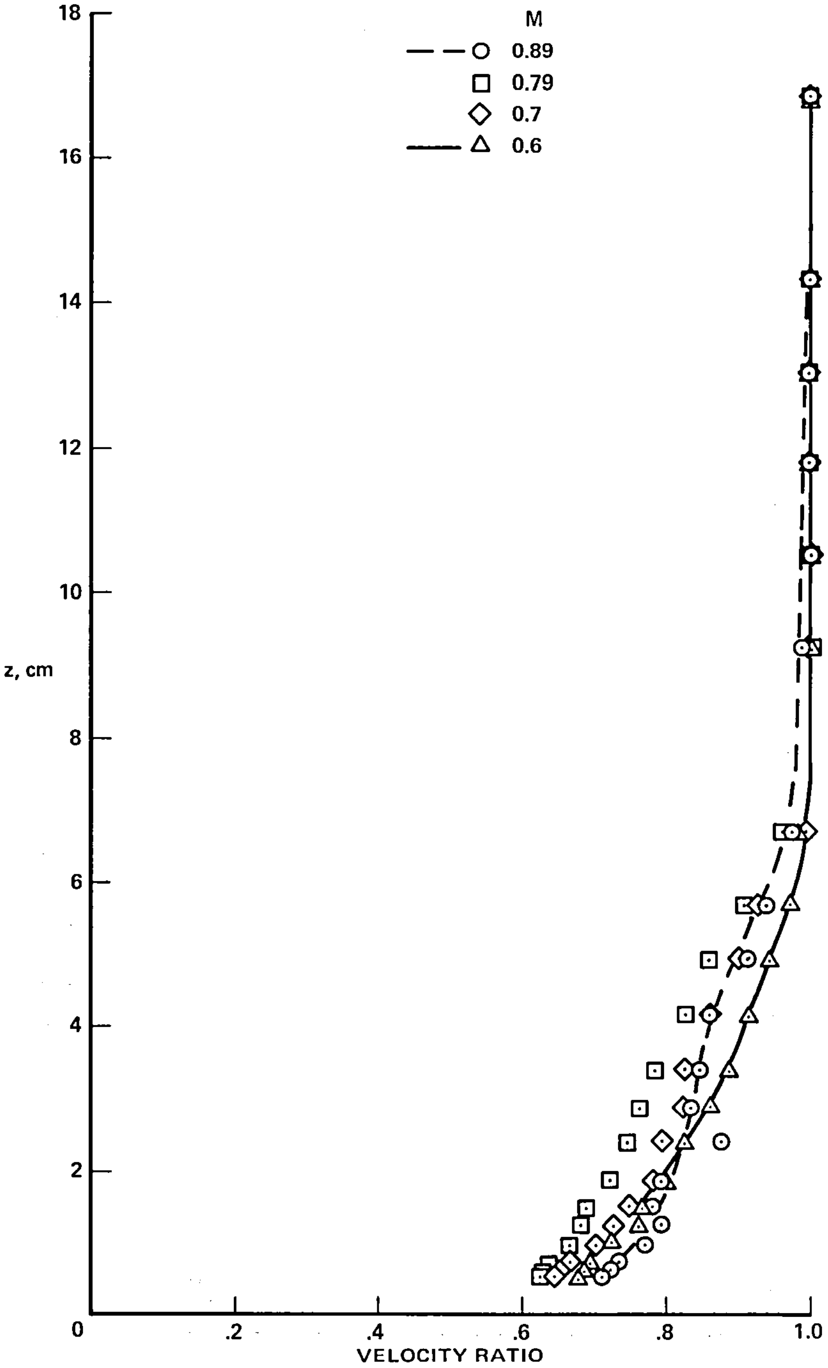

Figure 56.– Velocity profiles at various Mach numbers; Model 3, $R = 9.8 \times 10^6$/m, $x = 11.4$ cm, $y = 0$.

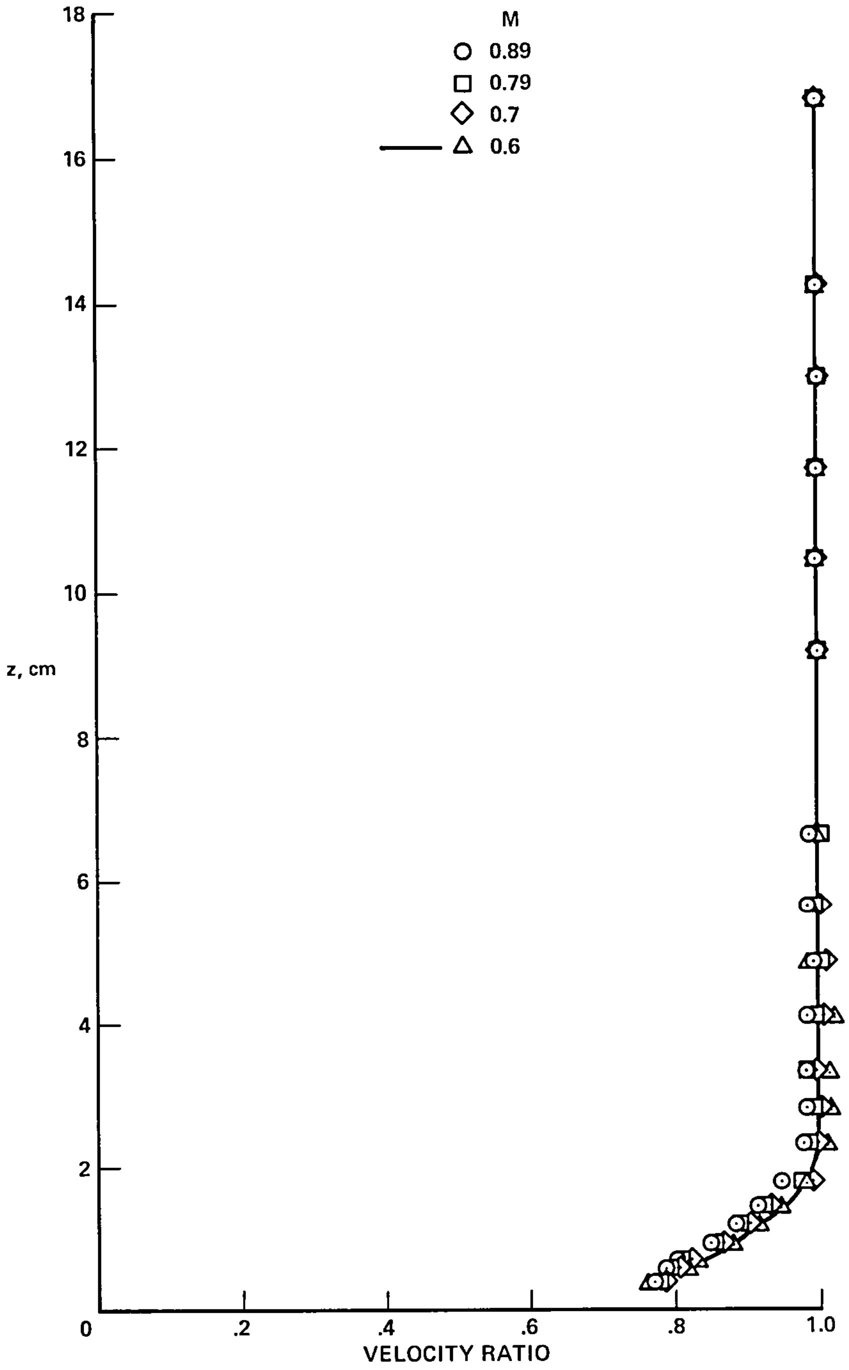

Figure 57.– Velocity profiles at various Mach numbers; Model 19, $R = 9.8 \times 10^6$/m, $x = 21.6$ cm, $y = 0$.

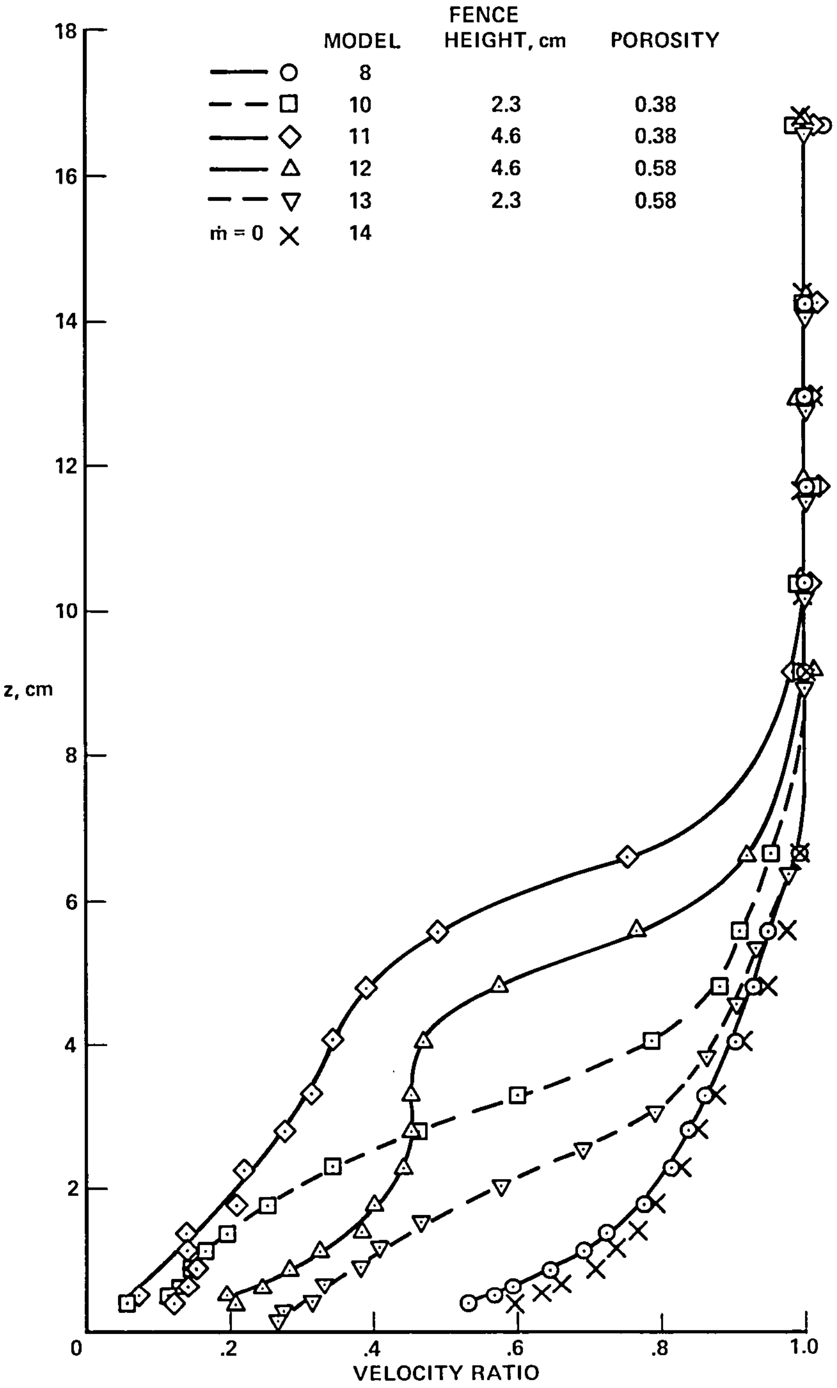

Figure 58.– Velocity profiles for cavity configurations; $M = 0.60$, $R = 9.8 \times 10^6$/m, $x = 7.6$ cm, $y = 0.1$ cm.

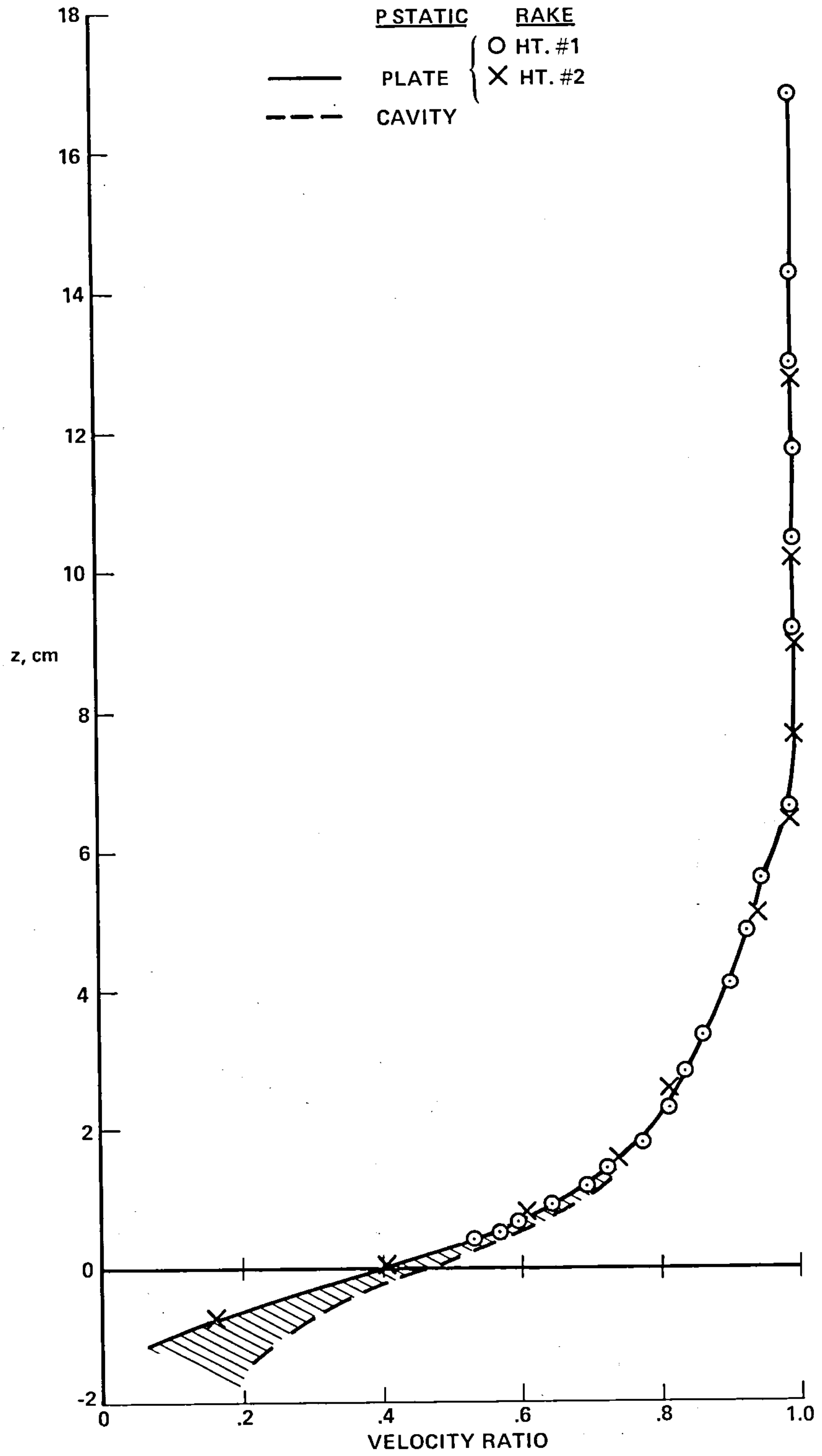

Figure 59.– Velocity profiles for various rake heights; Model 8, $M = 0.60$, $R = 9.8 \times 10^6$, $x = 7.6$ cm, $y = 0$.

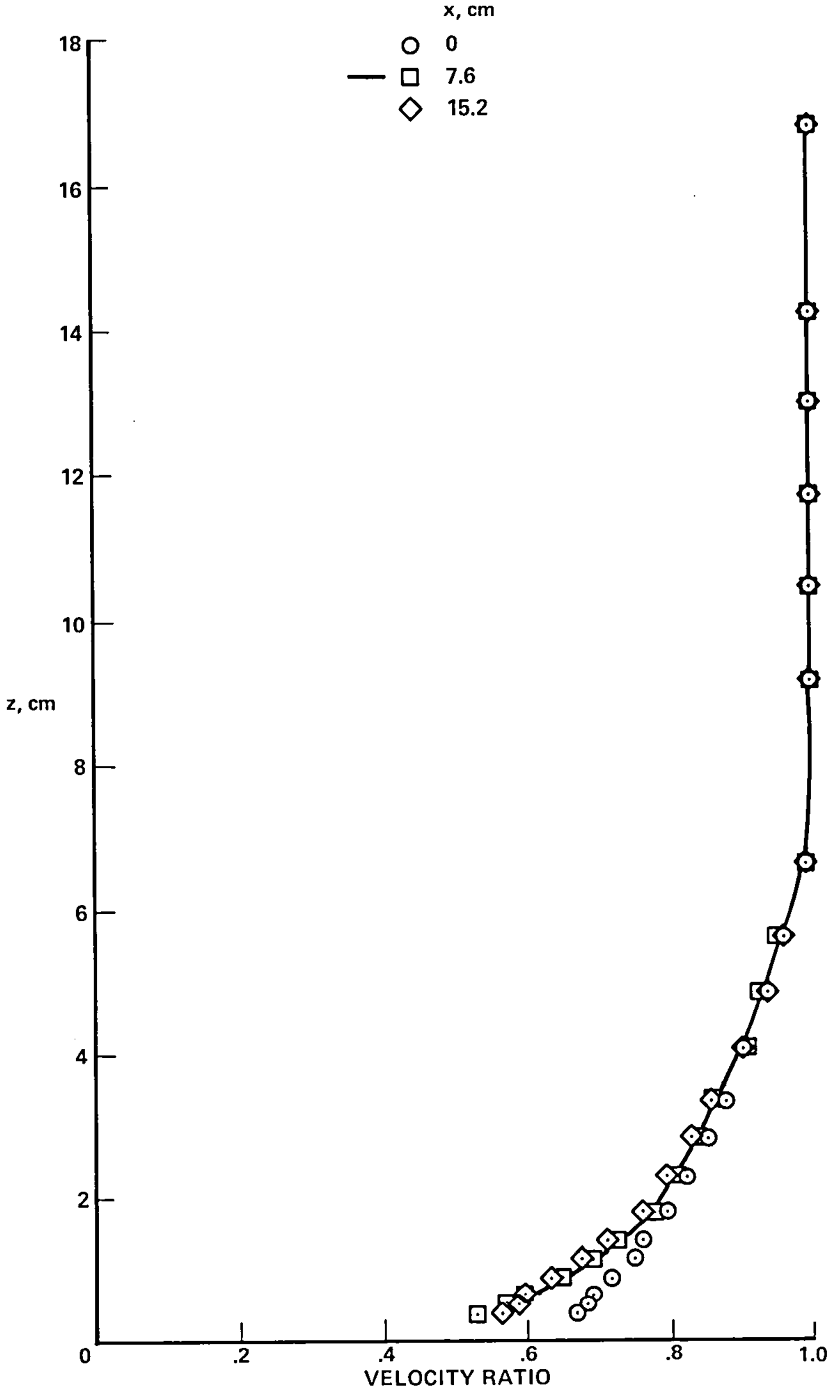

Figure 60.– Velocity profiles at various streamwise locations; Model 8, $M = 0.60$, $R = 9.8 \times 10^6$/m, $y = 0.1$ cm.

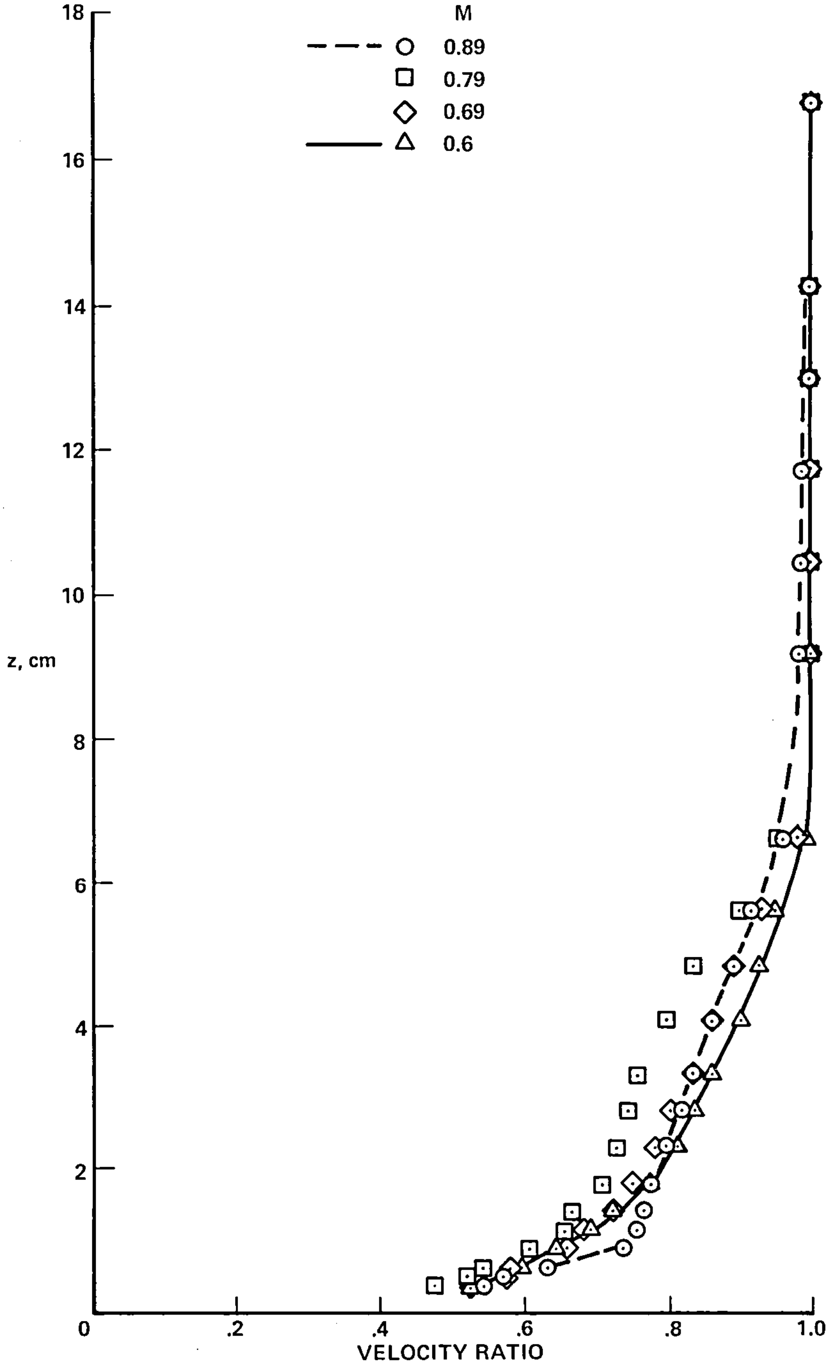

Figure 61.– Velocity profiles at various Mach numbers; Model 8, $R = 9.8 \times 10^6$/m, x = 7.6 cm, $y = 0$.

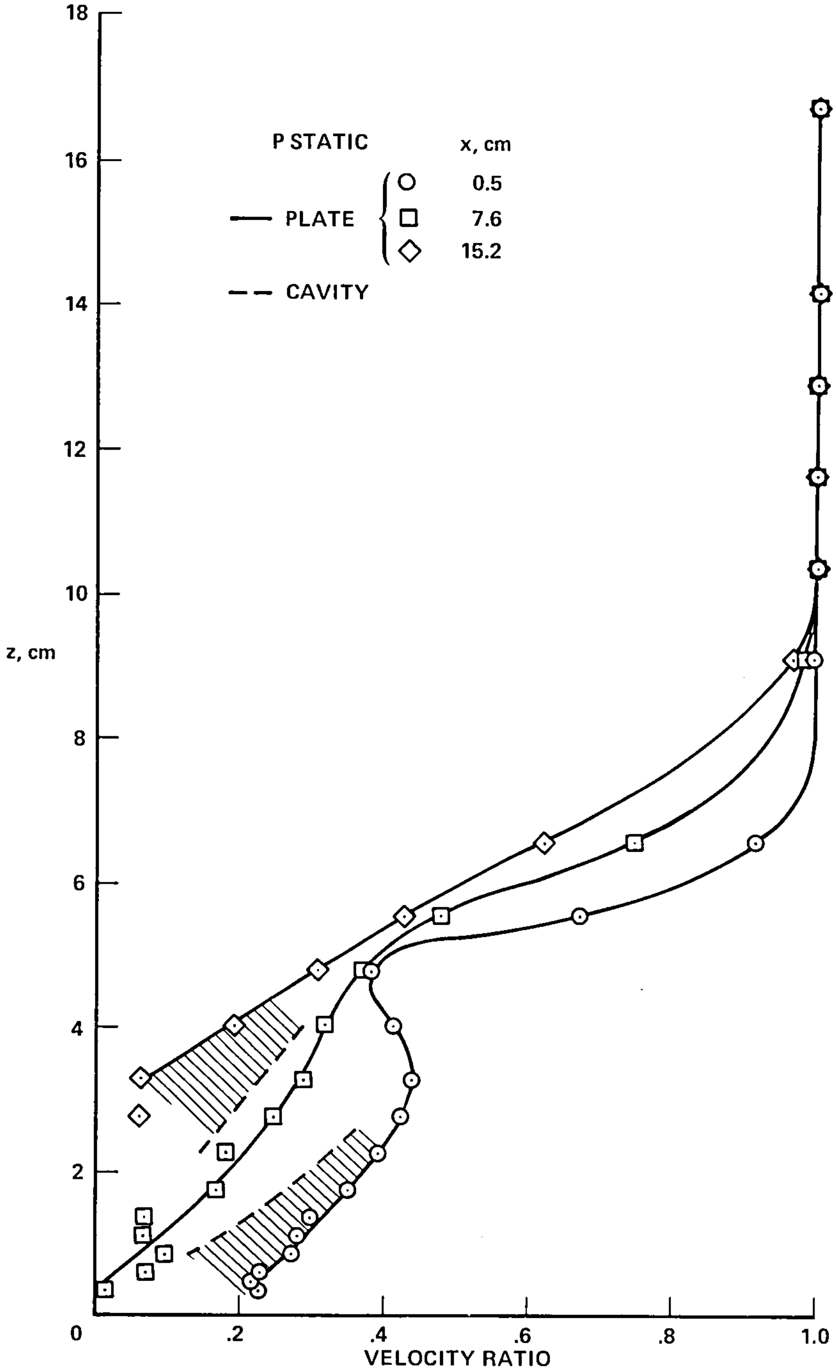

Figure 62.– Velocity profiles at various streamwise locations; Model 11, $M = 0.60$, $R = 9.8 \times 10^6$/m, $y = 0.1$ cm.

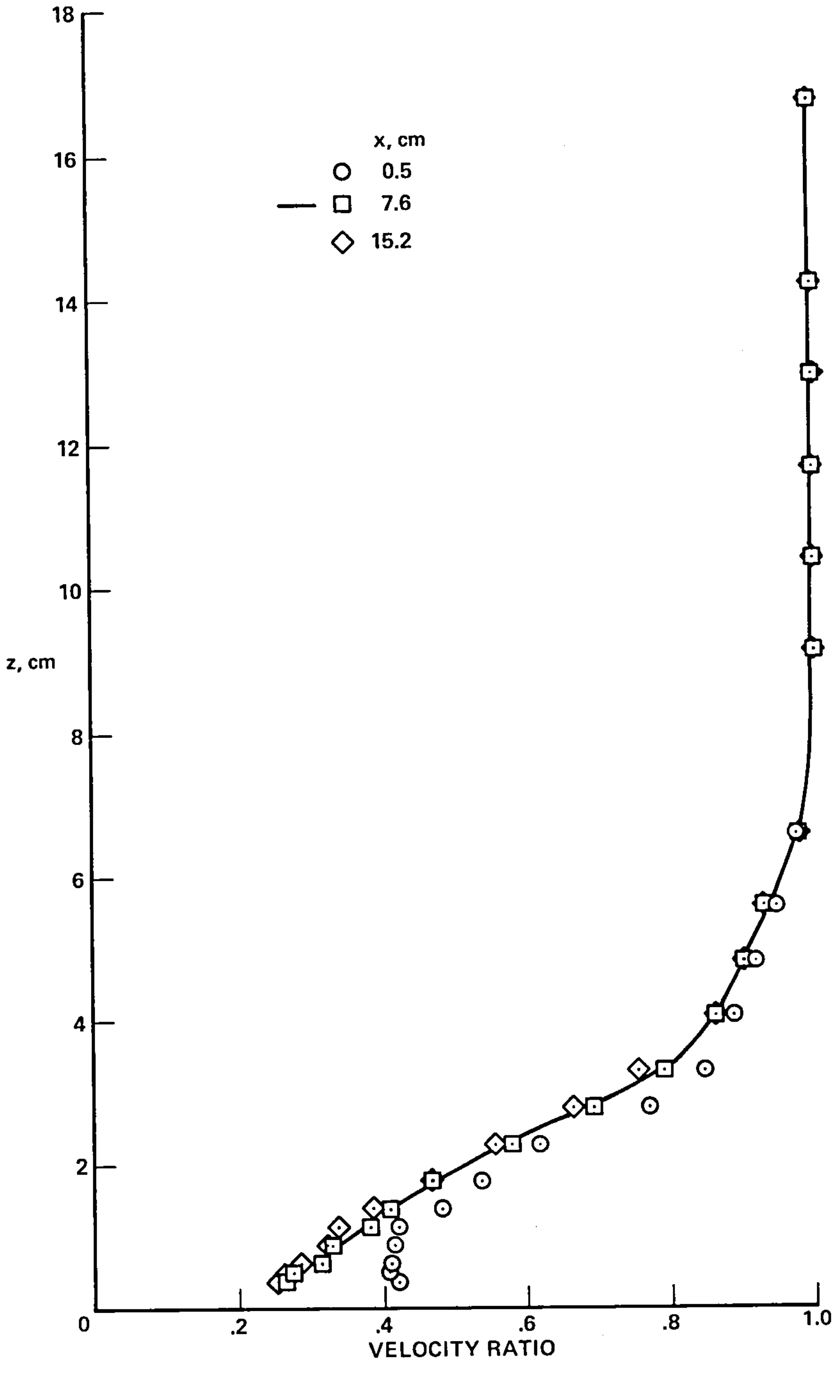

Figure 63.– Velocity profiles at various streamwise locations; Model 13, $M = 0.60$, $R = 9.8 \times 10^6$/m, $y = 0.1$ cm.

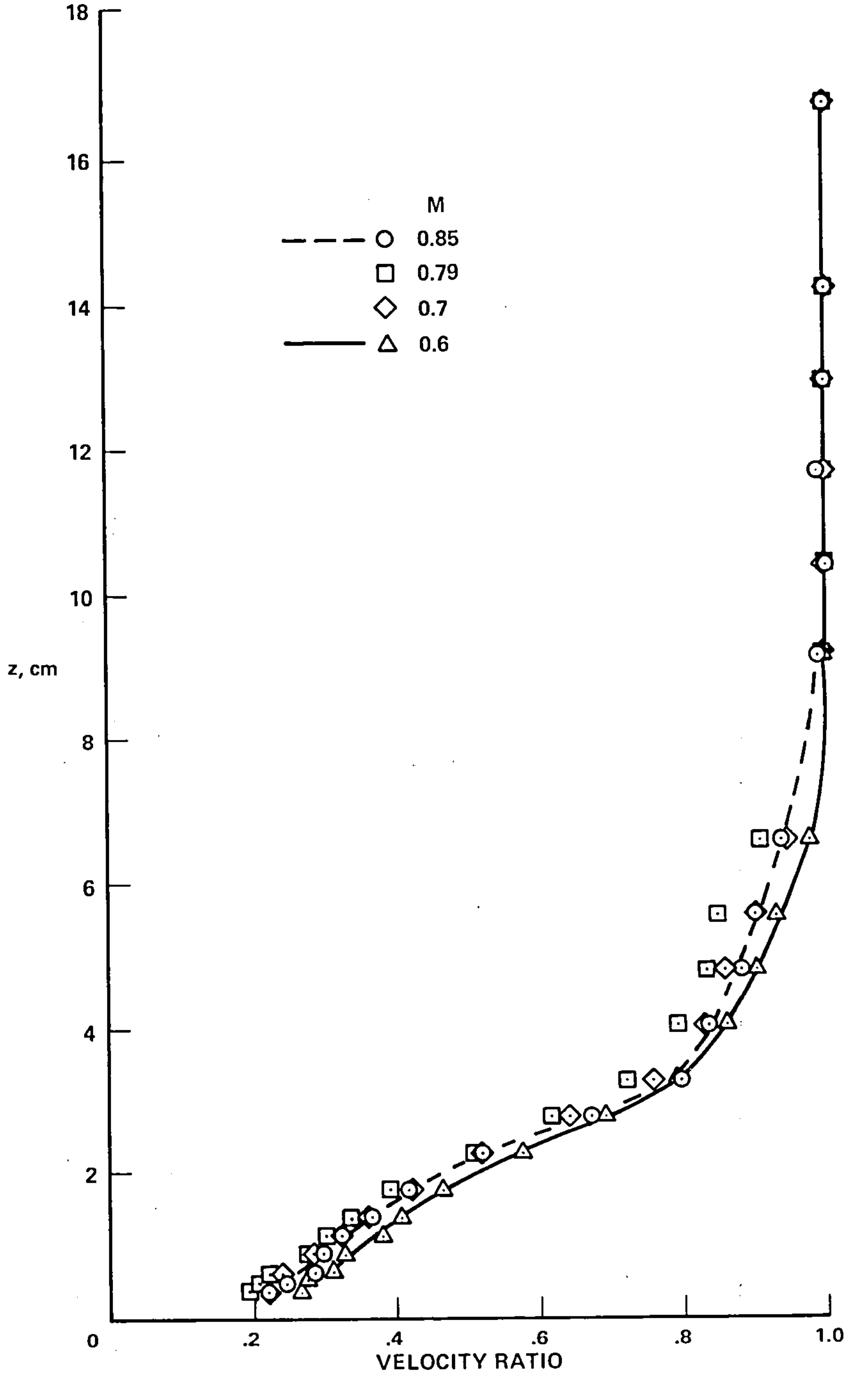

Figure 64.– Velocity profiles at various Mach numbers; Model 13, $R = 9.8 \times 10^6$/m, $x = 7.6$ cm, $y = 0.1$ cm.

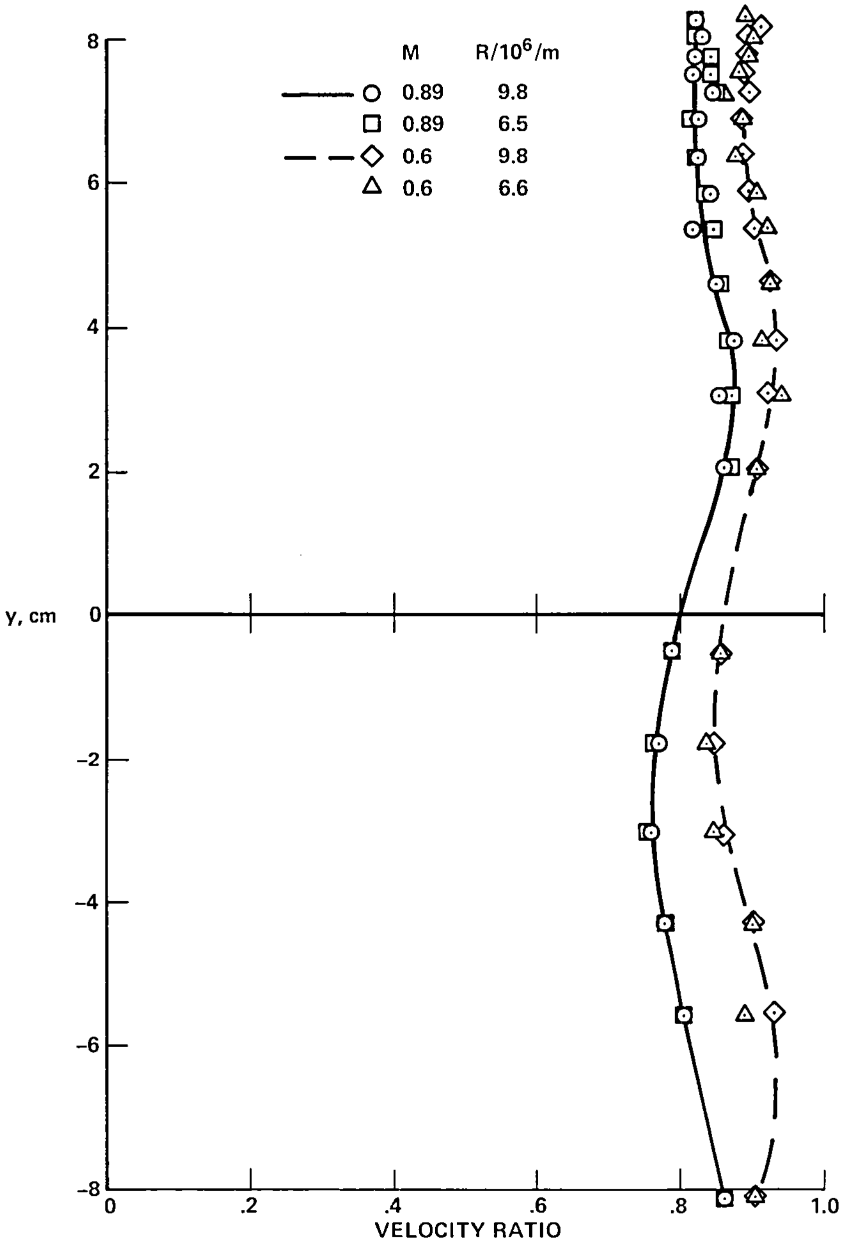

Figure 65.– Velocities in plane parallel to plate at various Mach and Reynolds numbers; Model 1, $x = 21.6$ cm, $z = 5.1$ cm.

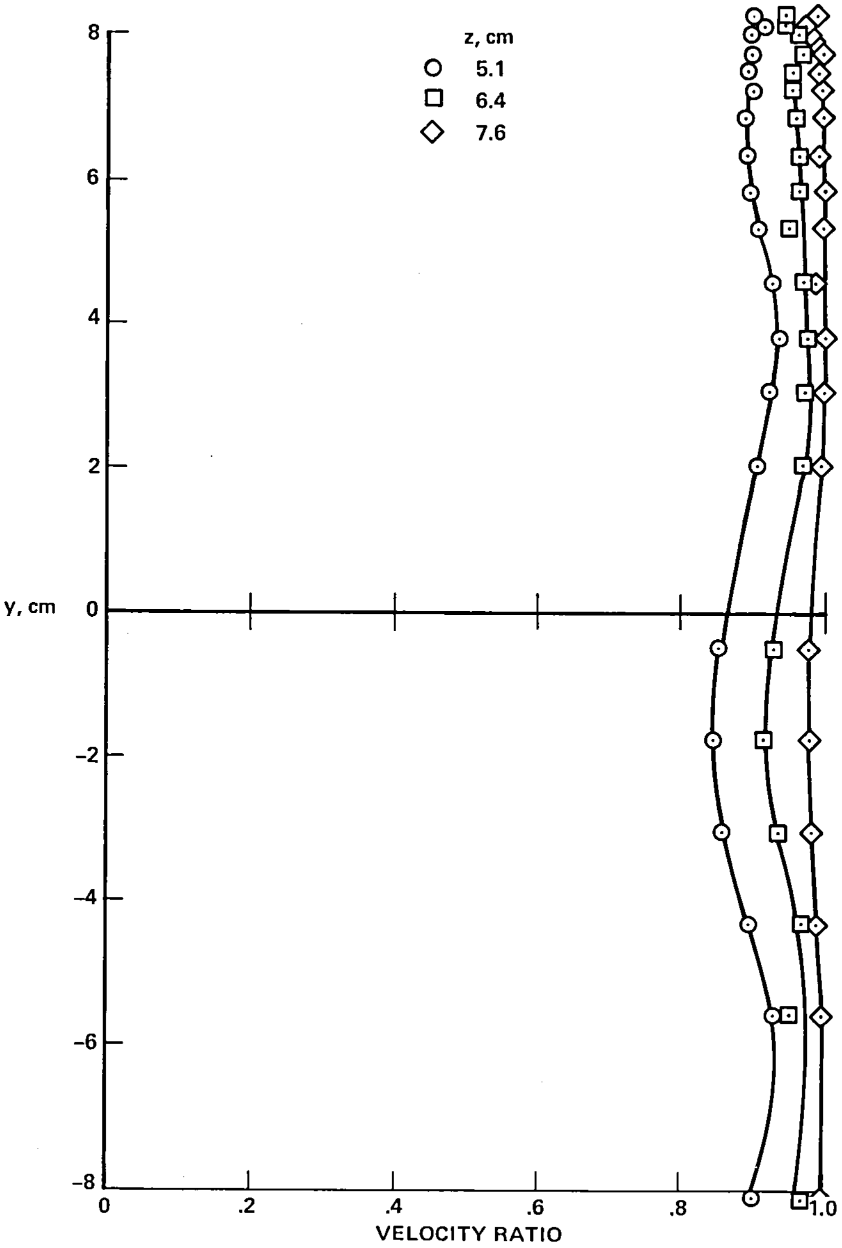

Figure 66.– Velocities in planes parallel to plate; Model 1, $M = 0.60$, $R = 9.8 \times 10^6$/m, $x = 21.6$ cm.

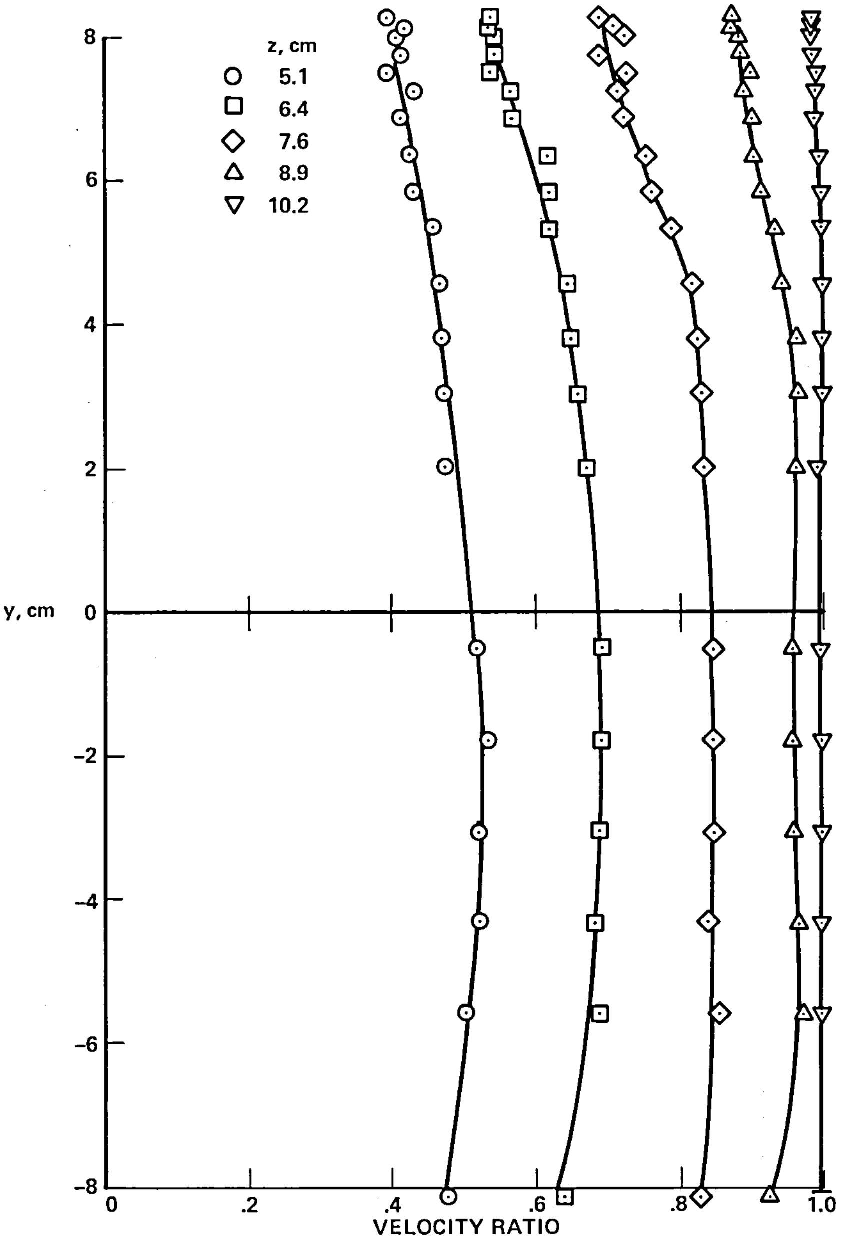

Figure 67.– Velocities in planes parallel to plate; Model 2, $M = 0.60$, $R = 9.6 \times 10^6$/m, $x = 21.6$ cm.

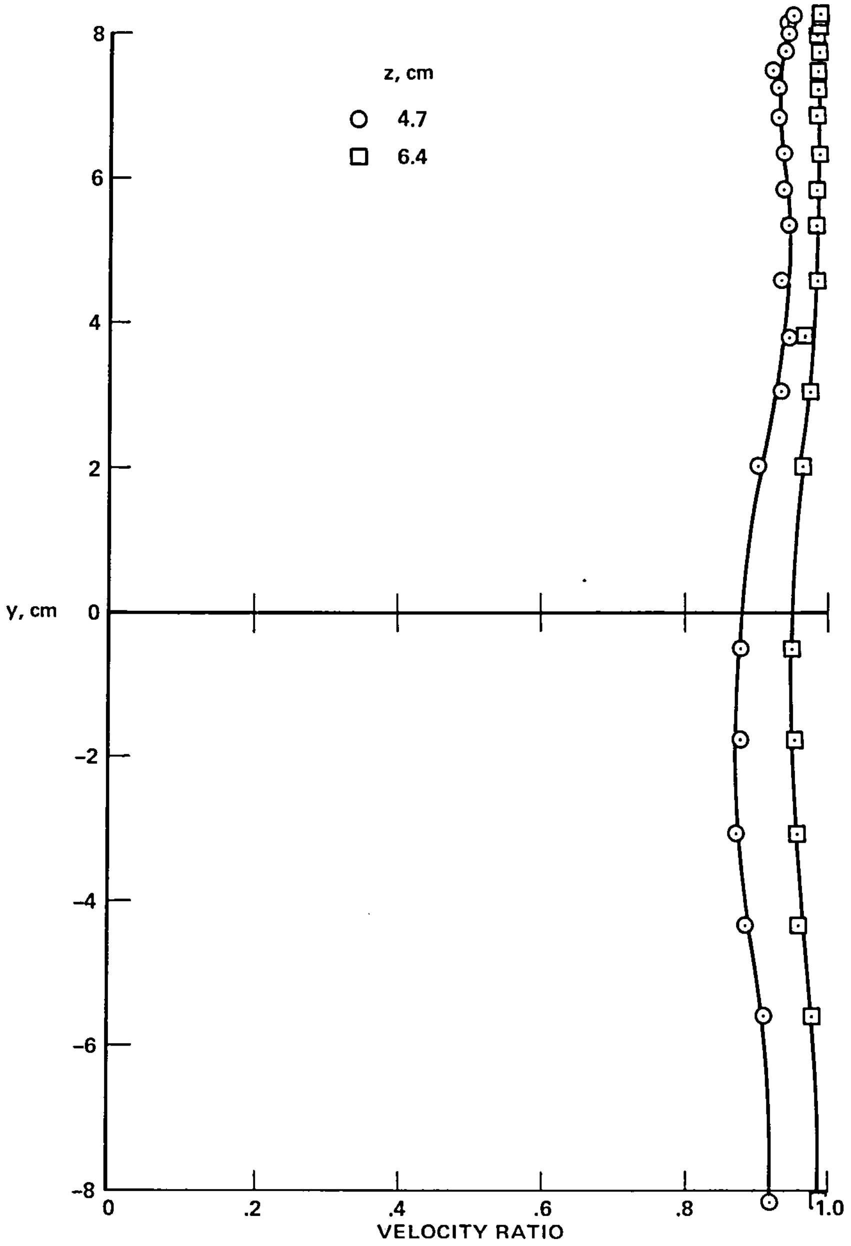

Figure 68.– Velocities in planes parallel to plate; Model 13, $M = 0.60$, $R = 9.8 \times 10^6$/m, $x = 15.2$ cm.

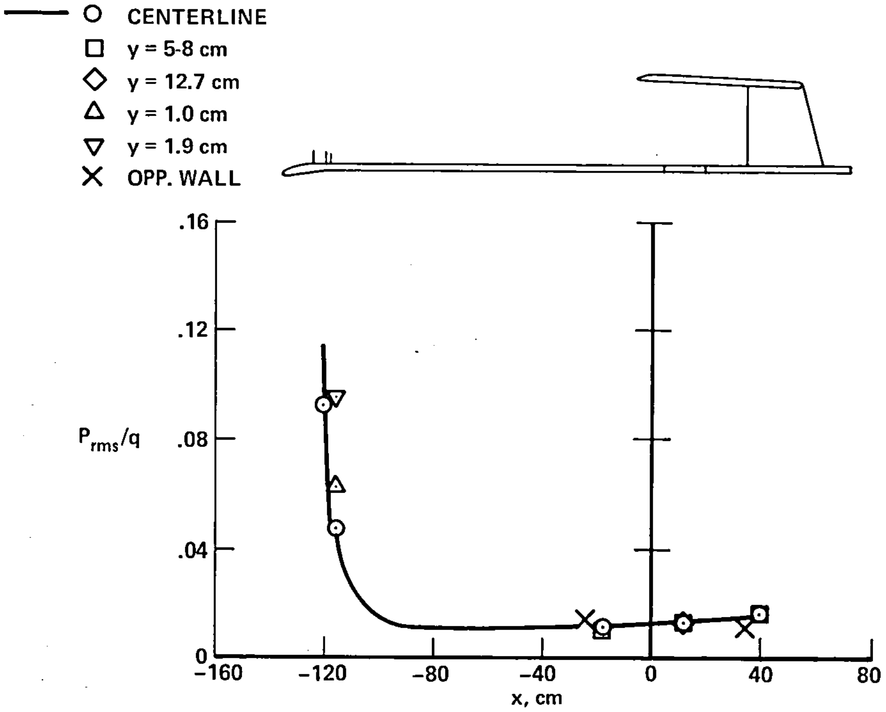

Figure 69.– Fluctuating-pressure coefficients on plate and wall; Model 1, Instrumentation 5, $M = 0.89, R = 9.8 \times 10^6$/m.

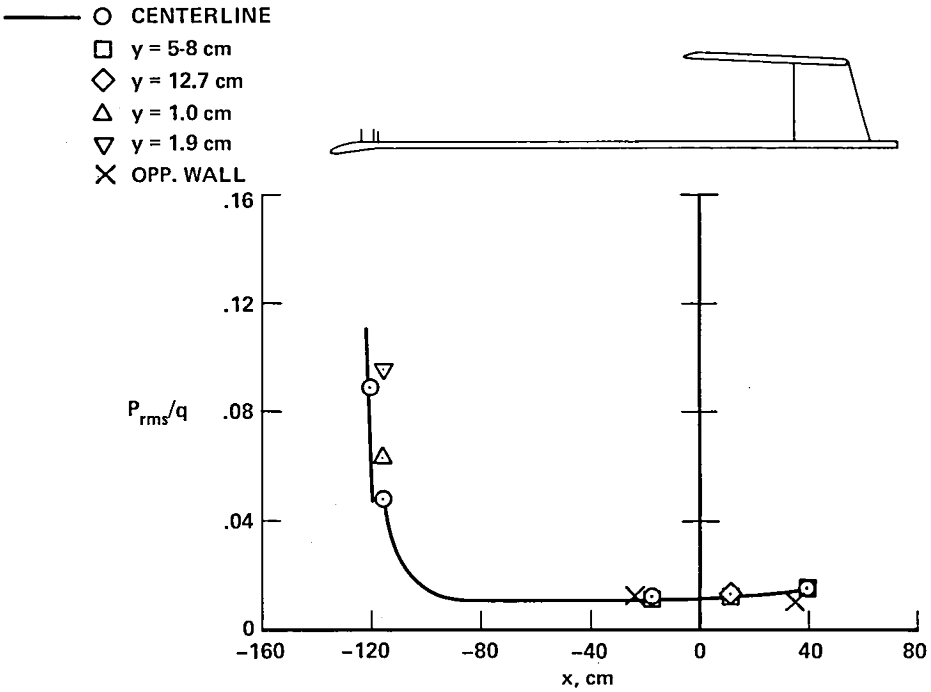

Figure 70.– Fluctuating-pressure coefficients on plate and wall; Model 1, Instrumentation 5, $M = 0.89, R = 6.5 \times 10^6$/m.

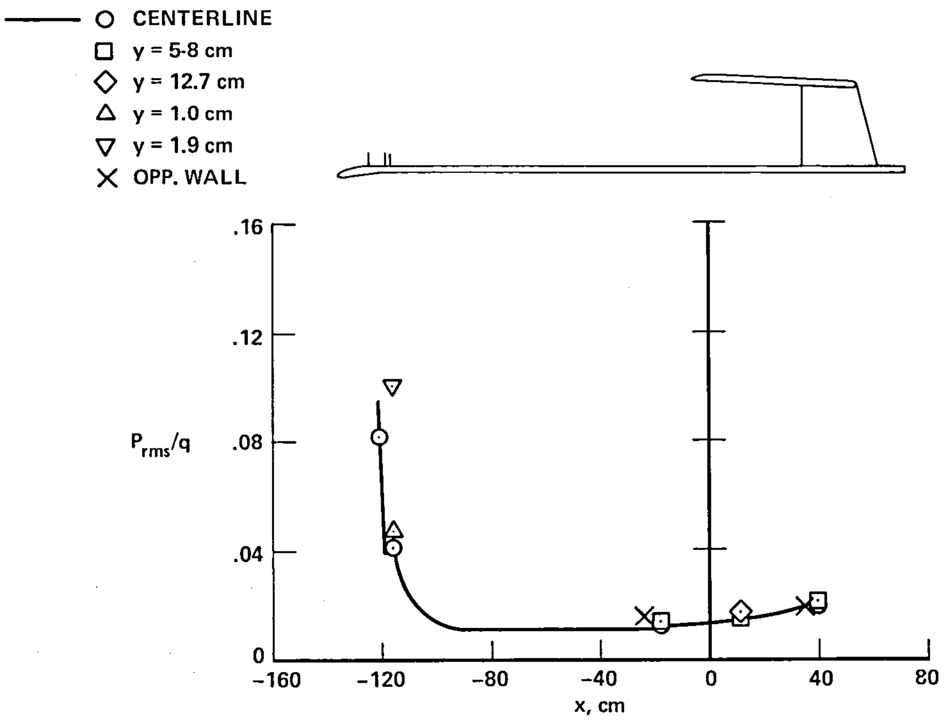

Figure 71.– Fluctuating-pressure coefficients on plate and wall; Model 1, Instrumentation 5, $M = 0.79$, $R = 9.8 \times 10^6$/m.

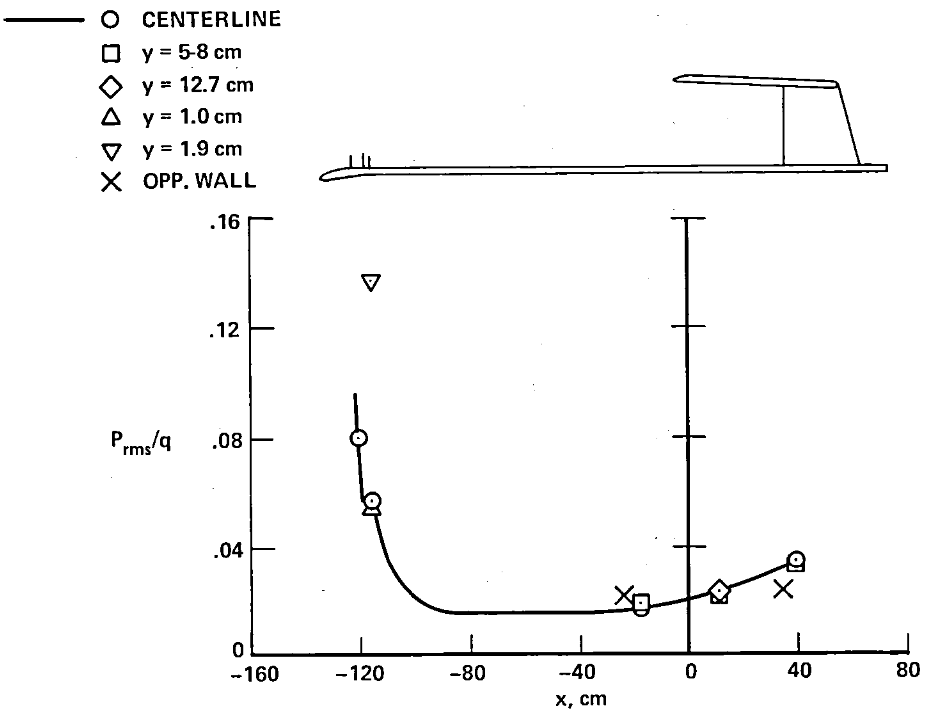

Figure 72.– Fluctuating-pressure coefficients on plate and wall; Model 1, Instrumentation 5, $M = 0.70$, $R = 9.8 \times 10^6$/m.

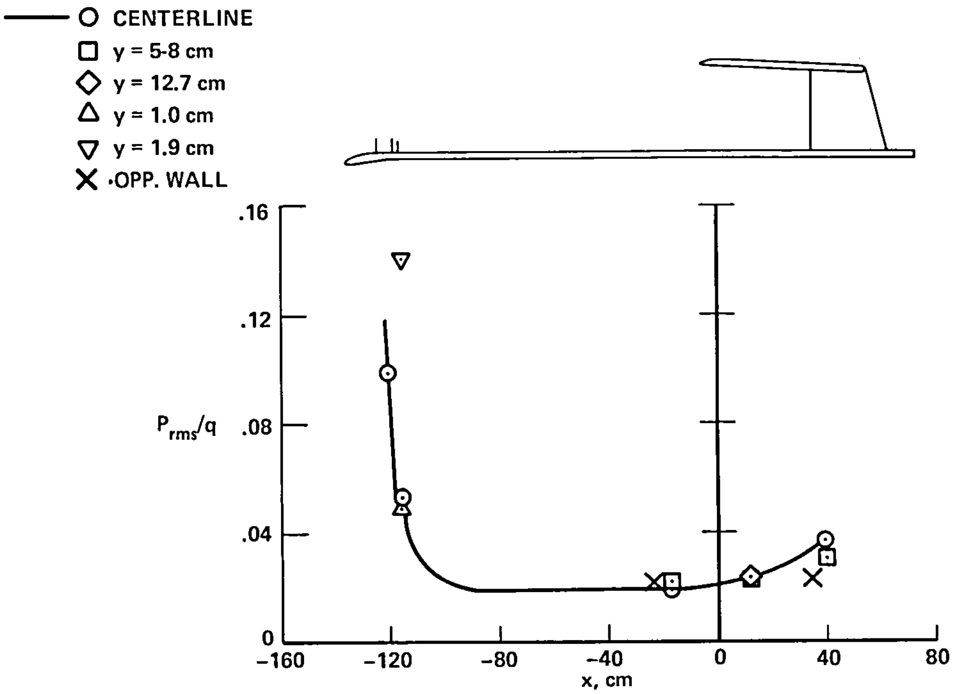

Figure 73.– Fluctuating-pressure coefficients on plate and wall; Model 1, Instrumentation 5, $M = 0.60, R = 9.8 \times 10^6$/m.

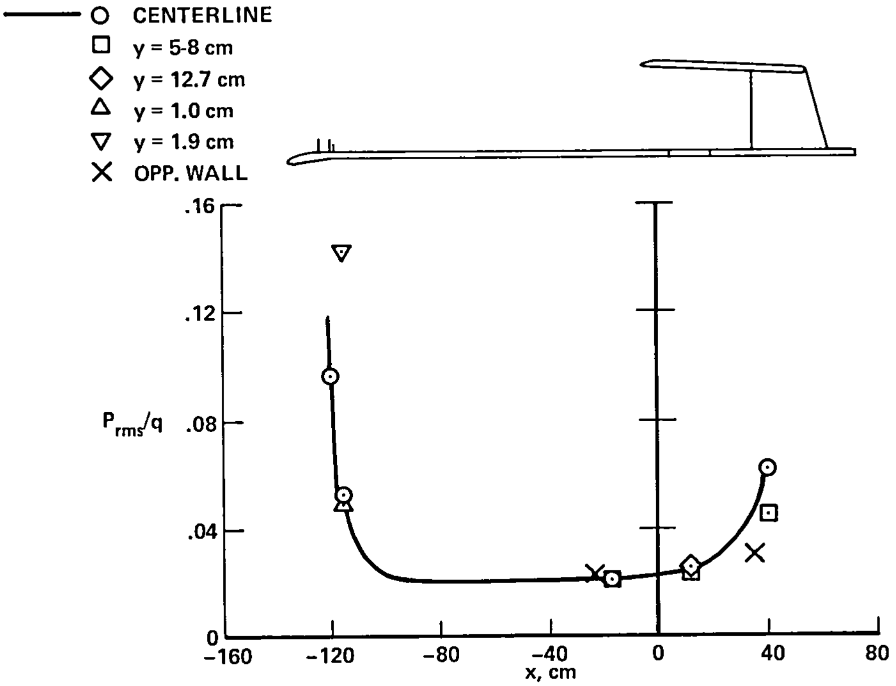

Figure 74.– Fluctuating-pressure coefficients on plate and wall; Model 1, Instrumentation 5, $M = 0.60, R = 6.6 \times 10^6$/m.

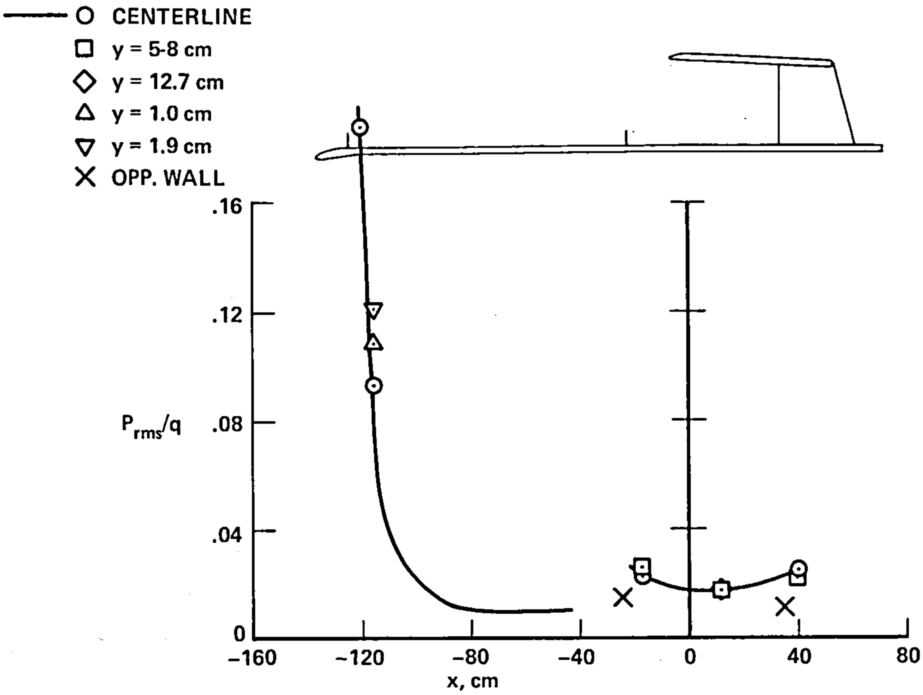

Figure 75.– Fluctuating-pressure coefficients on plate and wall; Model 2, Instrumentation 5, $M = 0.89, R = 9.7\times10^6$/m.

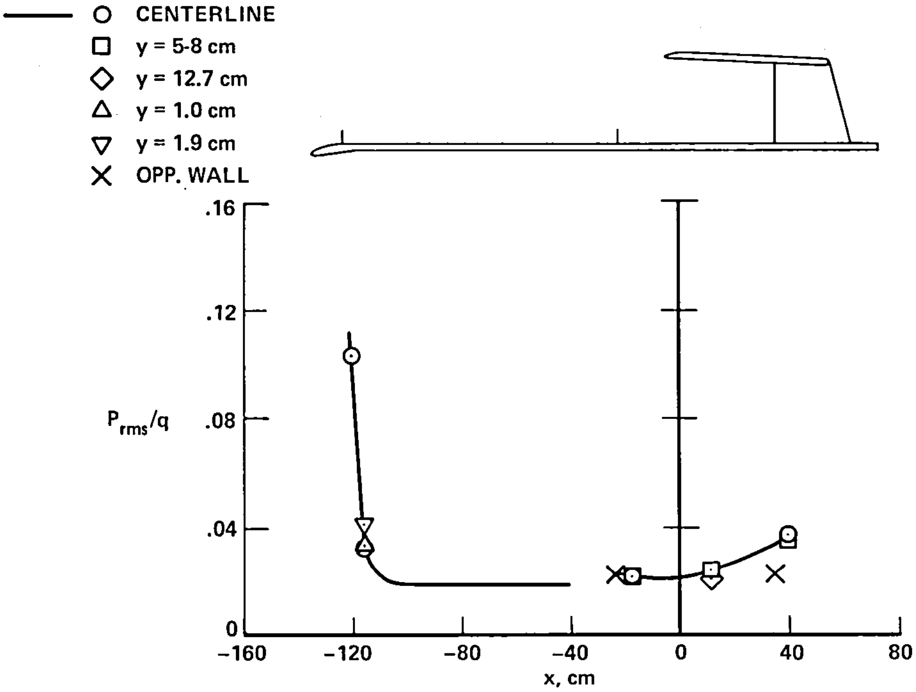

Figure 76.– Fluctuating-pressure coefficients on plate and wall; Model 2, Instrumentation 5, $M = 0.60, R = 9.7\times10^6$/m.

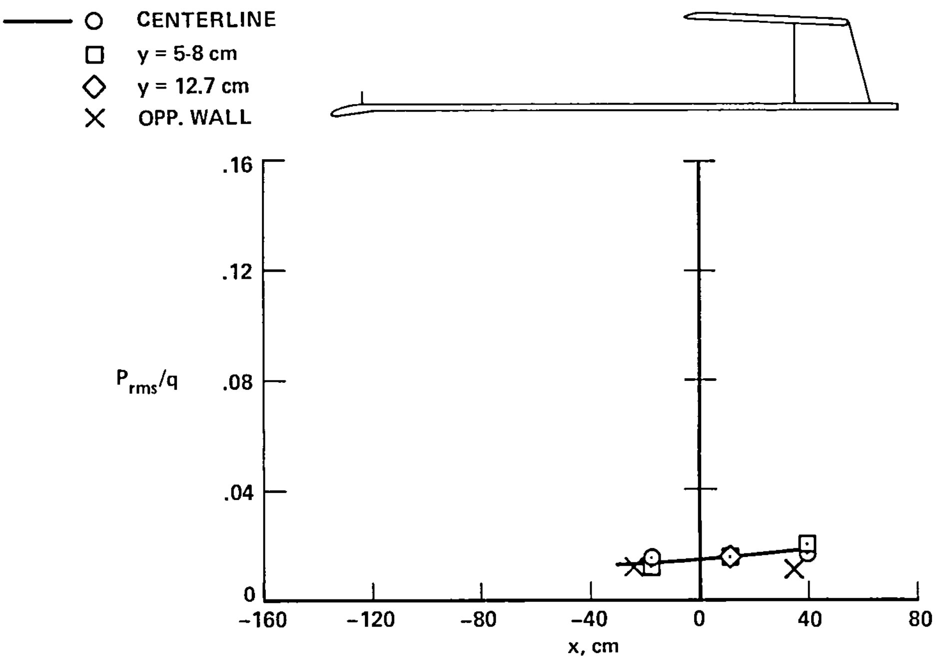

Figure 77.– Fluctuating-pressure coefficients on plate and wall; Model 3, Instrumentation 1, $M = 0.89$, $R = 9.7 \times 10^6$/m, amplifiers wide-band.

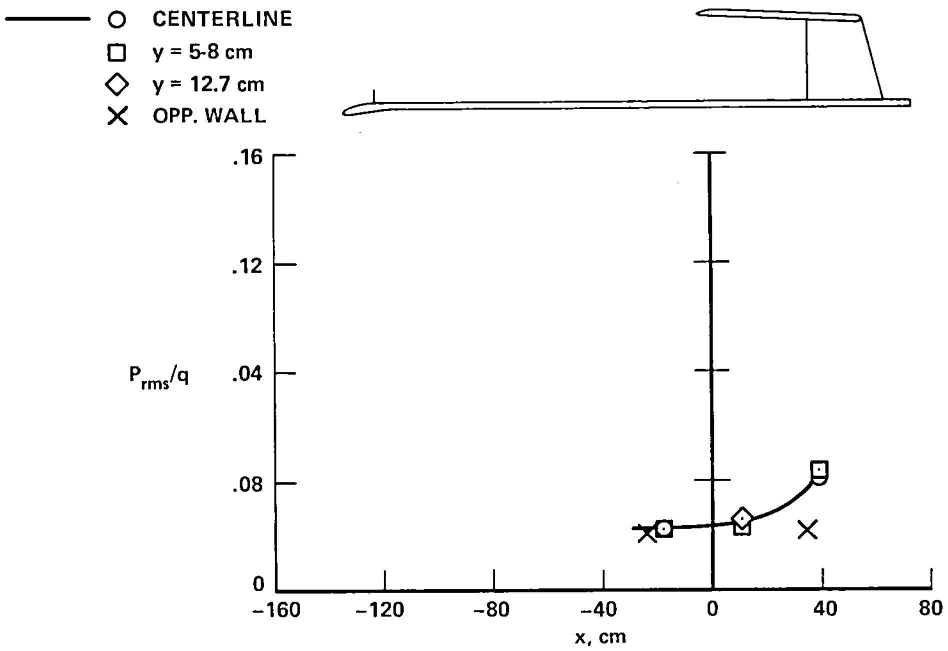

Figure 78.– Fluctuating-pressure coefficients on plate and wall; Model 3, Instrumentation 1, $M = 0.60$, $R = 9.8 \times 10^6$/m, amplifiers wide-band.

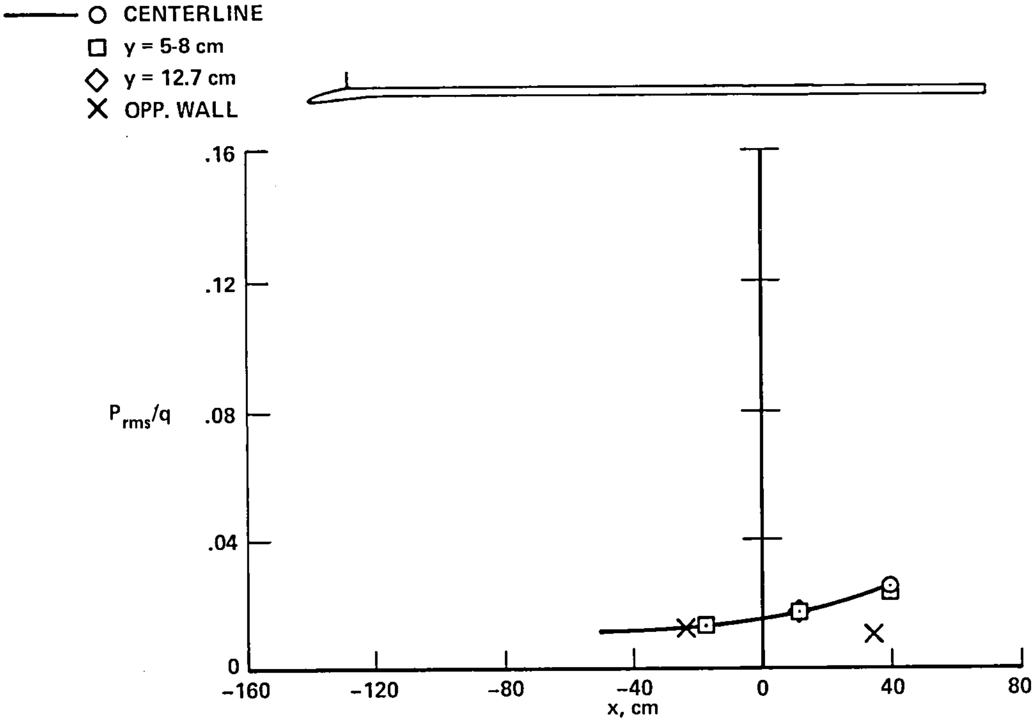

Figure 79.– Fluctuating-pressure coefficients on plate and wall; Model 4, Instrumentation 1, $M = 0.89$, $R = 9.9 \times 10^6$/m, amplifiers wide-band.

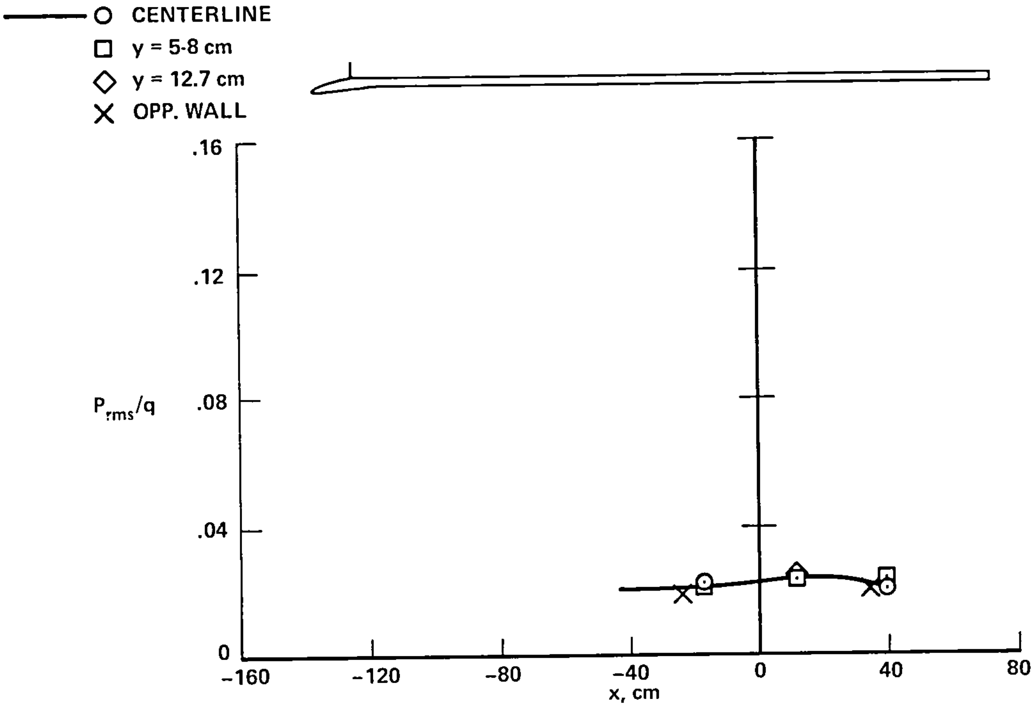

Figure 80.– Fluctuating-pressure coefficients on plate and wall; Model 4, Instrumentation 1, $M = 0.60$, $R = 6.6 \times 10^6$/m, amplifiers wide-band.

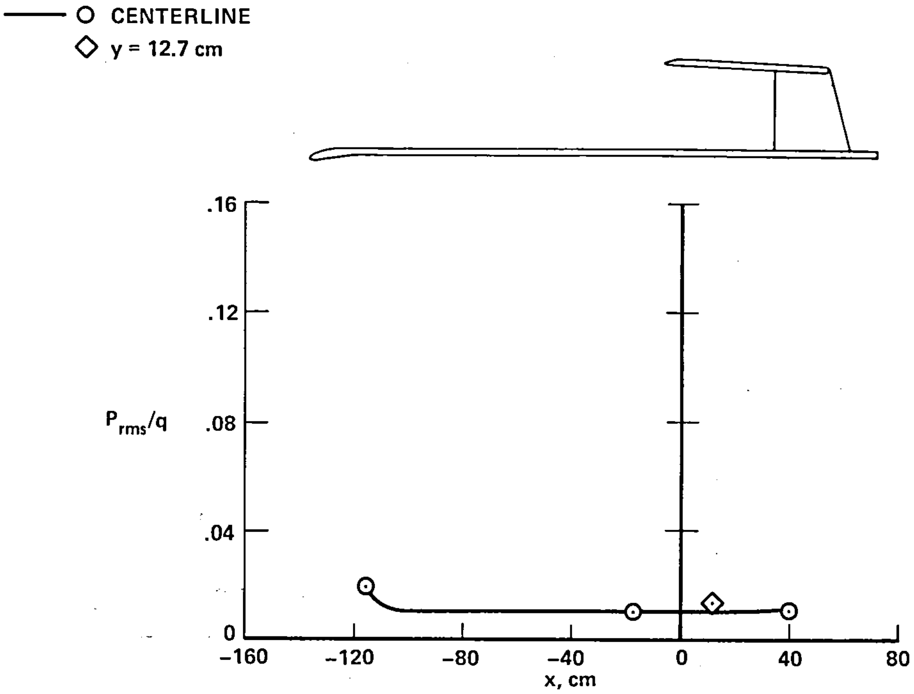

Figure 81.– Fluctuating-pressure coefficients on plate and wall; Model 19, Instrumentation 5, $M = 0.89$, $R = 9.8 \times 10^6$/m.

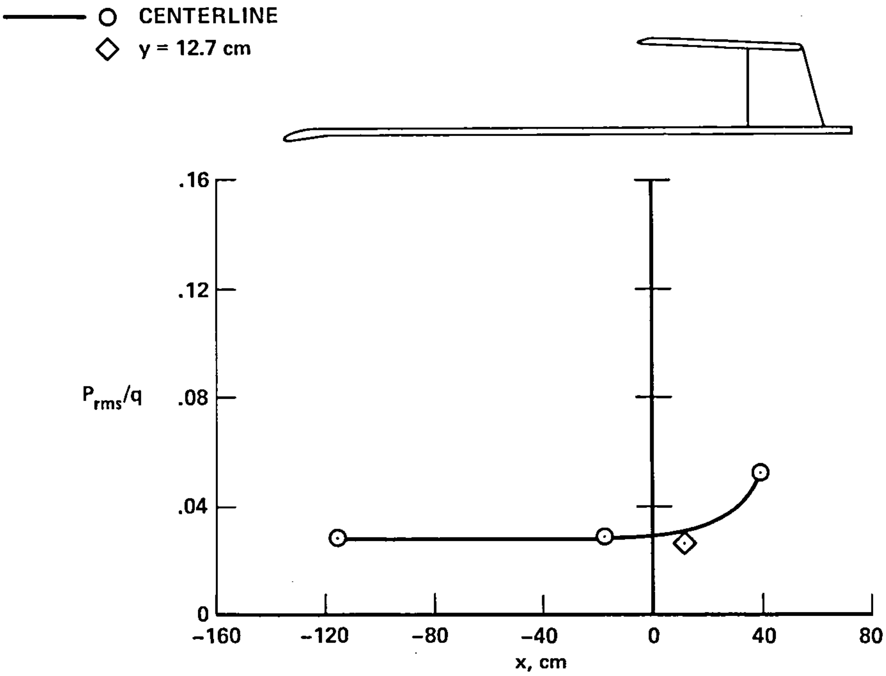

Figure 82.– Fluctuating-pressure coefficients on plate and wall; Model 19, Instrumentation 5, $M = 0.60$, $R = 9.8 \times 10^6$/m.

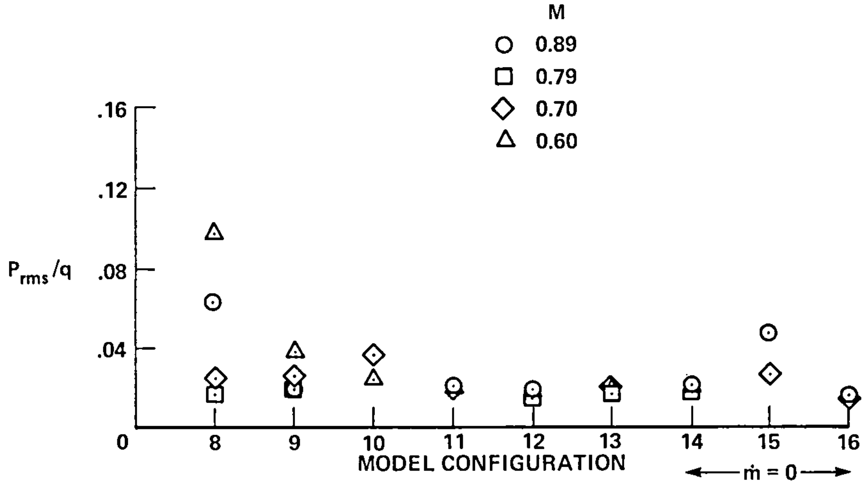

Figure 83.– Fluctuating-pressure coefficients in the cavity for various configurations; FP123, $R = 9.8 \times 10^6$/m.

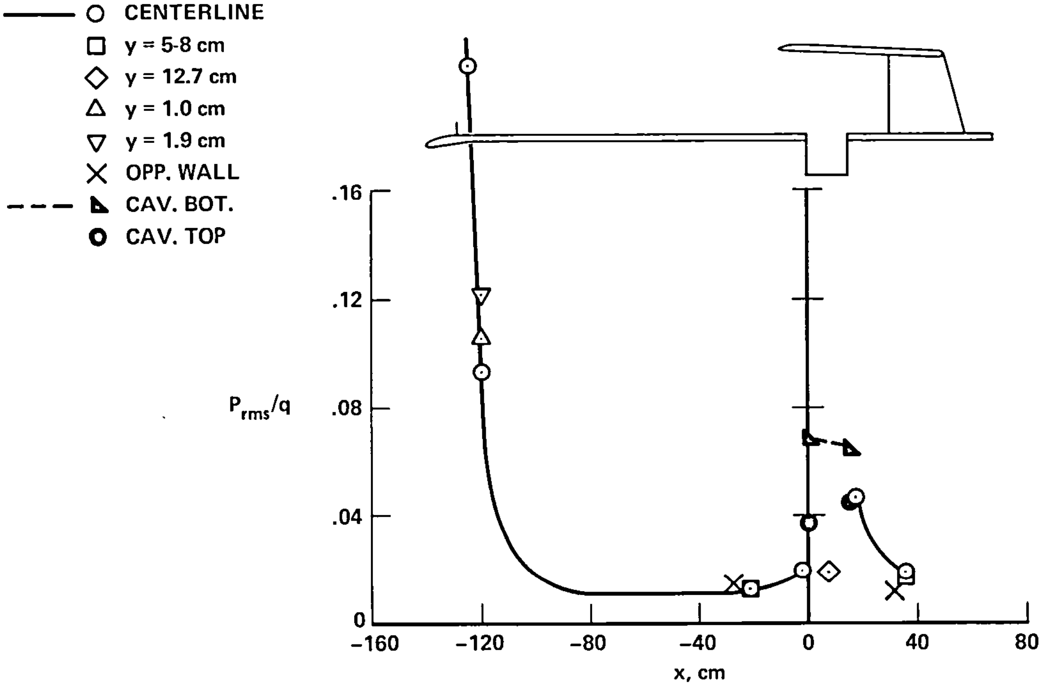

Figure 84.– Fluctuating-pressure coefficients on plate, wall, and cavity; Model 8, Instrumentation 7, $M = 0.89$, $R = 9.8 \times 10^6$/m.

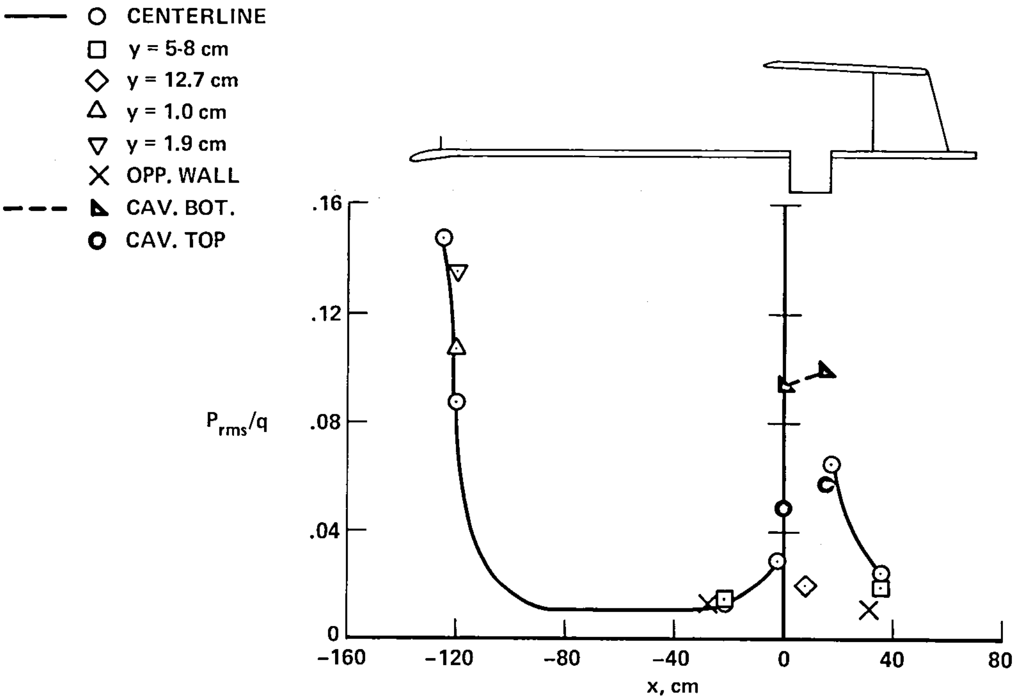

Figure 85.– Fluctuating-pressure coefficients on plate, wall, and cavity; Model 8, Instrumentation 7, $M = 0.89, R = 6.6\times10^6/\text{m}$.

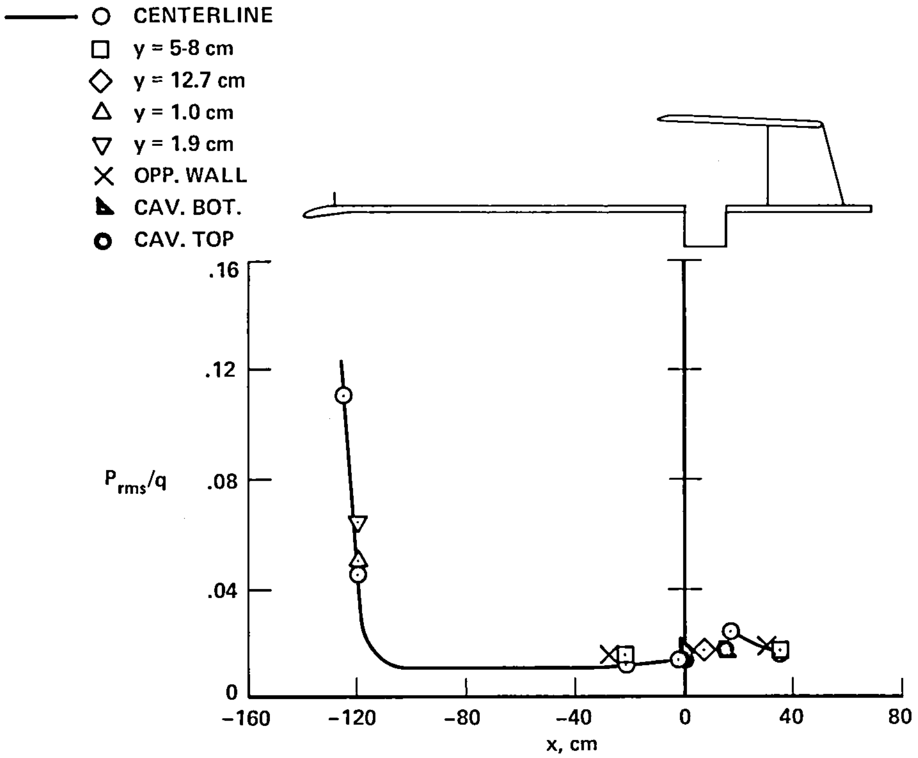

Figure 86.– Fluctuating-pressure coefficients on plate, wall, and cavity; Model 8, Instrumentation 7, $M = 0.80$, $R = 9.7 \times 10^6$/m.

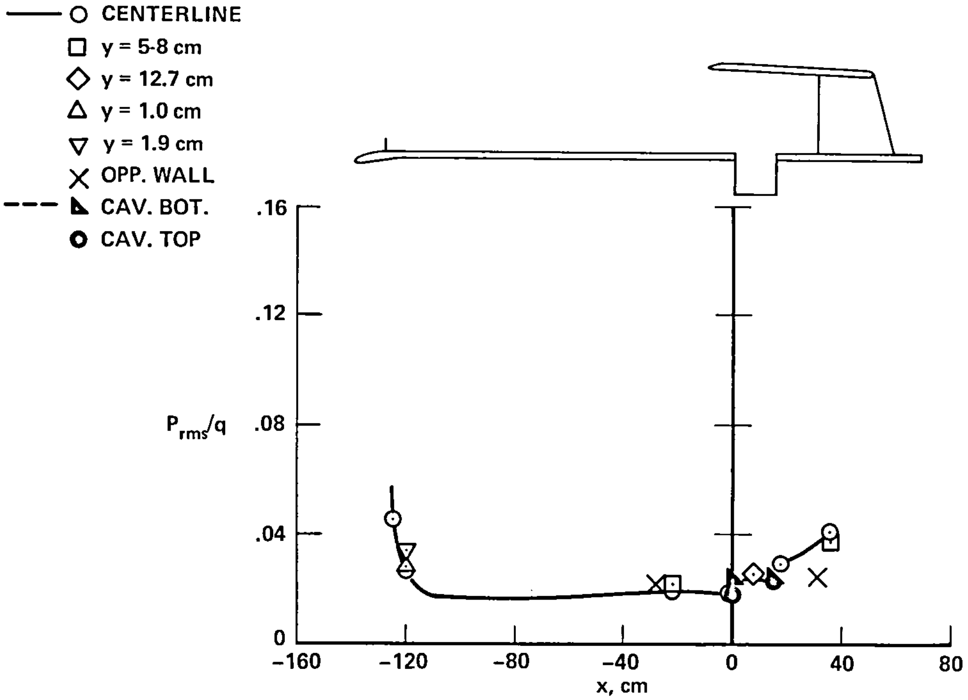

Figure 87.– Fluctuating-pressure coefficients on plate, wall, and cavity; Model 8, Instrumentation 7, $M = 0.70, R = 9.7 \times 10^6$/m.

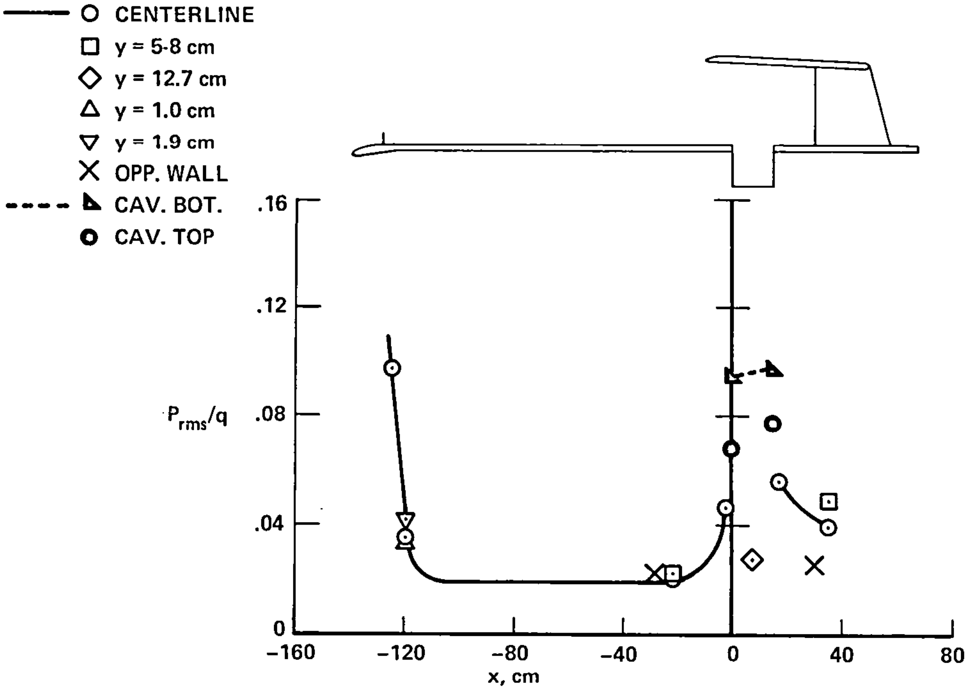

Figure 88 Fluctuating-pressure coefficients on plate, wall, and cavity, Model 8, Instrumentation 7, $M = 0.60, R = 9.8 \times 10^6$/m.

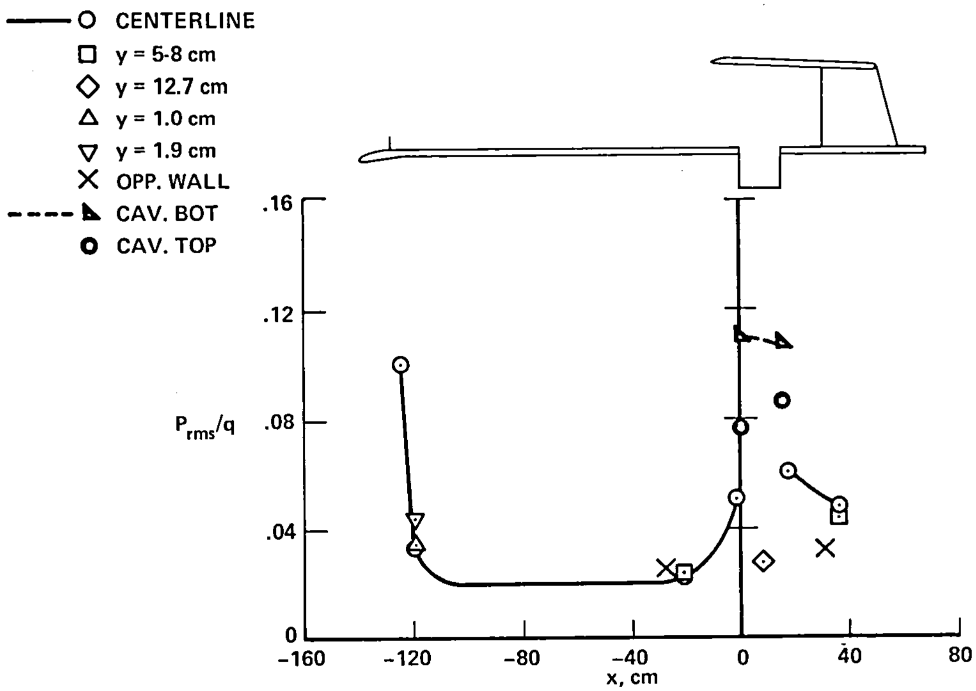

Figure 89.– Fluctuating-pressure coefficients on plate, wall, and cavity; Model 8, Instrumentation 7, $M = 0.60$, $R = 6.6 \times 10^6$/m.

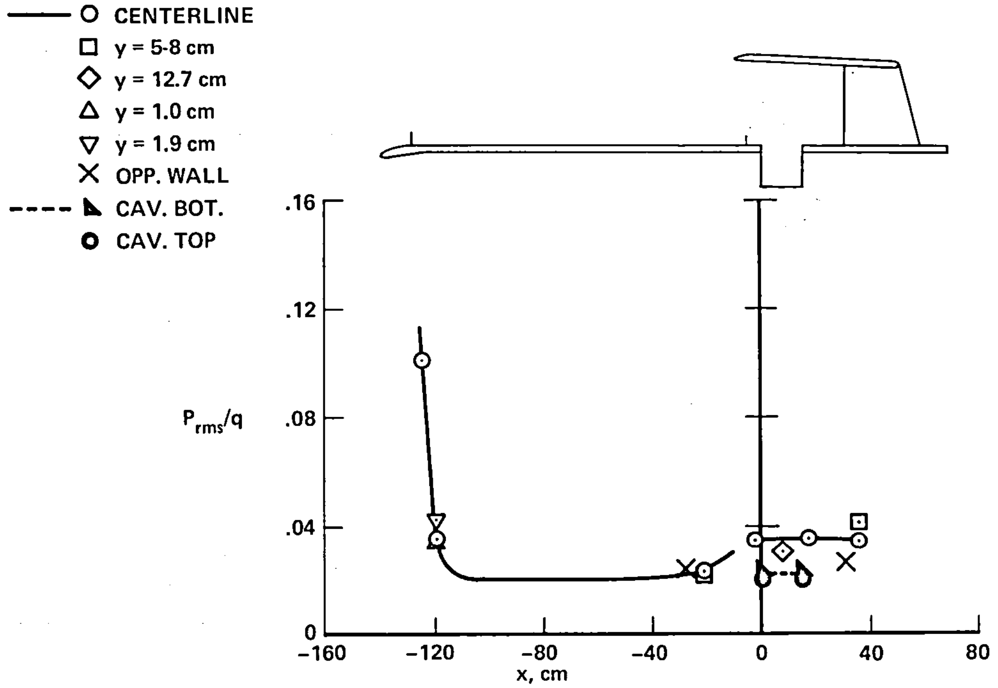

Figure 90.– Fluctuating-pressure coefficients on plate, wall, and cavity; Model 10, Instrumentation 7, $M = 0.60$, $R = 9.8 \times 10^6$/m.

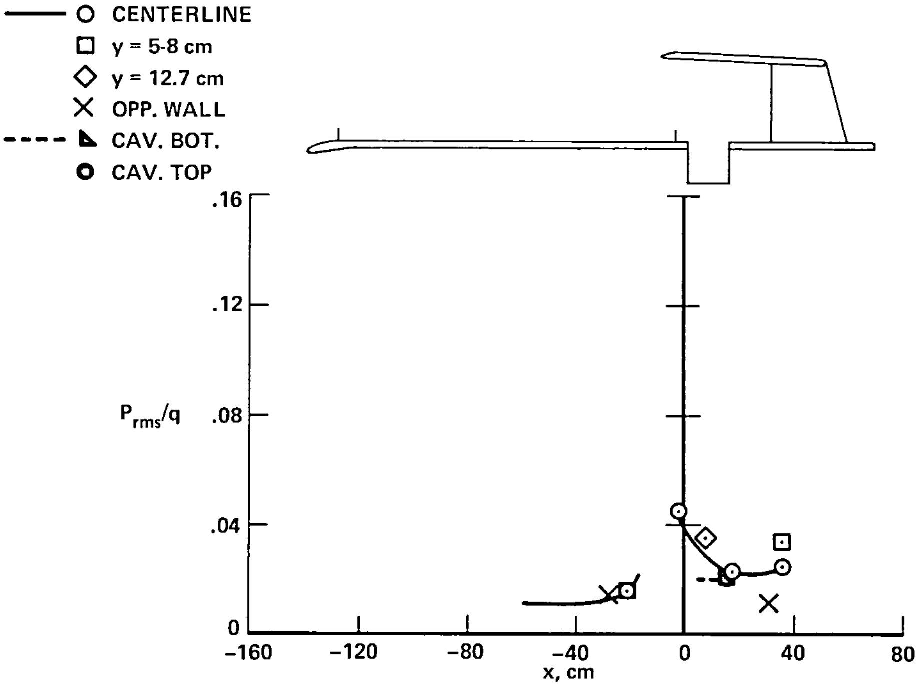

Figure 91.– Fluctuating-pressure coefficients on plate, wall, and cavity; Model 11, Instrumentation 2, $M = 0.89$, $R = 9.8\text{X}10^6$/m.

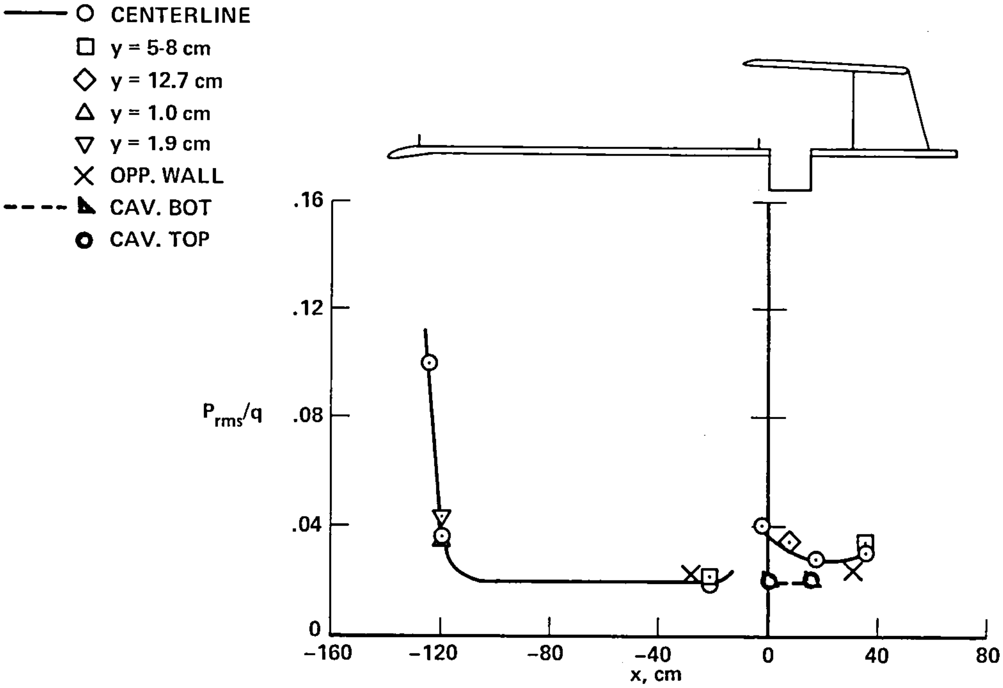

Figure 92.– Fluctuating-pressure coefficients on plate, wall, and cavity; Model 11, Instrumentation 7, $M = 0.60$, $R = 9.8\text{X}10^6$/m.

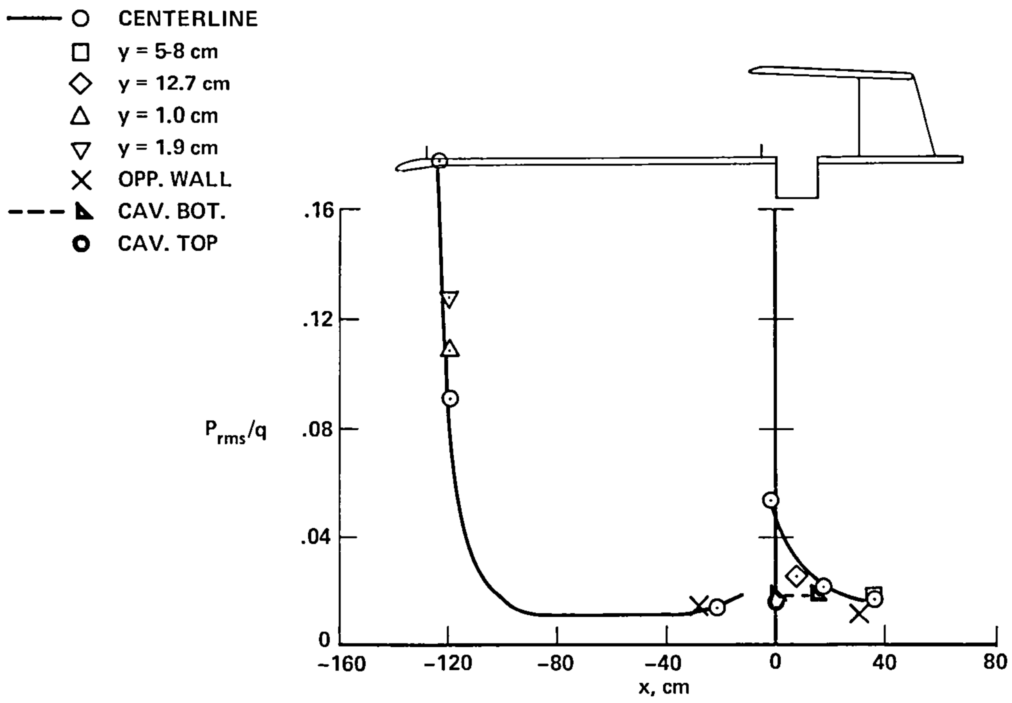

Figure 93.– Fluctuating-pressure coefficients on plate, wall, and cavity; Model 12, Instrumentation 7, $M = 0.89$, $R = 9.8 \times 10^6$/m.

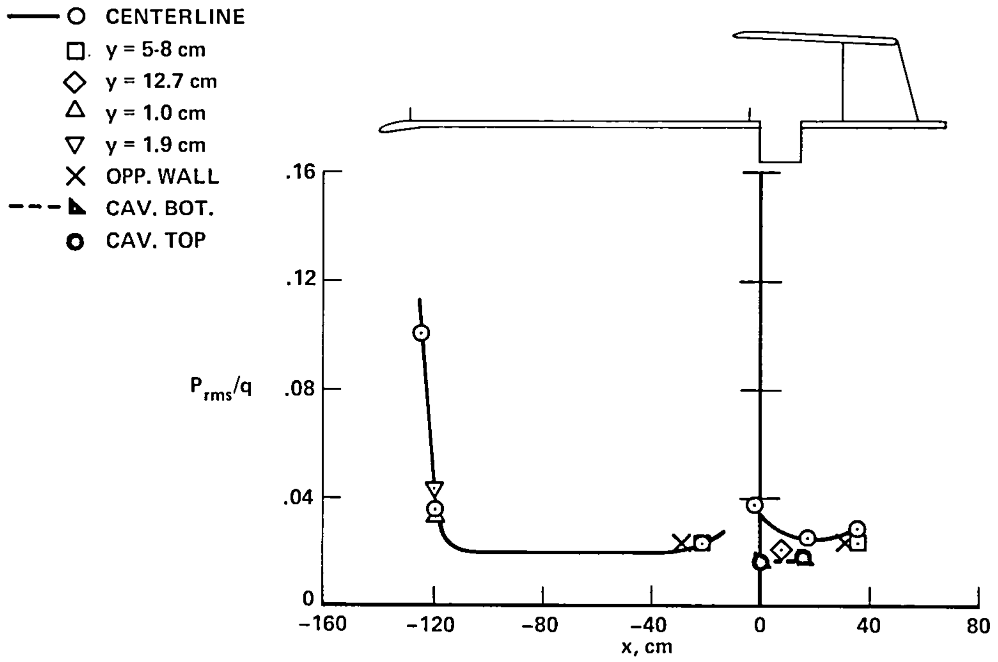

Figure 94.– Fluctuating-pressure coefficients on plate, wall, and cavity; Model 12, Instrumentation 7, $M = 0.60$, $R = 9.8 \times 10^6$/m.

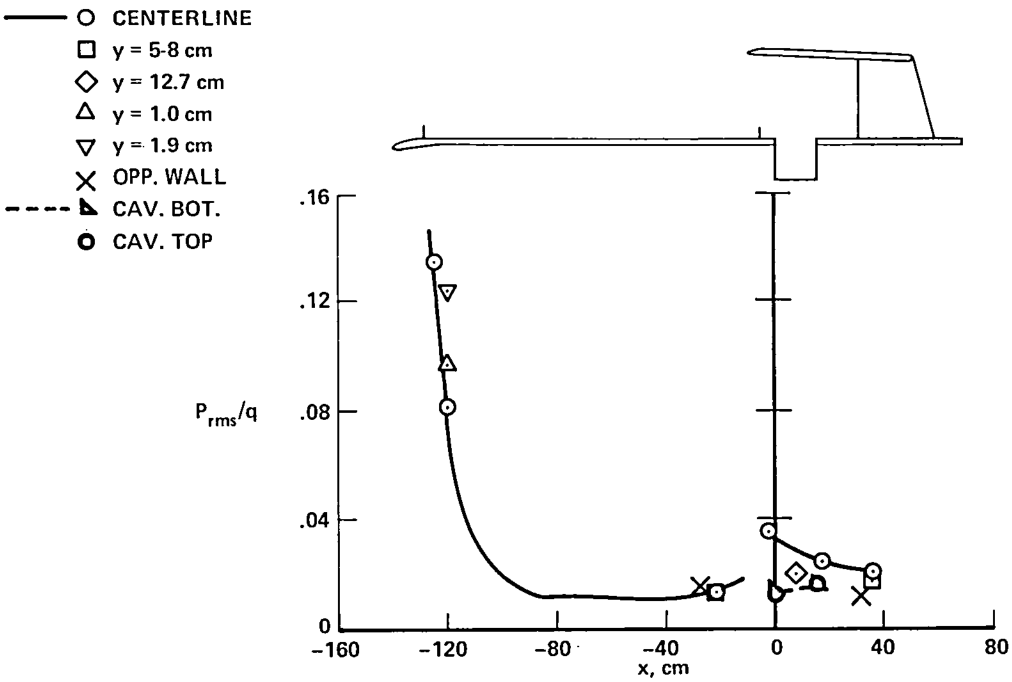

Figure 95.– Fluctuating-pressure coefficients on plate, wall, and cavity; Model 13, Instrumentation 7, $M = 0.89$, $R = 9.8 \times 10^6$/m.

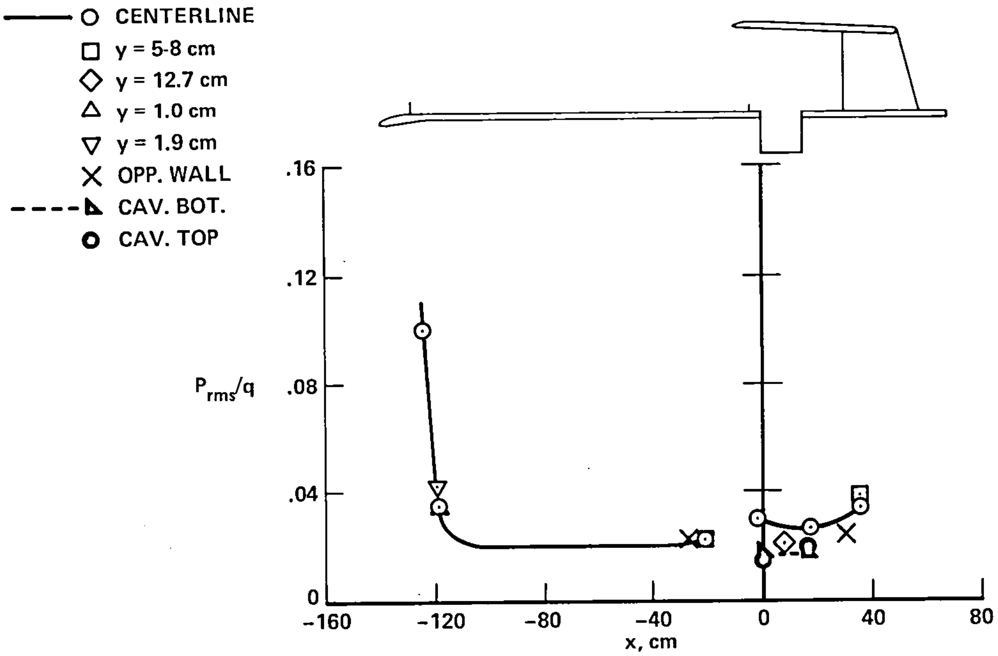

Figure 96.– Fluctuating-pressure coefficients on plate, wall, and cavity; Model 13, Instrumentation 7, $M = 0.60$, $R = 9.8 \times 10^6$/m.

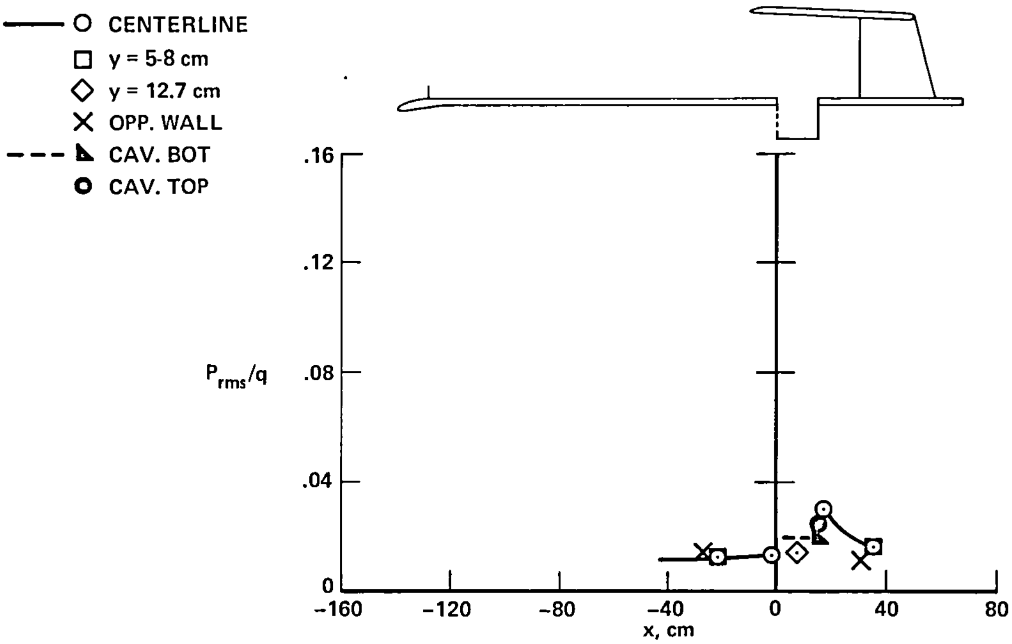

Figure 97.– Fluctuating-pressure coefficients on plate, wall, and cavity; Model 14, $\dot{m}$ = 0, Instrumentation 2 , M = 0.89, R = 9.8X10^6/m.

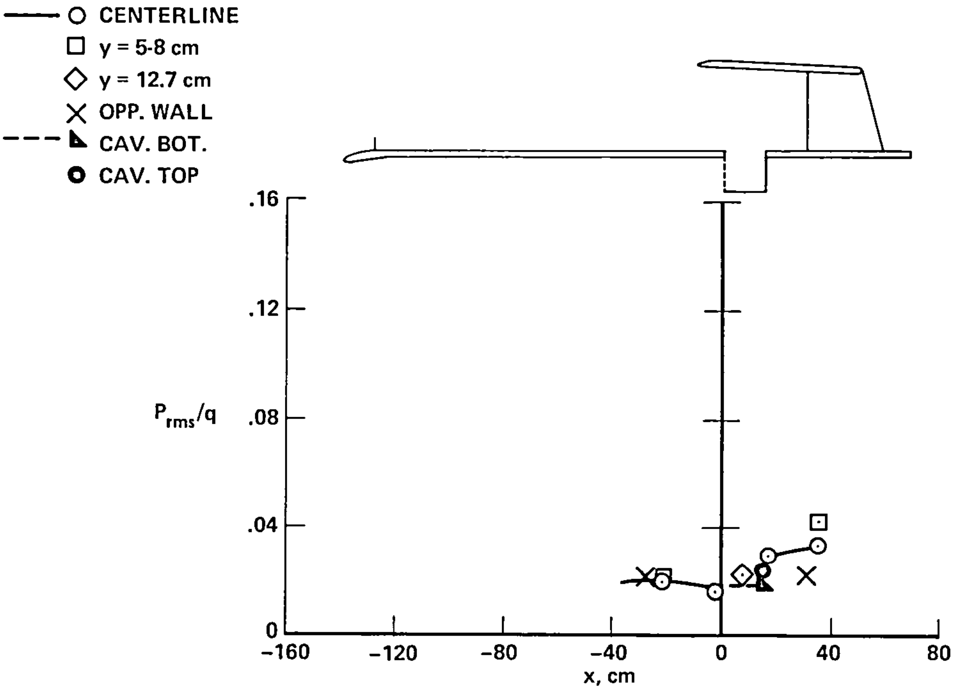

Figure 98.– Fluctuating-pressure coefficients on plate, wall, and cavity; Model 14, $\dot{m}$ = 0, Instrumentation 2, M = 0.60, R = 9.8X10^6/m.

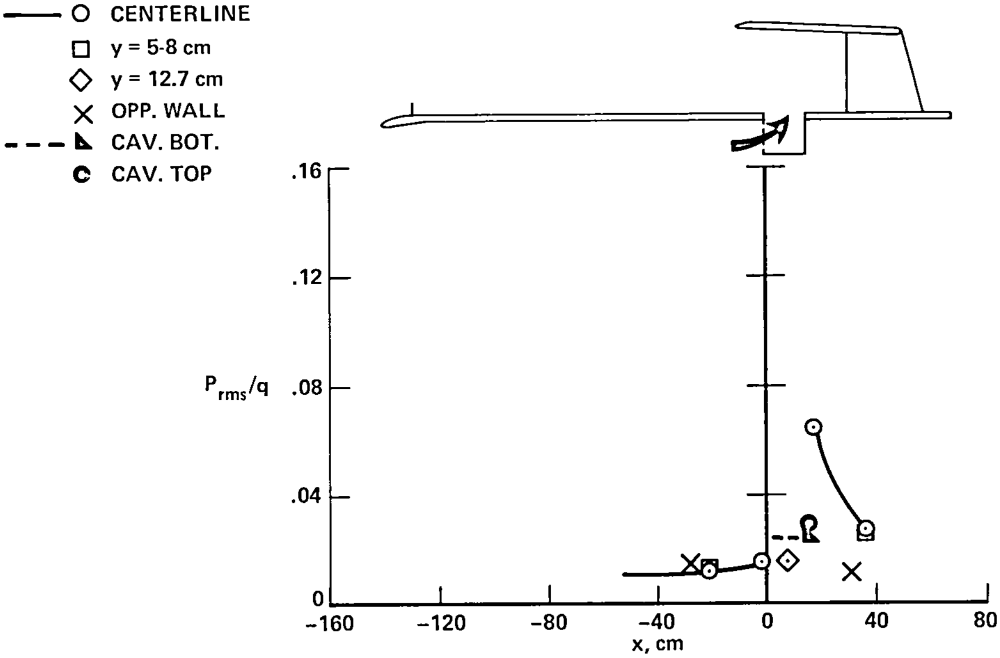

Figure 99.– Fluctuating-pressure coefficients on plate, wall, and cavity; Model 14, $\dot{m}$ = 0.24 kg/sec, Instrumentation 2, M = 0.89, R = 9.8X10^6/m.

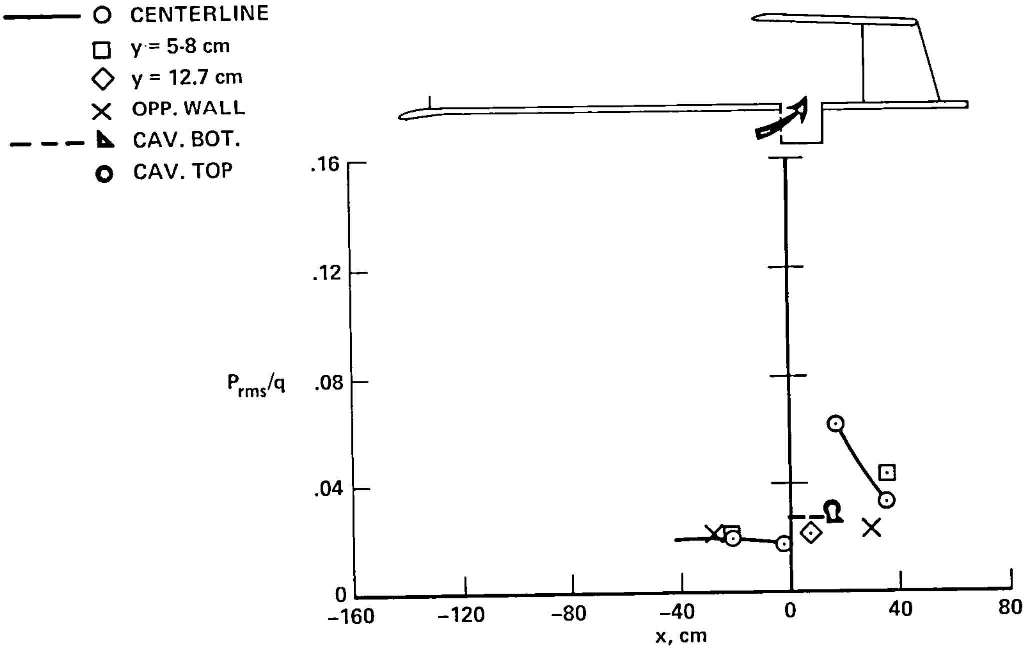

Figure 100.– Fluctuating-pressure coefficients on plate, wall, and cavity; Model 14, $\dot{m}$ = 0.24 kg/sec, Instrumentation 2, M = 0.60, R = 9.8X10^6/m.

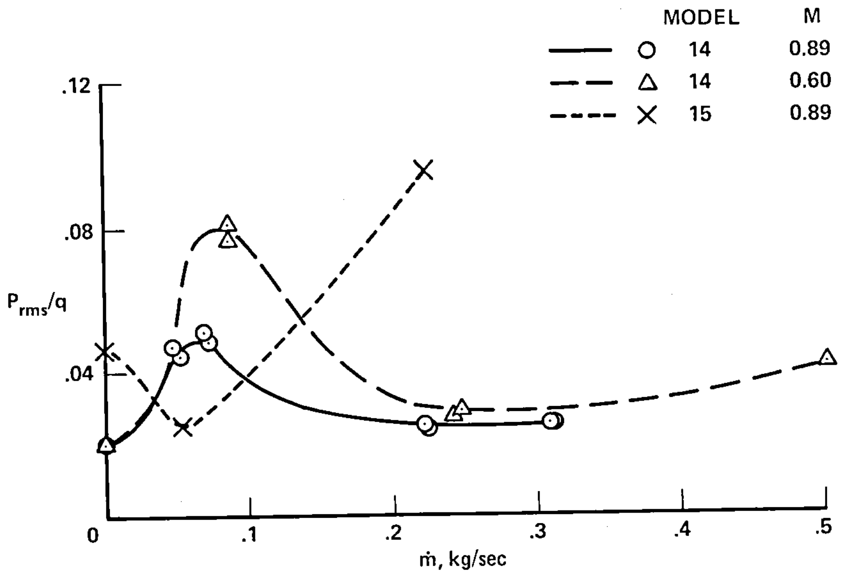

Figure 101.– The effect of mass flow on fluctuating-pressure coefficients in the cavity; FP123, $R = 9.8 \times 10^6$/m.

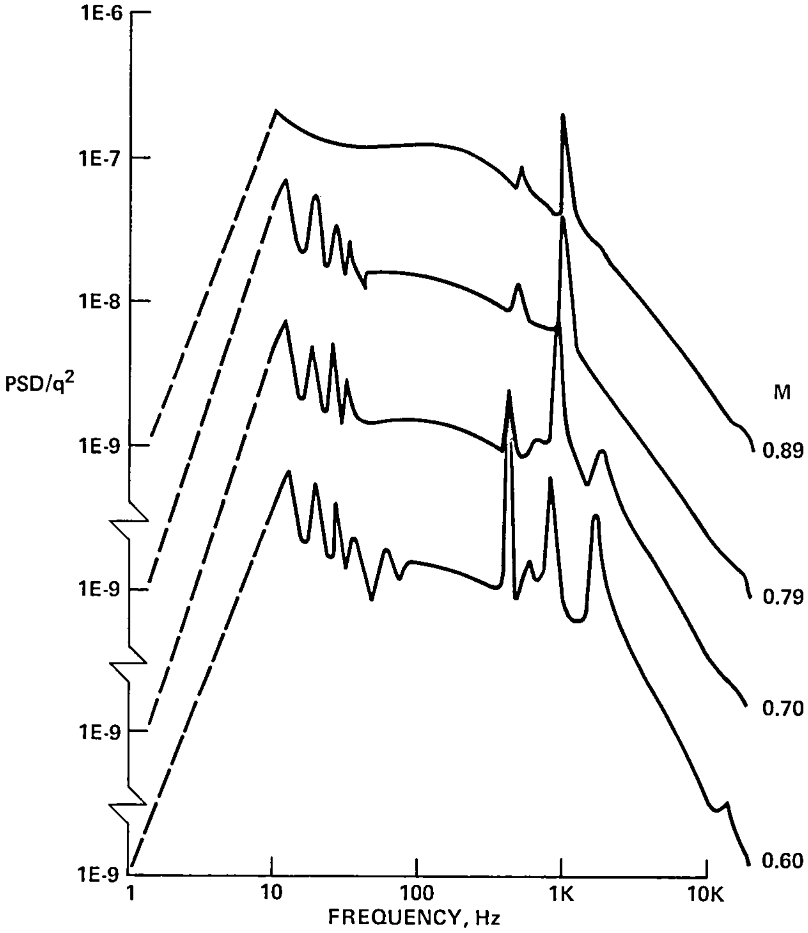

Figure 102.– Power-spectral density of pressures on the wall opposite the model; FP131, Model 8, $R = 9.8 \times 10^6$/m.

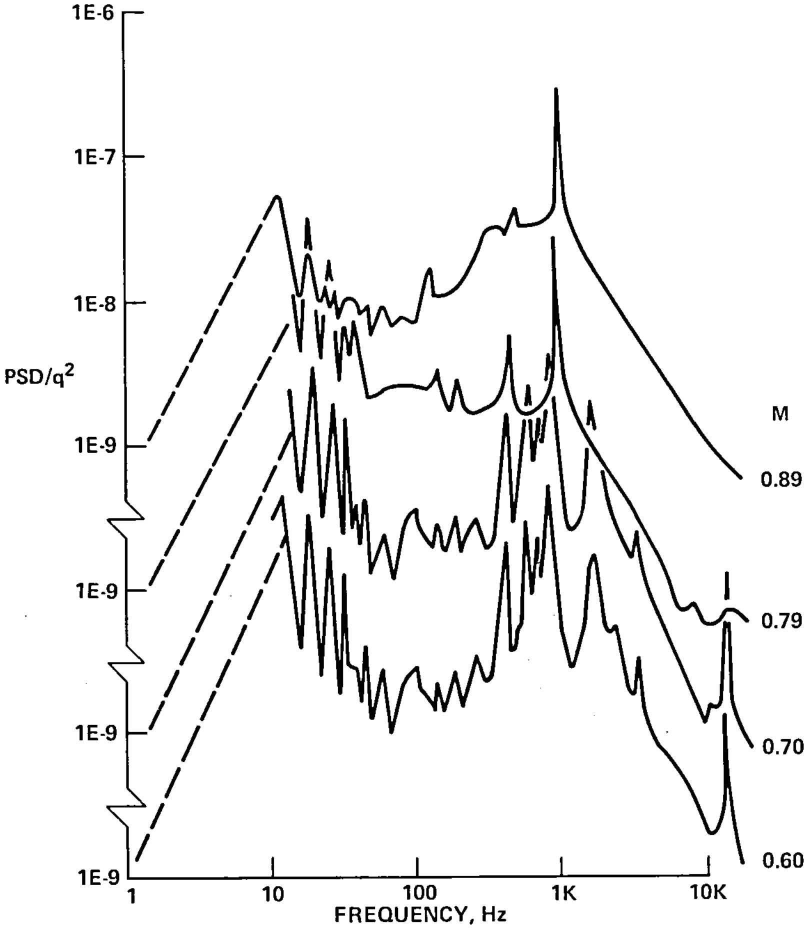

Figure 103.– Power-spectral density of pressures at the center of the plate; FP108, Model 8, $R = 9.8 \times 10^6$/m.

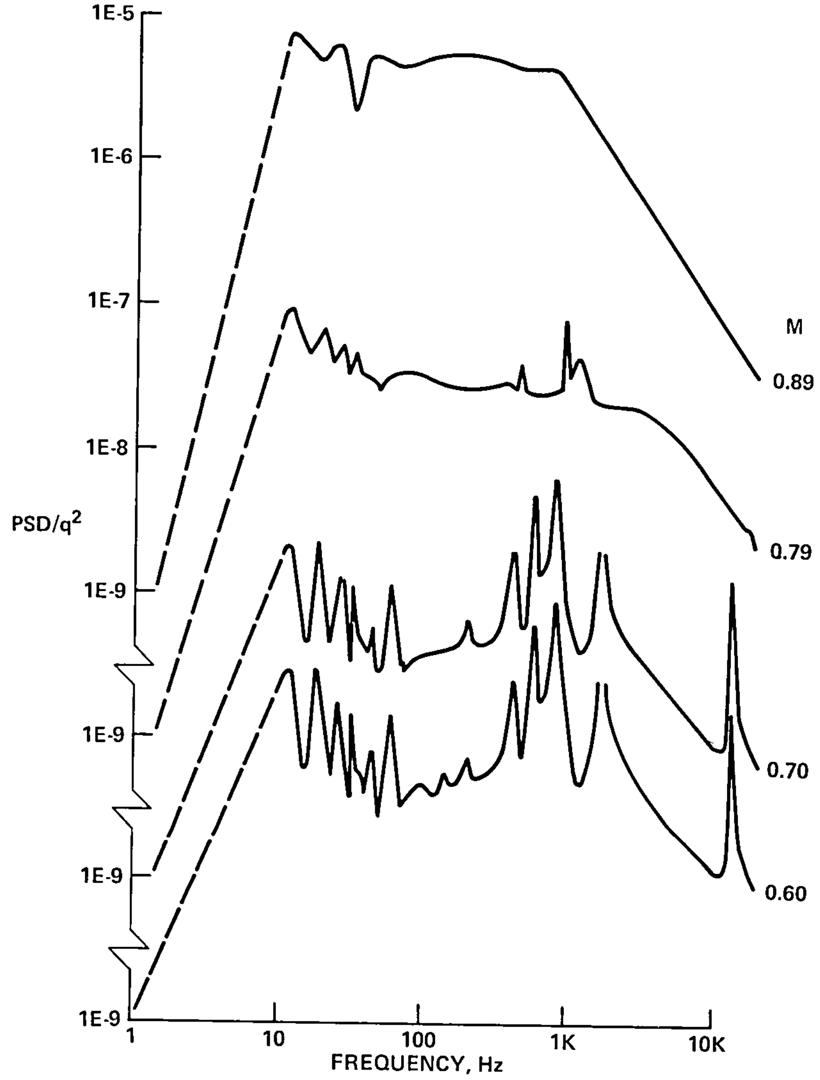

Figure 104.– Power-spectral density of pressures near plate leading edge; FP109, Model 8, $R = 9.8 \times 10^6$/m.

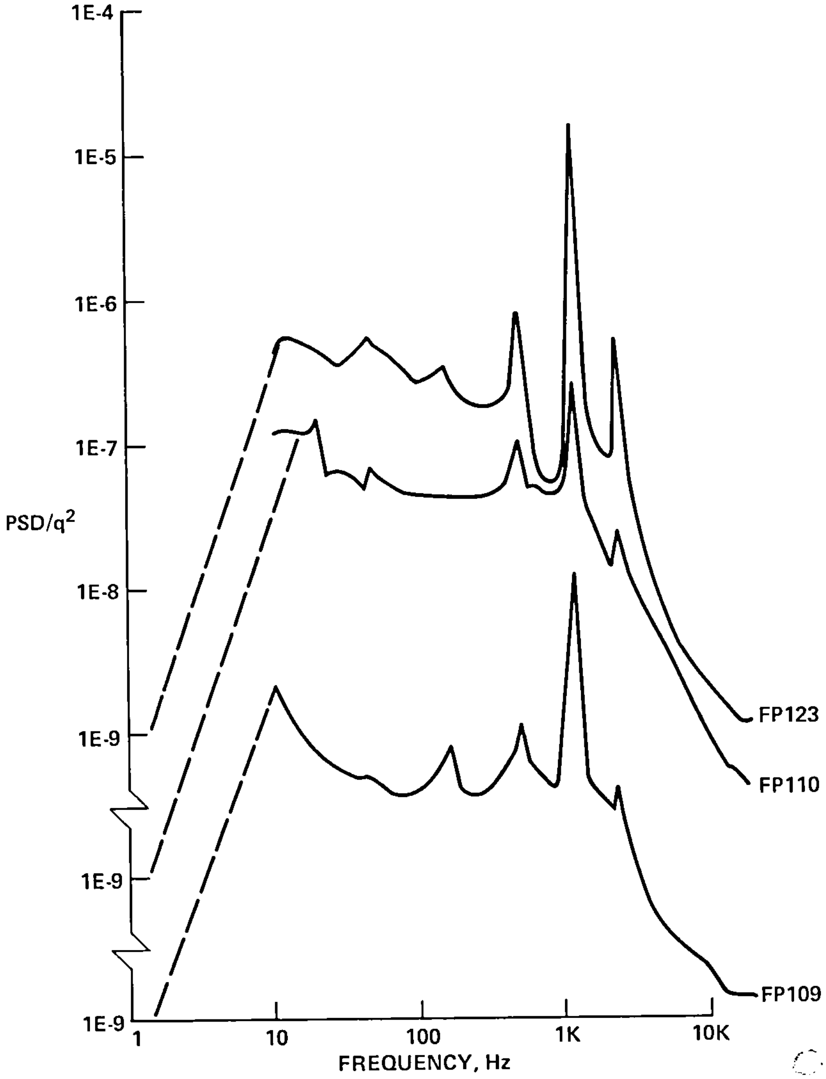

Figure 105.– Power-spectral density of pressures in and near cavity; Model 8, $M = 0.89$, $R = 9.8 \times 10^6$/m.

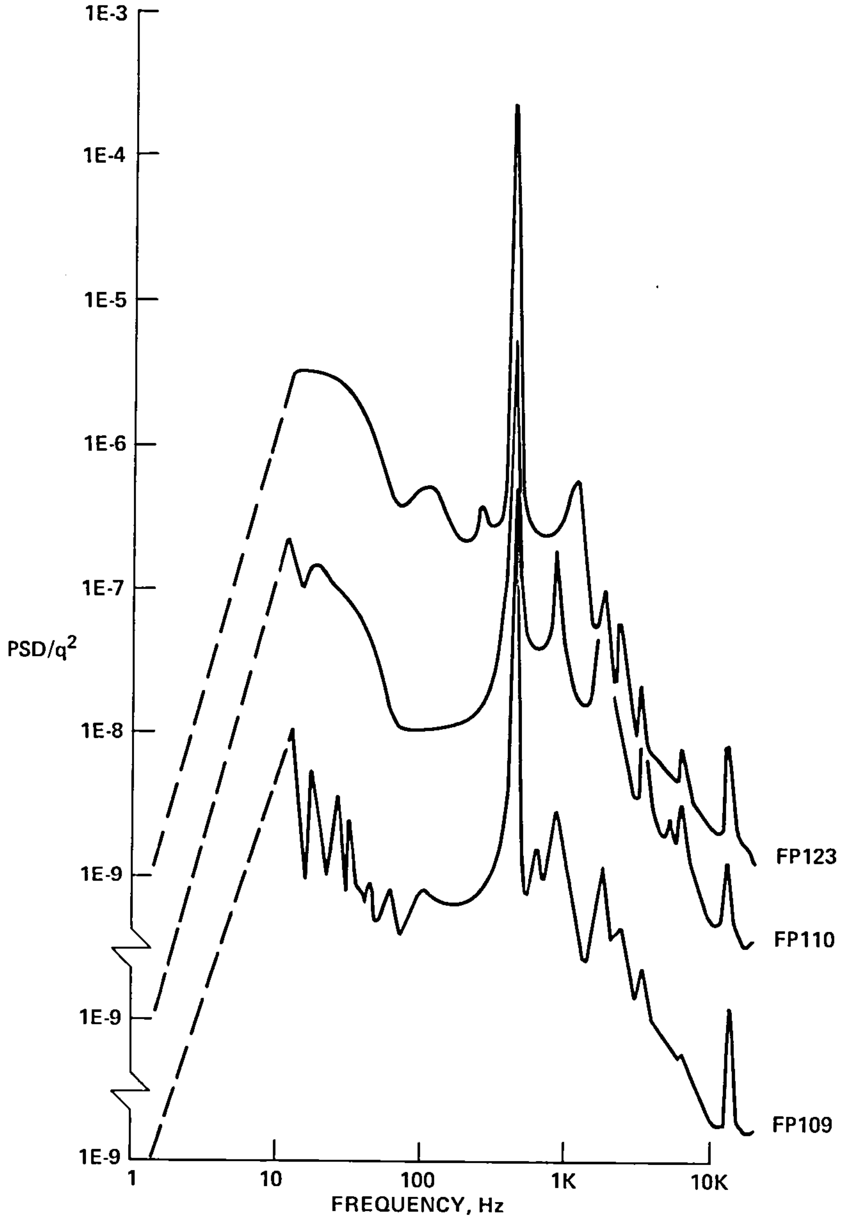

Figure 106.– Power-spectral density of pressures in and near cavity; Model 8, $M = 0.60$, $R = 9.8 \times 10^6$/m.

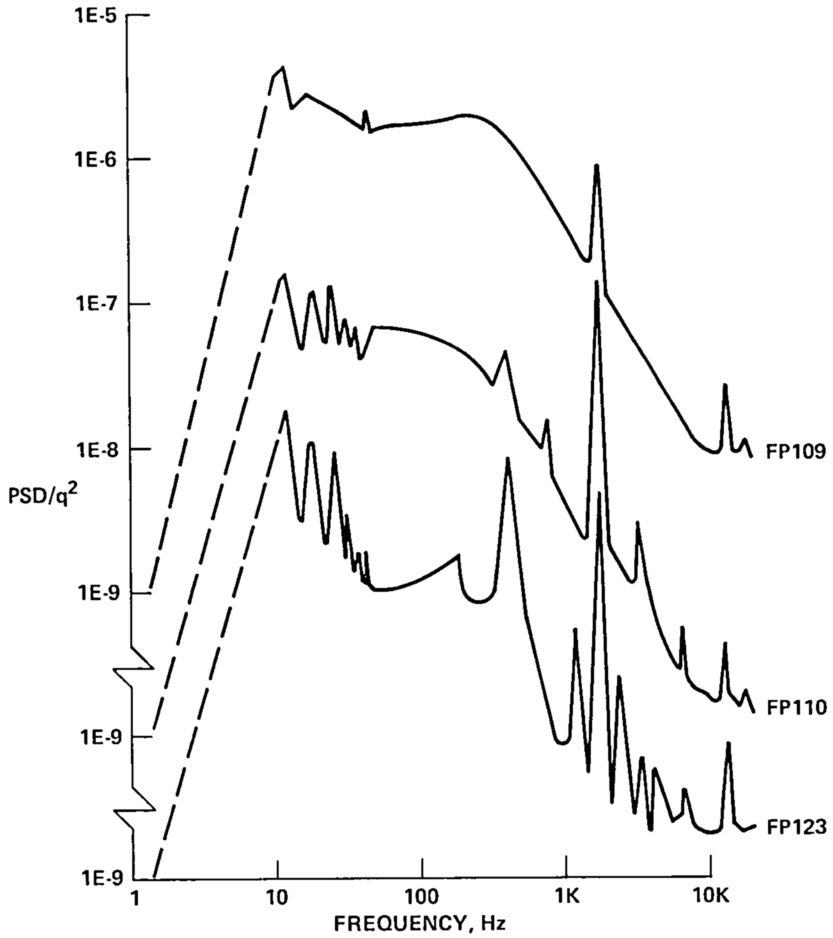

Figure 107.– Power-spectral density of pressures in and near cavity; Model 11, $M = 0.89$, $R = 9.8 \times 10^6$/m.

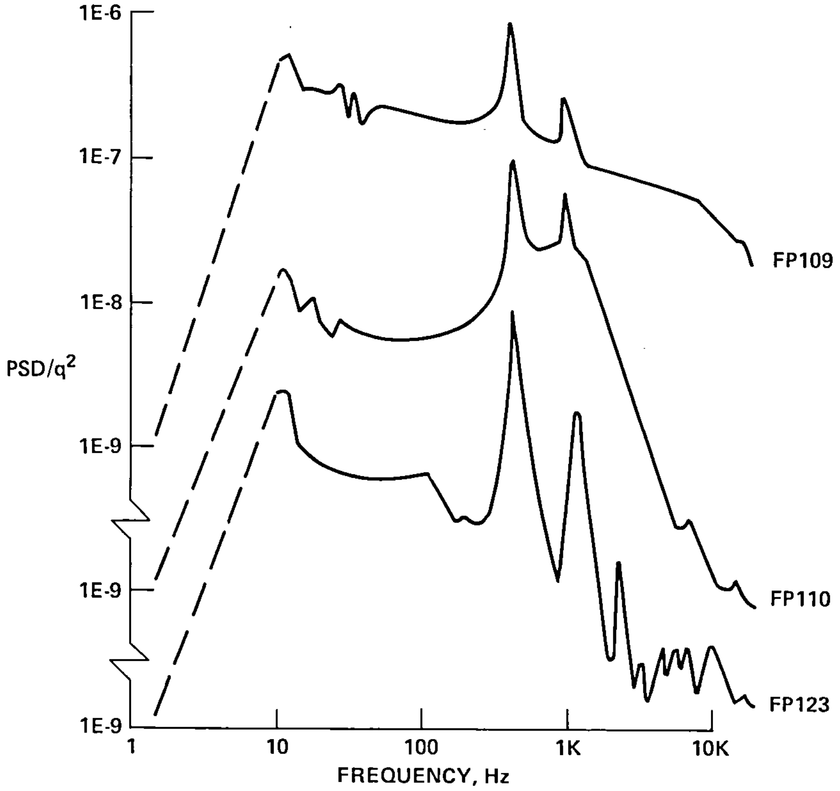

Figure 108.– Power-spectral density of pressures in and near cavity; Model 13, $M = 0.89$, $R = 9.8 \times 10^6$/m.

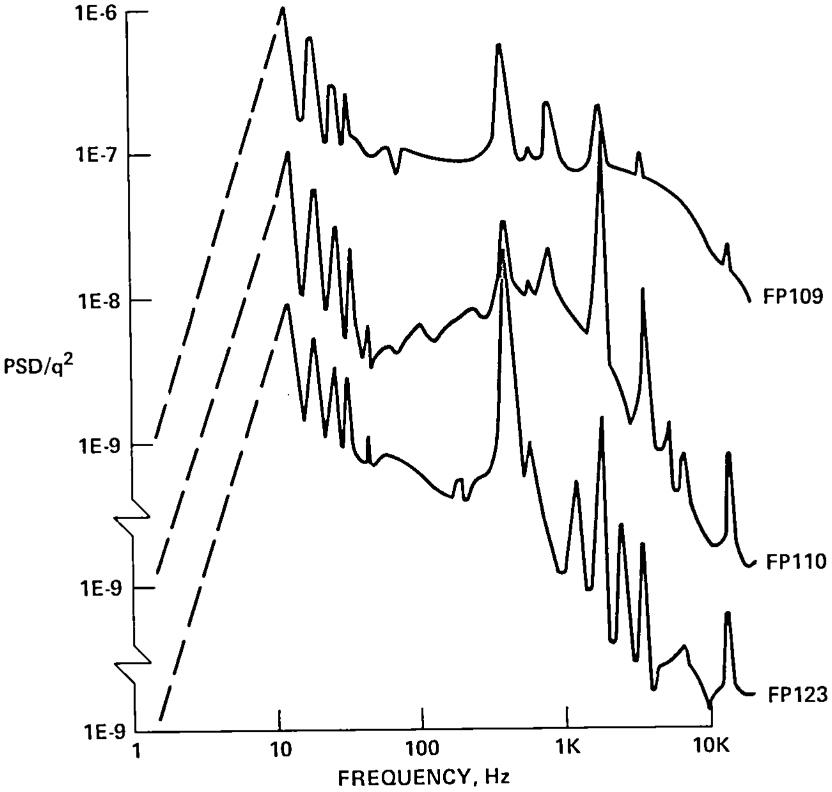

Figure 109.– Power-spectral densities of pressures in and near cavity; Model 13, $M = 0.60$, $R = 9.8 \times 10^6$/m.

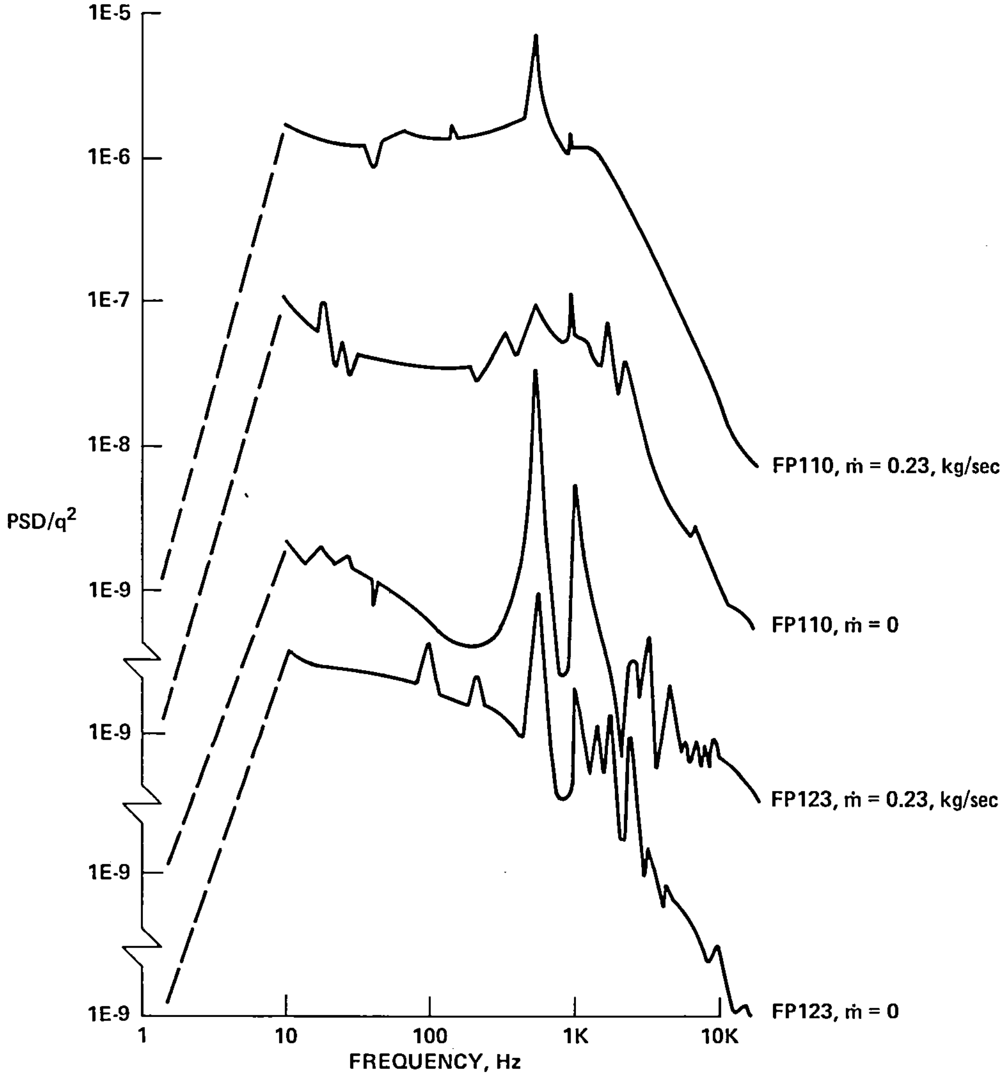

Figure 110.– Power-spectral densities of pressures in and downstream of cavity; Model 14, $M = 0.89$, $R = 9.7 \times 10^6$/m.

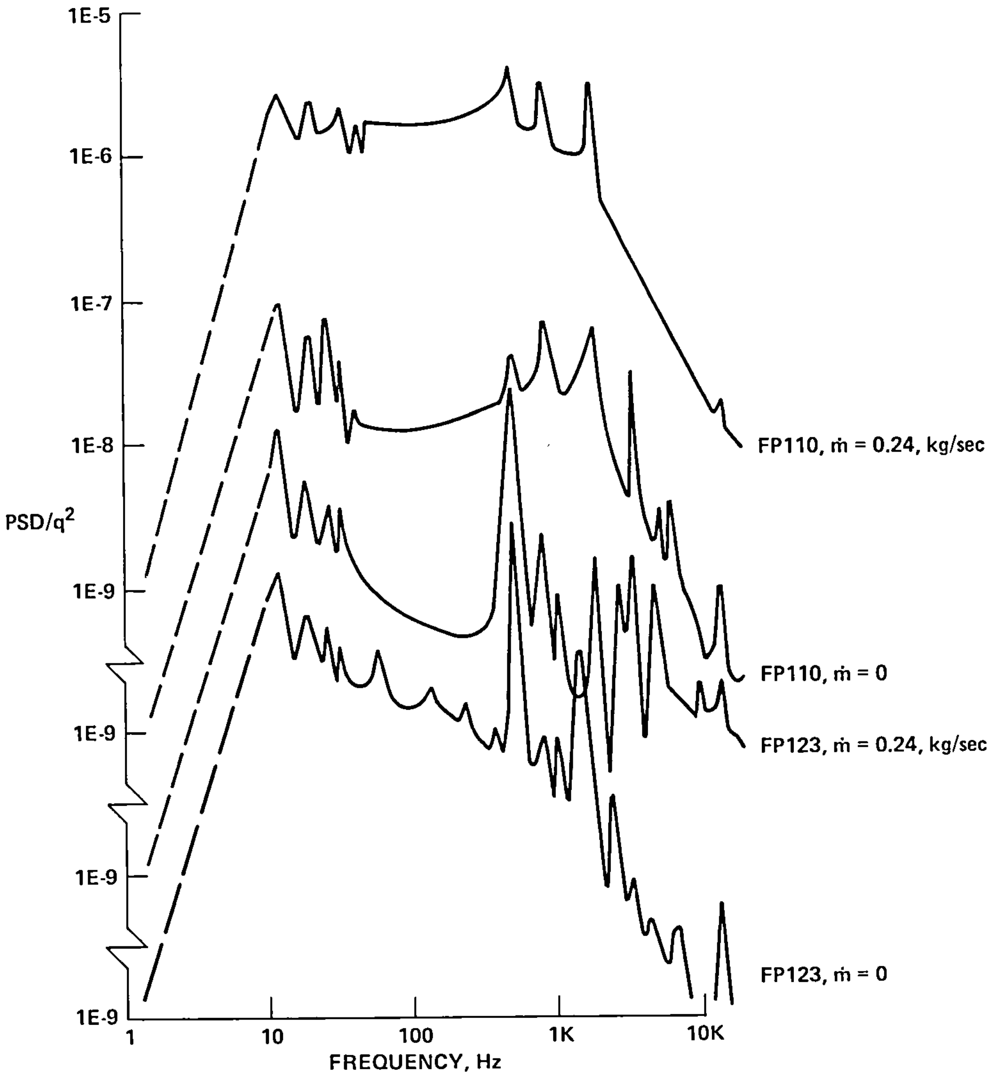

Figure 111.– Power-spectral density of pressures in and downstream of cavity; $M = 0.60$, $R = 9.8 \times 10^6$/m.

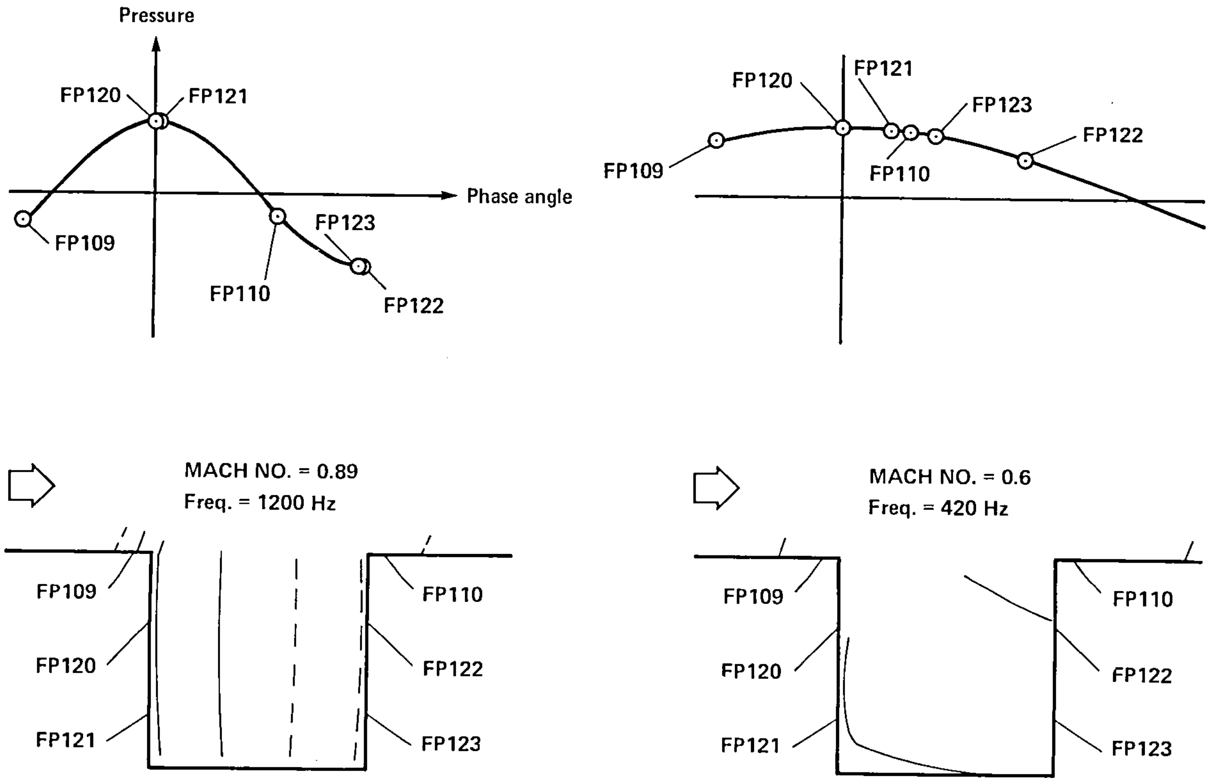

Figure 112.– Phase relationships in cavity resonance; Model 8.

1. Report No.
NASA TM-78487

2. Government Accession No.

3. Recipient's Catalog No.

4. Title and Subtitle
AERODYNAMIC PROPERTIES OF A FLAT PLATE WITH CAVITY FOR OPTICAL-PROPAGATION STUDIES

5. Report Date
January 1979

6. Performing Organization Code

7. Author(s)
Donald A. Buell

8. Performing Organization Report No.
A-7450

9. Performing Organization Name and Address
NASA, Ames Research Center
Moffett Field, Calif. 94035

10. Work Unit No.
505-06-21

11. Contract or Grant No.

12. Sponsoring Agency Name and Address
National Aeronautics and Space Administration
Washington, D.C. 20546

13. Type of Report and Period Covered
Technical Memorandum

14. Sponsoring Agency Code

15. Supplementary Notes

16. Abstract

Transonic wind-tunnel tests have been performed on a flat plate with and without a cube-shaped cavity and antiresonance devices. Measurements were made of the optical propagation and aerodynamic properties of the boundary and shear layers. This report describes the model and its velocity profiles and pressures.

17. Key Words (Suggested by Author(s))

Turbulence
Transonic
Boundary layer
Shear layer
Cavity
Optics
Propagation

18. Distribution Statement
Unlimited

STAR Category – 02

19. Security Classif. (of this report)
Unclassified

20. Security Classif. (of this page)
Unclassified

21. No. of Pages
100

22. Price*
$5.00

*For sale by the National Technical Information Service, Springfield, Virginia 22161

NASA-Langley, 1979

National Aeronautics and
Space Administration

Washington, D.C.
20546